EXPERIMENTAL STUDY OF AVALANCHE IONIZATION IN THE FEMTOSECOND BREAKDOWN OF ATOMIC LAYERED MATERIALS

by

Sabeeh Irfan Ahmad

A dissertation submitted to the faculty of
The University of North Carolina at Charlotte
in partial fulfillment of the requirements
for the degree of Doctor of Philosophy in
Optical Science and Engineering

Charlotte

2024

Approved by:

____
Dr. Tsing-Hua Her

____
Dr. Tino Hofmann

____
Dr. Haitao Zhang

____
Dr. Yong Zhang

ABSTRACT

SABEEH IRFAN AHMAD. Experimental Study of Avalanche Ionization in the Femtosecond Breakdown of Atomic Layered Materials. (Under the direction of DR. TSING-HUA HER)

The engine of modern society is fueled by information, and the desire to obtain, process and relay it ever more quickly is motivation for scientists to dig deeper into pathways that enable this endgame. The implementation of ever-quicker computer processors, optical fiber-based communications, and Light Detection and Ranging (LiDAR) for climate studies are a small subset that illustrates how ubiquitous the applications of optics are. In this context, the study of 2D materials (2DMs) is important due to the fascinating properties they exhibit that could lead to a plethora of future opto-electronic applications that extend beyond what silicon alone can provide. The story began with graphene due to its high conductivity and tensile strength, but due to the difficulty of switching its conductivity, applications in transistors is limited, and other materials such as the transition metal dichalcogenides (TMDs) MoS_2 and WS_2, which exhibit a bandgap transition from indirect to direct when going from bulk to monolayer, are being explored. The wide bandgap semiconductor hexagonal boron nitride (hBN) has also been piquing interest. The presence of room-temperature stable excitons detected via various spectroscopies suggests applicability in mainstream field-effect transistors, and current industry direction towards so-called ‘nanosheet’ and ‘nano-wire’ channel transistors serve as prime examples of the relevant applicability of such 2D materials. Quantum computing and valley-tronic applications have also been reported, making this class of material exciting to study.

When material dimensions are reduced to the single atomic layer (‘monolayer’) limit, fast carrier dynamics become important that can only be investigated by even faster phenomena i.e., femtosecond ‘ultrafast’ laser pulses. When exposed to intense electric fields, several processes can occur; multiphoton absorption (MPA) which utilizes multiple photons to promote a single charge carrier to the conduction band (CB), tunneling ionization (TI) in which the laser field modifies the inter-atomic potential and allows CB access via tunneling, and avalanche ionization (AI) where inter-carrier impact causes ionization. Together, these strong-field ionization (SFI) processes are subject to significant research effort. If SFI-induced excited carrier populations exceed a threshold, damage occurs via a non-thermal ‘ablation’ process which is advantageous for cutting and patterning.

The objective of this work was to explore the ultrafast optical dielectric breakdown (ODB) behavior of 2DMs such as MoS_2, WS_2, and hBN. The work involves an investigation of the etalon interference effect that causes differences in the ablation threshold fluence for the same material when placed on different substrates, differences in threshold fluence between different 2DMs, as well as an exploration of laser-induced defects added when multiple ultrafast pulses are incident on the material. ODB for the wide bandgap insulator hBN is also demonstrated and characterized using various imaging modalities and spectroscopies for the first time. Through the findings presented in this work, some aspects of the nature of ablation are unraveled, particularly the dominance of avalanche ionization as the key carrier generation mechanism in the ODB process in 2D materials. Femtosecond laser direct writing was established as a useful tool for the nanopatterning of such 2DMs.

ACKNOWLEDGEMENTS

I have been very fortunate to spend time under the tutelage of some truly remarkable people. Firstly, I would like to sincerely thank my supervisor Dr. Tsing-Hua Her for all his support, guidance, and understanding in every step of the process of performing this work. Without the opportunity of working in your laboratory and learning under you I would not be in the place I am now. I would also like to thank the professors on my committee; Dr. Tino Hofmann, Dr. Haitao Zhang and Dr. Yong Zhang for their advice, discussion, and access to various instruments in their respective labs. I would also like to recognize our collaborators in Taiwan from the institutions NCTU and NTHU for their feedback and support, as well as for the fabrication of the samples utilized in this study.

I would also like to extend my heartfelt gratitude to my colleague Joel M. Solomon for his support, camaraderie, and scientific expertise. Without your friendship this work would not have seen the light of day. I am also grateful toward Arpit Dave and Emmanuel Sarpong for being extremely supportive lab mates who were unhesitant in helping with experimental work and analysis whenever it was needed. The value of the various friends I have been so fortunate to make cannot also not be understated. Without all of you I would have buckled long ago.

This work was funded by various grants through NCTU and NTHU, Charlotte’s GASP/Fellowship, as well as Charlotte’s GSSF summer funding.

CONTENTS

LIST OF TABLES

LIST OF FIGURES

LIST OF ABBREVIATIONS

2D	Two-dimensional
2DMs	Two-dimensional materials
AFM	Atomic Force Microscopy
AI	Avalanche Ionization
BBO	Barium borate
CB	Conduction Band
CCD	Charge coupled device
CM	Contact mode for atomic force microscopy
CP	Circular polarization
CW	Continuous wave
DBR	Distributed Bragg reflector
DFT	Density functional theory
DIBL	Drain-induced barrier lowering
DIC	Differential Interference Contrast
EELS	Electron energy loss spectroscopy
FCA	Free Carrier Absorption
FIB	Focused ion beam milling
FWHM	Full width at half maximum
GAA	Gate-all-around
GW	Green’s function method used in density functional theory
HHG	High-harmonic generation

HR-TEM	High-resolution transmission electron microscopy
HWP	Half-wave plate
LDW	Laser direct writing
LHC	Left-handed circular polarization
LP	Linear polarization
LPF	Low-pass filter
MPA	Multiphoton absorption
NA	Numerical Aperture
ODB	Optical Dielectric Breakdown
OM	Optical Microscopy
PI	Photoionization
PL	Photoluminescence
PMMA	Poly (methyl methacrylate)
PF	Peak-Force mode for atomic force microscopy
RIE	Reactive ion etching
RHC	Right-handed circular polarization
RTA	Rapid thermal annealing
SEM	Scanning electron microscopy
SH	Second harmonic
SHG	Second harmonic generation
SFI	Strong Field Interactions
SPE	Single photon emitter
TBC	Thermal boundary conductance

TI	Tunneling ionization
TMDs	Transition Metal Dichalcogenides
TM	Tapping mode for atomic force microscopy
TMM	Transfer Matrix Methods
TRT	Thermal release tape
UV-vis-NIR	Ultra-violet-visible-near-infra-red
VB	Valence Band
ZTA	Zero thickness approximation
MoS_2	Molybdenum disulphide
$MoSe_2$	Molybdenum diselenide
$NbSe_2$	Niobium diselenide
WS_2	Tungsten disulphide
hBN	Hexagonal Boron Nitride

1 INTRODUCTION

Silicon has long been the well from which the essence of modern technology has been drawn. For decades the Si-based transistor has been refined, polished, and engineered to grow ever smaller, faster and more power efficient so that information can be gathered, processed and relayed. Notable success in this regard has been attained, with impressive computing performance and minuscule device feature sizes being the norm (1). Yet all things have limits and various deleterious effects such as high leakage currents, sub-threshold swing degradation and drain-induced barrier lowering (DIBL) are challenging further progress (1). Various strategies, such as fabricating 'fin'-style gates that wrap around the semiconducting channel, have been implemented to mitigate such short-channel effects via improved electric field control. Current industry direction is towards realizing gate-all-around (GAA) transistors (2) where the channel is a 'nanosheet' or a 'nano-wire' and significant research effort is being directed toward investigating two-dimensional materials (2DMs) that can serve as prime candidates for such devices (3) (4).

2DMs are a class composed of materials that are a few atomic layers thick (and can be down to single layers) that come in various flavors of lattice arrangements, band-structures, and electronic properties (5). The spectrum of bandgaps spanned by these materials make them attractive for different components in transistors. As an example, the highly conductive metal graphene (possessing a bandgap $E_g = 0$ eV and a uniquely linear band-structure) is a good prospect as an ultra-thin source/drain component. As the 2DM to undergo the most amount of scientific scrutiny, graphene (6) has been found to exhibit a dizzying array of properties such as strong wavelength-independent absorption of 2.3% (7) due to its metallic nature and unique band-structure (containing Dirac cones) (8), high carrier mobilities reaching 200,000 $cm^2/(V\cdot s)$ if extrinsic disorder is eliminated (9), and a remarkably high mechanical robustness 6. Higher in bandgaps are the semiconducting transition metal dichalcogenides (TMDs) Molybdenum disulphide (MoS_2) and Tungsten disulphide (WS_2) with $E_g = 2.4$ eV and 2.73 eV respectively in the monolayer (10) undergo a transition of the bandgap from indirect-to-direct as the thickness is reduced to the monolayer limit. 2D TMDs are attractive for opto-electronics such as photodetectors (11), saturable absorbers in mode-locked lasers (12) and active media in coherent light sources (13, 14). Applications in quantum computing and valley-tronic for future-generation computing and storage have also been reported (15, 16). Even further up in bandgap is the wide-gap insulator (~7.7 eV electronic E_g, ~ 6 eV optical E_g) hexagonal boron-nitride (hbN) (17, 18), that possesses a crystal structure very similar to graphene but in which alternating boron (B) and nitrogen (N) atoms are covalently bonded to each other in a honeycomb lattice arrangement. The ability to produce second and high-order harmonics of laser beams (predicted theoretically but not yet demonstrated experimentally) (19) (20), piezoelectricity in the monolayer (21), mechanical flexibility and breaking strength (22), and great chemical stability (23) make it an attractive prospect for multi-faceted optical and electrical applications. Even its passive properties are useful; hBN permits no penetration of gases and liquids through itself, which grants atmospheric immunity to unstable materials such as niobium diselenide ($NbSe_2$) and black phosphorous (24). Various groups have demonstrated improvements in 2D TMD based device performance and stability when active layers were encapsulated in hBN because of its atomically smooth surface and lack of dangling bonds (25). Together, with graphene as the source and drain, semiconducting TMD as the channel and hBN as the gate insulator, device size can be further reduced and performance improved, all leading toward the ideal single-electron transistor.

The various applications described for 2DMs often require the ability to reliably pattern the working materials into desired shapes and geometries and various methodologies have been explored for deterministic patterning. Ziegler et al. report on the formation of quantum emitting defects on the edges of regions with high curvature, such as arrays of holes of diameter ~500 nm that were created using Focused Ion Beam milling (FIB)(26). While FIB is capable of smaller features down to 20 nm (27), a significant disadvantage is lateral crystal damage and substrate modification incurred as a result of the ion bombardment that remains even after annealing procedures are performed (28). Froch. et al. created suspended photonic crystal cavities out of hBN to enhance the electric fields experienced by the SPEs via the use of hybrid electron beam and Reactive Ion Etching (RIE) techniques, achieving 100 nm feature sizes (29). Such techniques have the disadvantages of being slow (with a 200 x 200 nm raster scan taking ~ 30 minutes to complete)(30) and involving multiple complicated steps that require careful process optimization. Electrons backscattered from the substrate also are prone to producing an undesired affected region on the sides of patterns and highlight the need for process parameter selection (31). Kim et al. utilized the exhibition of a Non-Volatile Resistive Switching effect to fabricate high speed analog switches for terahertz communications, where a single hBN layer is sandwiched between two metal electrodes, their group also using e-beam techniques to fabricate a lateral feature size of ~ 500 nm (32). In a similar vein, Siaj et al. discovered space-charge limited carrier transport in hBN nanoribbons, which is an important step toward the realization of UV-emitting laser diodes and light emitting diodes (33). The existence of a hyperbolic dispersion in the optical spectrum gives rise to the existence of phonon polaritons (PhPs) that have propagation lengths longer than plasmon polaritons, making hBN an exciting candidate for meta-surfaces and sub-wavelength optics. Zhang et al. propose a design involving a disk array with 10 nm holes that can support PhPs utilizing monolayer hBN (34), while Hillebrand et al. demonstrate that surface-confined PhP designs require small ribbons of width 70 nm with slits 30 nm wide between them, demonstrating the importance of being able to pattern hBN (35). Norris et al. utilize a novel technique toward this end via thermal scanning probe lithography that uses a heated AFM tip to create patterns in a resist that can then be transferred to hBN (36). The resolution achieved is impressive (~ 30 nm for thicker samples, ~ 10 nm for thinner ones) but the technique, like all lithography-based methods, is prone to leaving behind undesirable photoresist residues. Such residues can reduce device performance in the case of vertical heterostructures where scattering can occur at resist sites and require additional cleaning procedures (37). Such diverse applications of useful properties highlight the need for a patterning technique that is fast, causes minimal crystal and surface damage, and can produce fine features.

Laser Direct Writing (LDW) is advantageous as a patterning method in that it avoids the use of resists, forgoes the need for high vacuum equipment and thus is relatively lower in cost, is a high-speed technique for prototyping in-situ, all qualities which introduce an overall simplicity to the patterning process. LDW has previously demonstrated the ability to pattern 2D materials. Finer features in graphene have been demonstrated by using phase-plate-structured light, where holes of diameter ~ 85 nm and linear strips of width ~ 20 nm were made using 10-ps 532 nm, via thermally induced oxidative burning (38). Using femtosecond pulses offers benefits over long-pulse or continuous wave sources since the pulse-width are on time-scales faster than electron-phonon coupling lifetime, minimizing heat conduction and reducing the area of the heat-affect zone (HAZ). Ultrafast patterning demonstrated ~ 250 nm linear strips patterned into MoS_2 later in this work (39). With very tight focusing at critical fluence, a tightly focused femtosecond pulse has produced a hole feature < 100 nm on a solid surface (40).

Understanding of the strong-field interaction (SFI) of 2DMs for single and multiple ultrafast pulses is critical to effectively harness LDW as a tool. Such understanding is lacking for many 2DMs. hBN's linear (41) and nonlinear optical properties in the weak limit (42, 43) have been extensively studied yet little is known about its interaction with the strong field in high-intensity laser pulses. To date, although femtosecond laser ablation of hBN has been reported (44, 45), the physics of dielectric breakdown in hBN is not known, and laser patterning of hBN has not been demonstrated. This ignorance is similarly true for the case of ablation of 2D TMDs. Several fundamental processes of carrier generation can occur when ultrafast pulses are incident on a material and knowledge of these phenomena is interesting and important. These processes illustrated in Figure 1-1.

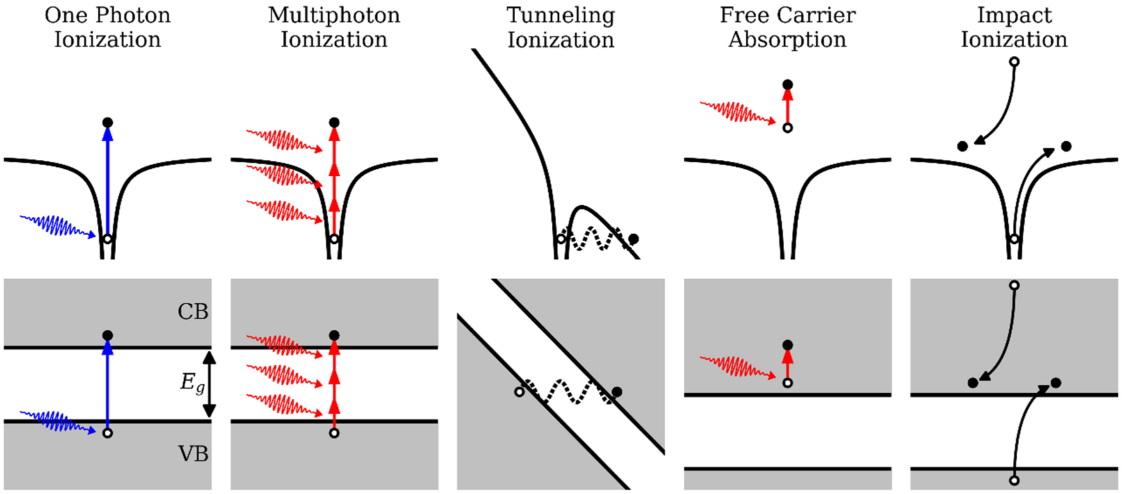

Figure 1-1: Illustration of carrier generation mechanisms when strong-field light is incident on a material. The top row has energy as the vertical axis and space as the horizontal axis. The bottom row displays rudimentary band-structures.

If light is incident on a material several mechanisms of carrier generation can occur. If the material bandgap (E_g) is smaller than the photon energy of the source electrons can absorb individual photons and be promoted into the conduction band (CB) of the material via linear absorption. If the source wavelength is longer than that required for linear absorption to the E_g then a high incident intensity is required for free carrier generation in the CB, moving into the realm of nonlinear optics. Multiple photons can be absorbed simultaneously to promote an electron from the valence band (VB) to the CB in a process termed multiphoton ionization (MPI). Another process is tunneling (also referred to as Zener) ionization (TI) where the strong electric field of the incoming laser pulse can displace the ion cores in the lattice, modifying the potential environment of the electrons, and allowing them to tunnel out of their potential wells into the delocalized states of the CB. Carriers within the CB can absorb subsequent incoming photons and rise higher in the energy in the CB in a process termed free-carrier absorption (FCA, also termed 'inverse bremsstrahlung'). FCA increases the electron's ponderomotive or 'quiver' energy which is the vibrational energy of the electron as it moves in phase with the oscillation of the driving field, moving it higher in energy in the CB (40, 46). If the quiver energy increases to be equal to or higher than E_g , the oscillation amplitude of the electron can be on the order of the lattice constant (~0.3 nm for hBN) and the probability of collisions with VB electrons on the neighboring atoms increases. If such a collision occurs the high-energy electron can impart its energy to the VB electron and promote it to the CB, creating two electrons in the CB in place of the original one. Further FCA would repeat the process, further multiplying the number of electrons in the CB. This multiplication of free carriers results in rapid increases in the number of free carriers, which subsequently also increases the plasma frequency ω_p of the material. Several studies postulate that material breakdown occurs when ω_p equals the laser frequency (40, 47, 48). According to the drude model of free electron plasmas, beyond ω_p the dielectric constant of the material becomes negative, drastically increasing the absorption of the material, leading to a runaway damage process.

Given a sufficient number of free carriers in the CB with sufficient enery, a rapid carrier multiplication process can occur that is referred to as Avalanche Ionization (AI). In the case of small-E_g materials these seed carriers can be present at room temperature. Alternatively, doped materials can have electrons due to donor impurities present in the lattice. Since much of the following work focuses on hBN, which is a wide bang-gap insulator, where the probability of having free carriers in the CB is exceedingly small. In such a case, MPI or TI can seed carriers into the CB and initiate AI. Identifying the specific carrier generation process under ultrafast illumination of materials, whether it is MPI, TI or AI, holds interest for the research community. In the case of AI, differentiating between MPI and TI as the seeding mechanism for AI is also important.

The work undertaken in this dissertation constitutes the first systematic study of optical dielectric breakdown (ODB) and LDW of MoS_2, WS_2 and hBN monolayers by femtosecond laser pulses. The work begins with an examination of the effect of the substrates on the ablation of 2DMs, taking MoS_2 as the subject of study. It is found that the etalon interference effect can effectively explain the wide variation seen in ODB fluence threshold (F_{th}) when the same 2DM is placed on different substrates, contrasting with the commonly accepted view of substrate heat conduction affecting F_{th}. Sub-micron patterning in MoS_2 using LDW is also demonstrated. Since the patterning process involves multiple laser pulses incident on the material the multi-pulse breakdown phenomena is examined in MoS_2 and WS_2 and the nature of laser-induced defects in such 2D TMDs is unveiled using various optical spectroscopies and analysis. Subsequently, the ODB of hBN is investigated. hBN is shown to possess the highest breakdown threshold among currently known 2DMs. Clean removal of hBN while leaving the surrounding hBN film and the substrate intact is demonstrated, indicating that hBN is optically very robust. The ablated features in hBN were revealed to have very small edge roughness due to its ultrahigh fracture toughness. High-resolution femtosecond laser patterning of hBN was demonstrated with impressive <100 nm resolution. These ultrafast investigations enable the clear revelation, for the first time, a linear dependence of F_{th} on the bandgap (E_g) of 2DMs, indicating that such a linear dependency is a universal scaling law, independent of the dimensionality. Indirect evidence for strongly enhanced carrier generation in hBN compared to bulk supporting substrates with a similar bandgap is found. The role of nonlinear ionization mechanisms was probed, and AI was found to be the best candidate as the causative mechanism to explain carrier generation in 2DMs.

Toward the end a preliminary study of less-studied materials such as $Mg(OH)_2$ and $CrCl_3$ is also performed to gather more data in search of support of the claim that AI is the dominant mechanism in 2DMs.

2 EXPERIMENTAL TECHNIQUES

Uncovering the physics that dictates the strong ionization of 2D materials requires carefully designed experiments and setups that are unbiased and isolate the physics under study. These experimental designs are often overlooked in publications where only a single paragraph is given to describe approaches, methods, and equipment in an effort to not disrupt the main message being presented. In some cases, the experimental methods themselves are the most impactful and deserve recognition. To that end, this chapter is dedicated to the various experimental techniques utilized to characterize the laser, experimental setups built to perform laser ablation and methodologies used to characterize ablation features in the 2D films. It provides details on experimental protocols followed in this work and is meant to be used as a reference when examining data presented in subsequent chapters. The illustrations made in this chapter were assembled using 3D CAD files commonly available from various manufacturers of optical and mechanical components (Thorlabs, Newport, Edmund Optics, Aerotech) and online communities such as 3D content central and grab3D. Illustrations of 2D materials were made in the open-source software VESTA.

2.1.1 Characterization of laser beam.

The laser source utilized in the experiments described in this work is a Coherent RegA 9000, which uses a titanium-doped sapphire (Ti:S) crystal to amplify seed pulses from a laser oscillator (Spectra-Physics Tsunami), and produces 800nm, 160 fs pulses. It is important to characterize the output light from the source, collecting information such as the pulse-width, beam cross-sectional profile at the beam waist and the spectrum. Beginning with the pulse-width, such a measurement of such fast laser pulses cannot be performed using conventional photodiodes and electronics because the response time of such instruments is slower than the laser pulse itself, so toward that purpose a home-built autocorrelator was used.

2.1.2 Pulse-width: Autocorrelation.

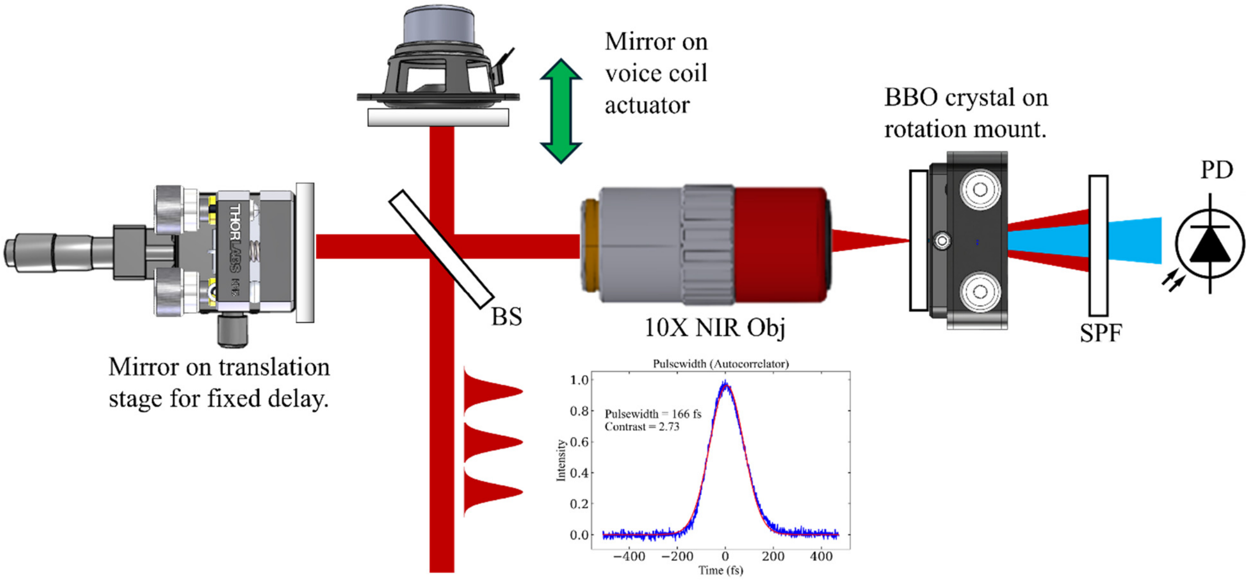

Figure 2-1: Michelson interferometer-style collinear autocorrelation measurement to measure the beam pulse-width from the 800 nm laser pulses.

The laser pulse-width was measured via autocorrelation. The autocorrelator was set up in a collinear Michelson interferometer-style where the pulses are split in two and spatio-temporally overlapped going into the back-aperture of the Mitutoyo NIR objective used in the experiments performed in this work. A type I BBO crystal mounted on a rotation mount is placed after the objective for second-harmonic generation (SHG) and adjusted rotationally to optimize phase matching. A short-pass filter is used to block the 800 nm fundamental beam and a photodiode measures the generated SHG. One of mirrors in the autocorrelator is mounted on a speaker-style voice coil actuator that continuously oscillates the mirror to ‘scan’ one of the pules w.r.t. to the other.

2.1.3 Beam cross-sectional profile.

The beam cross-sectional profile at the laser beam waist after the Mitutoyo 0.28NA objective was characterized using a home-built imaging microscope. A 100X 0.85 NA infinity-corrected objective acts in conjunction with a 150-mm focal length lens to image the laser beam at the waist onto a profiling camera (Dataray WincamD UCD23). The imaging microscope is calibrated using a reference 1951 Air Force target. This setup is shown in Figure 2-2.

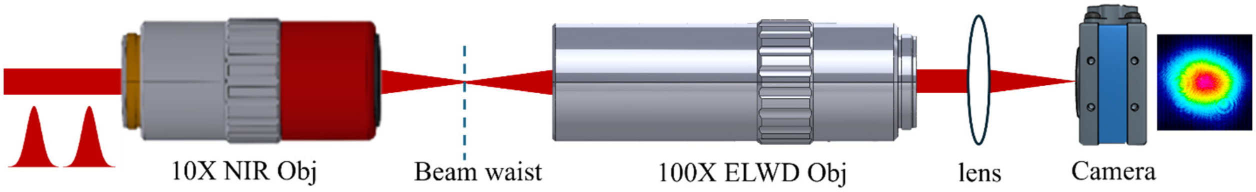

Figure 2-2: Beam microscope used for measuring the spatial profile of the laser beam.

2.2 Optical Dielectric Breakdown (ODB) setup

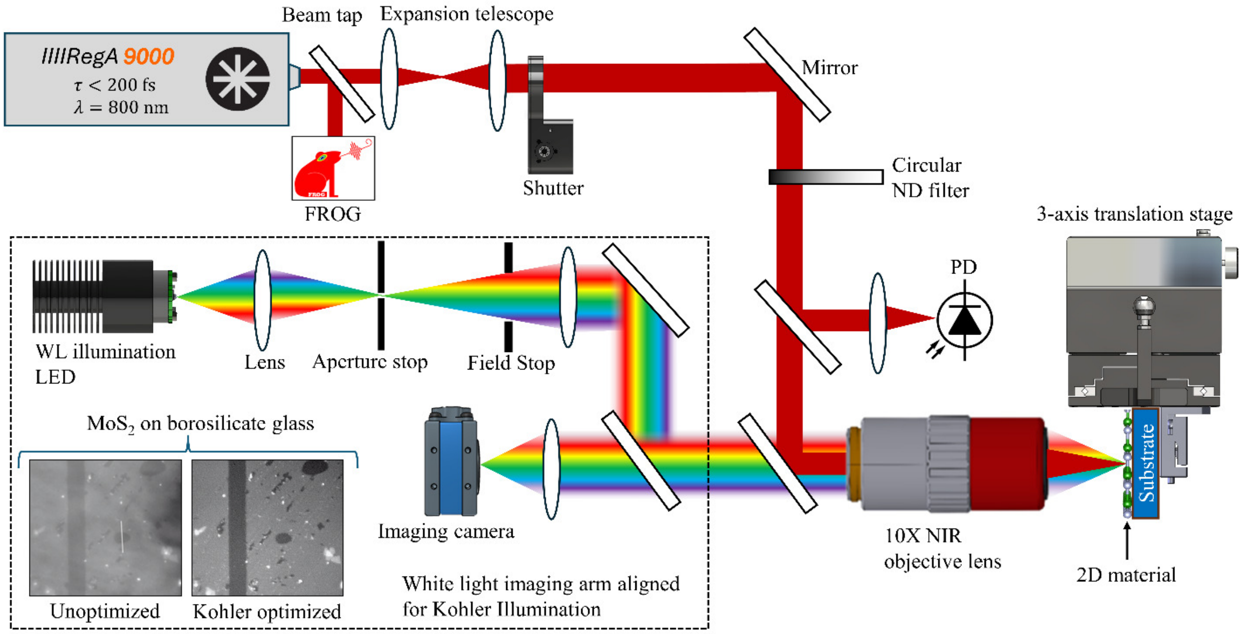

Figure 2-3: Optical dielectric breakdown (ODB) experimental setup with Kohler imaging.

The laser employed is a Coherent RegA 9000 regenerative amplifier seeded by a Spectra Physics Tsunami oscillator, producing 800-nm 160-fs pulses with a pulse energy stability of ~ 0.5%. For the single-shot experiment, the laser was operated at 300 Hz and a single pulse was selected using a mechanical shutter. The laser was focused by either a 0.26-NA (Mitutoyo NIR objective, 10×) or a 0.9-NA (Leitz-Wetzlar NPL 100×) objective for high-NA experiments. The sample was mounted to a 3-axis translation stage (Aerotech ANT-50L) to position at the laser focus and for lateral position control. A circular ND filter wheel was used to select the pulse energy. If multi-pulse experiments were being performed the shutter was simply opened for duration required to let the desired number of pulses through to the sample.

The methodology followed for an ODB experiment is as follows; after laser beam characterization and diagnostics, power calibration of the photodiode is done by placing a power meter (PM100USB) after the objective and creating a voltage-power calibration curve. After calibration the sample is then placed on the translation stage, and tilted such that the beam is incident normal to the film surface and placed at the laser focus. For single or multi-shot experiments an area of film is exposed, and the sample is translated to a fresh spot of film for the next exposure. Typically, 5 exposures are made for each experimental condition.

For line patterning, the laser was operated at 100 kHz and focused through the 0.9-NA objective, with the translation speed set at 100 $\mu m/s$. High NA experiments have a significantly shorter Rayleigh range than the lower-NA experiments (< 500 nm in our experiments). The intrinsic drift of the Aerotech translation stage was experimentally determined to be insufficient for the demands of the experiments. This required the use of a capacitance sensor (Lion Precision CP-102) as the primary feedback mechanism for the stage instead of the built-in Renishaw RG24B encoder. The capacitance sensor was placed to sense a second kinematic mount on the same translation stage as the sample. This experimental setup is displayed in Figure 2-4.

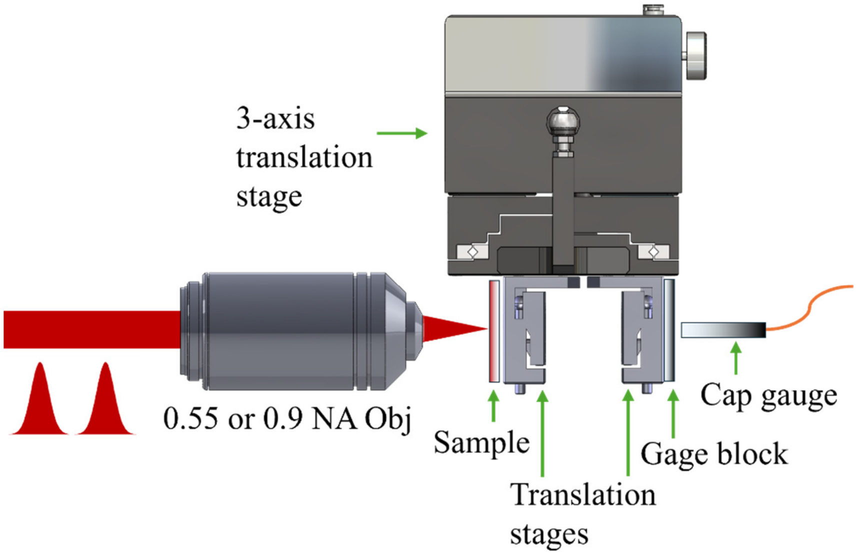

Figure 2-4: Capacitance sensor feedback system for maintaining sample position at the laser focus for high-NA experiments

For experiments where the beam spot size was changing it was more expedient to image the sample from behind. The experimental setup was kept the same when the light polarization on the sample was being rotated. This arrangement is shown in Figure 2-1.

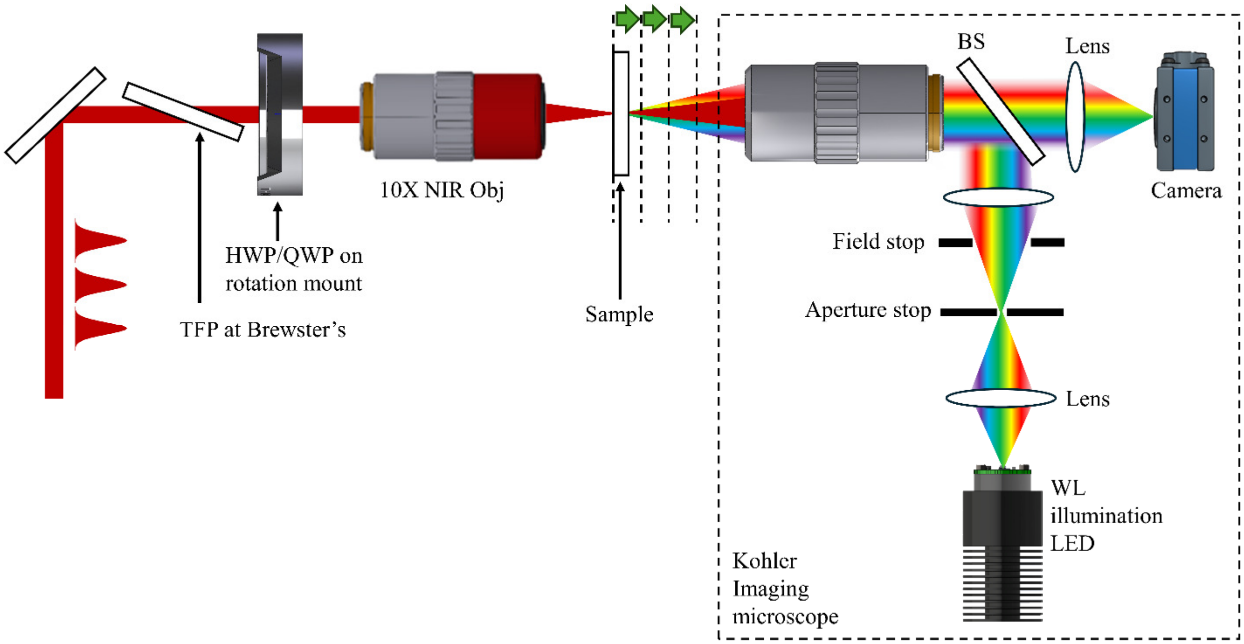

Figure 2-5: Imaging in transmission for polarization dependence and spot size dependence experiments.

For experiments requiring fine control on the incident polarization, the beam is directed through a thin film polarizer (TFP, Eksma 420-1286) and a half-wave plate if linear polarization is being rotated or a quarter-wave plate to control linear or circular polarization, respectively. The beam is focused on the sample through the NIR 0.26NA objective. In both cases of imaging the sample, whether it is imaging in reflection as in Figure 2-3 or in transmission as in Figure 2-5, Kohler illumination was found to be critical in optimizing image contrast. Often a slight phase-contrast induced due to the Kohler imaging setup allowed critical features to be located, such as femtosecond exposed areas on hBN films which were normally impossible to locate with DIC imaging.

2.3 Material Characterization

2.3.1 Optical microscopy/Differential Interference Contrast (DIC) Imaging.

Ablation features such as holes and cut-lines in TMD materials were imaged using optical microscopy on an Olympus BX-51 TRF optical microscope. A suitable choice of substrate, such as on a silicon wafer with a 90-nm SiO_2 layer on it, can enhance the optical contrast between the film and the substrate. One group explicitly calculates this increase in contrast based on the film and substrate refractive indices (49). A 90-nm SiO_2-Si substrate also aids ablation by increasing the internal field within the 2DM, lowering the incident fluence required to ablation (39). The situation is more difficult in the case of hBN. The large bandgap of hBN makes ablation of the film impossible before ablation of the substrate itself, which has been demonstrated before (44). This necessitates the use of more robust substrates with large bandgaps such as fused SiO_2 ($E_g > 5.8$ eV, more discussion on material bandgaps later) or Al_2O_3 ($E_g \sim 9.3$ eV) that can withstand the high fluences incident on them. Unfortunately, such substrates present extremely poor optical contrast that results in the film being impossible to discern under normal optical microscopy (OM). Any ablation features made under femtosecond exposure are not visible in situ, a fact that increases the difficulty of conducting experiments on hBN since one is, quite literally, shooting in the dark. Differential Interference Contrast (DIC) imaging (also referred to as Nomarski microscopy) provides improved contrast compared to OM and makes the identification of ablation features possible, such as seen later in the work in Figure 3-10. Thus, any experiments involving ODB had to be carefully planned and performed. After femtosecond exposure the sample would be measured under DIC.

2.3.2 Atomic Force Microscopy.

Atomic Force Microscopy (AFM) is an imaging technique often utilized to measure and obtain height data for microscopic features. The operating principle can vary based on operating modality of the AFM. The mode used for our experiments is Tapping Mode (TM). A small silicon 'tip' on a tiny cantilever is oscillated back and forth using a piezoelectric drive. A laser beam is illuminated on the back of the tip and the back-reflected laser is detected by a photodetector. The signal on the photodetector oscillates as the tip oscillates. The tip is brought into proximity of the sample to be measured and the laser back-reflected signal's amplitude and phase change is recorded and used to derive the distance the sample height. The AFM tip is then translated laterally across the sample while the tip oscillates and 'taps' the sample, and a height map is generated from the resulting variation of the signal with respect to the position of the tip, creating an AFM image.

Other operating modes of AFM are Contact Mode (CM) and PeakForce (PF) modes. Contact mode AFM involves the tip not oscillating/tapping the surface of the sample but instead dragging across the sample, conforming to the morphology of the surface. This operating mode has the potential to damage the monolayer films of our samples that are held onto the substrate simply by Vanderwaal's interactions and is hence not used here. Peakforce (PF) mode measures the force exerted on an AFM tip that operates in tapping mode and is a function of more advanced AFMs that were not available to us. PF imaging can translate to more accurate thickness measurements of the monolayer films; Shearer et al. used PF to measure the thickness of graphene accurately (50).

The thickness of monolayer samples can be challenging. The amount of force the AFM tip applies can change the thickness measured, possible due to water 'adlayers' between the monolayer film and the substrate. In addition, nanometric wrinkles in the film (such as those seen for graphene (50)) can affect the thickness measurement. Simply taking cross-sectional line profiles across a film edge can be challenging due to noise in the instrument. Shearer et al. use an alternative measurement technique where they create histograms of the AFM data on the film and on the bare substrate and fit it using gaussian distribution (50). The difference in the center position of the gaussians is taken to be the film thickness. A similar approach will be taken later on in the work (section 3.3.1)

The thickness of 2D films is a somewhat contested topic that makes the accurate determination of monolayers difficult. To determine film thickness for our hBN/fused silica samples, the height data from the area outside the ablation hole was averaged (Figure 2-6, left) to get an average height of the film. The same was done to the height data of the area inside the ablation hole (Figure 2-6, right) and the difference was taken to yield a height of ~0.36 nm. This corresponds very well to thickness of a monolayer hBN film in the literature.

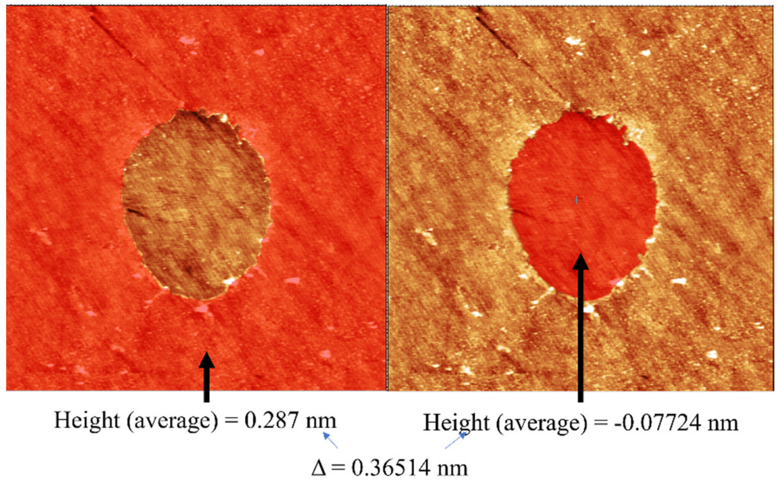

Figure 2-6: AFM image of an ablation hole in hBN on fused silica made at $1.27F_{th}$..

The literature reports a range of heights for monolayer films that varies from 0.3 – 2.8 nm (44). The same is true for graphene. Literature reports efforts undertaken to accurately determine the thickness of graphene using multiple AFM modalities (50, 51). This can be due to a thin water layer adsorbed onto the substrate underneath the 2D film (50). Regardless, the thickness measurements made in this work are within literature variation for single layers.

2.3.3 Raman and photoluminescence (PL) spectroscopy.

Raman and photoluminescence spectroscopies are useful tools for material characterization. For this purpose a home-built Raman microscope was assembled, as shown in Figure 2-7.

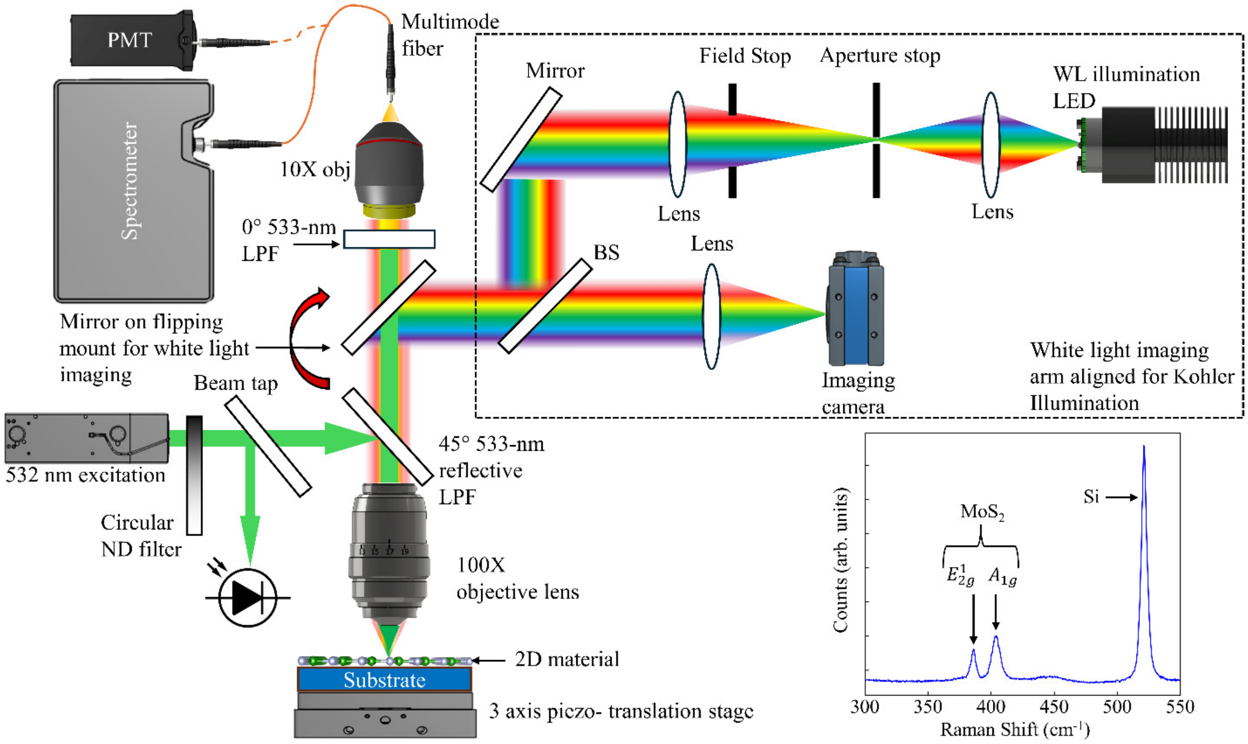

Figure 2-7: Raman and photoluminescence (PL) spectroscopy experimental setup. (inset) Raman spectrum taken of MoS_2 monolayer on a 90-nm SiO_2/Si.

A 532 nm diode-pumped solid stage (DPSS) laser is used for material excitation (Lasos GLK 3250 T01). A circular ND filter is used to adjust the laser power and a tap samples the beam for continuous laser power monitor via a photodiode. A 532 nm long-pass filter (Iridian ZX827) directs the excitation beam through an objective lens (Olympus 100X) that is used simultaneously for sample excitation, white light imaging and signal collection. The back-scattered light, collected by the 100X objective and further filtered to remove the excitation light by a 0° 532 nm long-pass filter (LPF), is then coupled in to a 200 μm core-diameter multi-mode fiber that is then coupled into an imaging spectrometer (Horiba iHR-500) for spectral analysis. The sample is mounted on a 3-axis piezo-actuated translation stage. To accurately position the sample and select the position from where Raman signals are to be collected, white light imaging is set up in a Kohler illumination configuration. When positioning the sample, a mirror on a flipping mount directs the white light toward the objective.

The Raman signature exhibited by hBN is quite weak and requires high excitation powers (~ 5 mW) and large integration times (~ 20 mins). To further increase the signal, a $1/e^2$ spot radius of ~ 1.16 μm is used for the excitation beam. The horizontal and vertical spot radii are measured via a knife edge measurement, displayed in Figure 2-8.

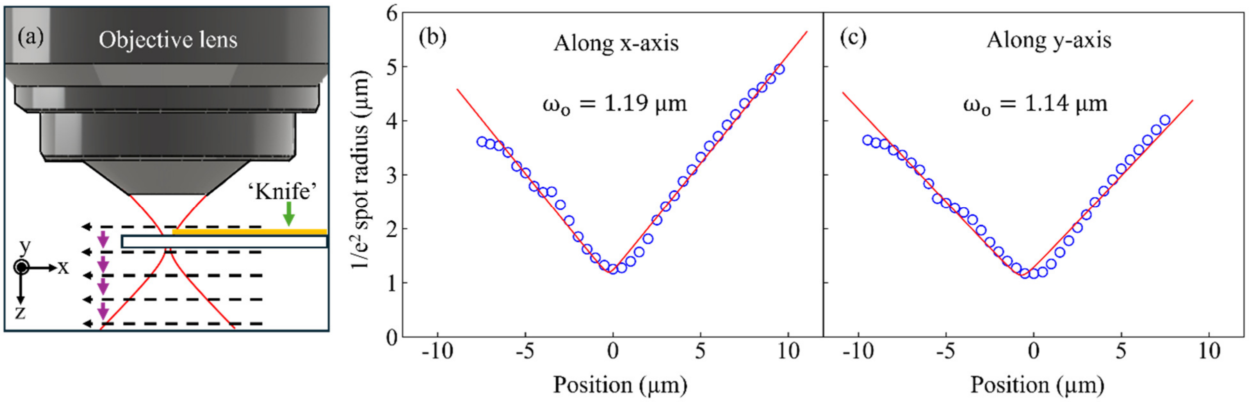

Figure 2-8: (a) Schematic of the knife edge measurement of the $1/e^2$ beam spot radius Raman system. (b) and (c) results from the knife edge measurement.

A borosilicate (Schott D263M) glass coverslip with 100-nm thick Au film deposited on it is used as a 'knife-edge.' The 532-nm reflection from the Au film is coupled into the fiber from the Raman system and connected to the PMT (the 0° LPF filter removed was removed to get adequate signal). As the edge of the Au film is scanned laterally across the cross-section of the laser beam (along x or y - axis in Figure 2-8(a)) at a known speed the signal on the detector creates an erf-function signal that is fitted to extract a $1/e^2$ waist radius. The knife is then shifted axially w.r.t. to the laser beam (along z-axis in Figure 2-8(a)) and scanned again. The spot radius vs. position data is fitted with a hyperbola to obtain the minimum spot radius at the beam waist.

2.3.4 2D photoluminescence (PL) imaging

2D photoluminescence (PL) images are collected by adding an additional 560-nm LPF before coupling into the fiber and switching the fiber to couple light onto a photomultiplier tube (Hamamatsu R-928). Thus, the resulting images are spectrally integrated and are the result of PL from optically bright mid-gap defects in the films.

2.3.5 UV-VIS-NIR absorbance spectroscopy

Further characterization of the nature of defects in hBN was done via measuring the UV-VIS-NIR absorbance spectrum via a Shimadzu UV2600 spectrophotometer.

2.3.6 Scanning electron microscopy (SEM).

Scanning electron microscopy (SEM) is a powerful tool for imaging features in metallic and conductive materials. An electron beam is incident in the sample and scattered electrons are collected via electron lenses. SEM is typically unsuitable for imaging semiconducting or insulating materials due to charging of the material. In this work it was found that a combination of a low accelerating voltage (1 to 5 kV) and suitable aperture size (10 µm) can succeed in imaging 2DMs without metallization. The instrument used in this work was a Raith 150 SEM.

2.3.7 Sample preparation.

In the case of TMD films, highly oriented monolayer MoS_2 films and WS_2 flakes were grown by chemical vapor deposition (CVD) on Al_2O_3 substrates following the procedure outlined in reference (52). Monolayer growth was confirmed via AFM measurements, PL spectra (the location and amplitude of the C exciton peak in MoS_2 for monolayer is particularly telling) and Raman spectroscopy (location of the A_{1g} and E_{2g}^{1} peaks). All films were transferred to target substrates as required, which included 70 nm Au film, Al_2O_3, borosilicate glass (Schott D263M), 90 nm SiO2/Si, and two different DBR substrates. The transfer process is also outlined in reference (52).

In the case of hBN films, The hBN monolayers were grown on 500 nm-thick Cu(111) on c-plan Al_2O_3 substrates by hot-wall CVD using ammonia borane (97%) as the precursor. The as-grown monolayer hBN film was detached from the Cu(111)/Al_2O_3 substrate by electrochemical delamination using a poly(methyl methacrylate) (PMMA) film and a thermal release tape (TRT) as the supporting layer. After detachment, the TRT/PMMA/hBN stacked film was placed onto a fused silica substrate. The TRT and PMMA film were finally removed by baking and hot acetone, leaving behind a monolayer hBN film on fused silica. PMMA residue was further removed using rapid thermal annealing at 400 ◦C for 1 min under a 6 torr forming gas (5% H2 and 95% nitrogen). Further details of the growth and transfer can be found in (53).

2.3.8 Exfoliation of bulk materials.

The recipe followed in this work was like the one described in (54). First, the target substrates (fused SiO_2 or Al_2O_3 in this case) were cleaned using traditional optics cleaning methods such as blowing compressed air on it followed by the ‘drop-and-drag’ method with acetone or methanol. Afterwards the substrates were sonicated for 60 minutes in an acetone bath to remove any large particulates that might be ‘hard-stuck’ onto the substrates. Simultaneously while the sonication is occurring, adhesive tape is used to exfoliate the target material samples. Adhesive tape was attached to a table and the bulk material was pressed onto the tape, pressed down for 30s, then lifted off, leaving behind multilayer flakes onto the tape. This initial piece of tape is referred to as the ‘mother tape’. Another piece of tape is then pressed onto the mother tape, pressed for 30s, then peeled to deposit a thinned flake onto this second tape, which is referred to here as the ‘depositing tape’. Thinning on the depositing tape is performed by pressing and peeling on subsequent clean pieces of tape (a third tape, separate from the mother tape). This tape is then transported to a clean-room along with the cleaned substrates, where the substrate undergoes further cleaning in an O_2 plasma at ~150W for ~ 5 mins. Plasma cleaning is useful in that it removes any molecular or water molecule adsorbates on the substrate. Immediately after taking the samples out of the plasma cleaner the depositing tape with the thinned 2D material is pressed onto the prepared substrate using a flat plastic scraper to ensure as smooth a contact as possible. The samples are then placed inside a vacuum chamber under a weight and left under a partial low vacuum for ~35-40 mins. This is to ‘pull’ any air bubbles between the film and the substrate out of the film. Empirically the flake yield was found to improve after such a vacuum treatment. After the vacuum treatment the sample is placed onto a hotplate @ 100°C for ~2 mins, similar to the methodology of (54), after which the tape is peeled to reveal the final 2DM on the target substrate.

Before target materials such as $Mg(OH)_2$ or $CrCl_3$ were exfoliated, the process was first tested on highly oriented pyrolytic graphite (HOPG) to see whether single layer graphene could be isolated. It is important to note that the number of thinning steps when peeling the material ultimately determines the thickness of the material. Raman signatures identified small flakes as single-layer graphene. The size of the single layer flakes was too small ($< 10\ \mu m^2$) to conduct meaningful ODB experiments on, despite multiple tries and variations on the recipe used. In this case a compromise had to be made where multilayer flakes were targeted if the E_g was still of a direct nature (more discussion in section 4.4.1).

3 OPTICAL DIELECTRIC BREAKDOWN (ODB) STUDY OF MoS_2 AND hBN

As delineated in chapter 1, it is interesting to examine the strong-field interaction of different 2DMs and examine the feasibility of laser-direct writing (LDW) in fabricating nano-patterns out of such materials. The following chapter begins with an exploration of the single pulse induced optical dielectric breakdown (ODB) of the monolayer transition metal dichalcogenide (TMD) MoS_2. The etalon interference effect of the substrate on the ODB threshold of the film is investigated and preliminary sub-micron LDW of MoS_2 is demonstrated. Since LDW involves the exposure of the film to multiple pulses incident on the material one after another, accumulation effects of laser-induced defects on the breakdown threshold on MoS_2 and WS_2 are studied. The ODB of the wide bandgap insulator hexagonal boron nitride (hBN) is studied next. The favorable ODB properties of hBN are characterized and subsequently harnessed in its patterning using LDW. Impressive sub-100 nm resolution of features is achieved via careful control of the laser exposure of the film.

3.1 Single shot breakdown experiments of MoS_2

As noted in chapter 1, after graphene, MoS_2 is one of the most studied 2DMs. Various studies of the ODB of MoS_2 have been reported in the literature but most have presented wide variations in the breakdown thresholds. Paradisanos et al. looked at the multi-shot degradation of exfoliated monolayer and bulk MoS_2 and reported single-shot ablation thresholds based on the appearance of submicron-sized distortion in film (55). Pan, Y. et al. studied the laser-induced sub-wavelength ripple formation on a natural bulk MoS_2 crystal which they attributed to spallation and sublimation of the crystal caused by laser induced surface plasmon polaritons (56). Similarly, Pan, C. et al. investigated breakdown mechanisms of bulk MoS_2 under intense femtosecond excitation and determined that the ablation was mediated by sublimation at weak pumping and melting at strong pumping (57). Most of these efforts were performed on bulk MoS_2, and a rigorous investigation of the ODB threshold fluence and ultrafast laser patterning for monolayer TMDs has not been demonstrated and will be undertaken in this work.

Regarding laser patterning, it should be noted that sublimation of monolayer MoS_2 on a SiO_2/Si substrate with a 200 nm spatial resolution has been demonstrated before using continuous-wave (CW) 532-nm sources (58). The primary caveat of using CW sources is that the patterning speed is slow due to its photothermal nature. Lin et al. were able to increase the throughput of CW laser thinning by patterning on an opto-thermo-plasmonic substrate (layer of Au nanoparticles), but this carries the caveat of needing to then transfer the patterned 2DM to the final target substrate 20. Using ultrafast sources is desirable due to the minimization of thermal effects by virtue of the laser pulse-width and the electron-photon interactions being faster than typical electron-phonon coupling timescales. Since many applications require a supporting substrate, understanding its effect on the laser ablation of 2D materials is important. Although ultrafast laser ablation of graphene has been extensively studied, the role of the substrates is still not clear. The reported ablation thresholds from many studies made by similar pulse widths (~50–100 fs) and wavelengths (~800 nm) differ by one order of magnitude among suspended graphene and graphene supported by borosilicate glass, Al_2O_3, and 285 nm SiO_2/Si substrates (59-64). Such variation has not been rigorously examined and the substrate has primarily been relegated to the role of heatsink. This has often been the explanation for why CW laser thinning of multi-layer graphene and MoS_2 self-terminates at monolayers (58, 65). Other reports have also observed that the ablation threshold for both femtosecond and CW excitation are lower for suspended 2D materials than those supported on a SiO_2/Si substrate, which was again attributed to heat dissipation through the supporting substrates (64, 66). Optically, substrates are known to enhance the light outcoupling of 2D materials through the etalon effect. For SiO_2/Si substrates, the Raman scattering was shown to strongly depend on the SiO_2 thickness for graphene (67), which led to the optimization of both the Raman scattering and photoluminescence of WSe_2 by controlling the SiO_2 layer thickness where the largest enhancement occurred for a SiO_2 thickness of about 90 nm for 532 nm excitation (68). Similar enhancement for Raman scattering, photoluminescence, and second harmonic generation has been demonstrated in the literature by engineering distributed Bragg reflector (DBR) substrates for 532-nm excitation (69). Improved optical contrast of graphene and MoS_2 has also been achieved by designing multilayer heterostructure substrates where an optical contrast of 430% was obtained for monolayer MoS_2 (70, 71). The etalon interference effect has been previously shown to modulate the laser thinning efficiency of multilayer graphene (65) but has never been studied for the laser ablation of 2D materials. In this work, the ODB of monolayer MoS_2 on a variety of common substrates was studied. In this work the ODB process was demonstrated to possess both high speed (~5 mm/s) and high resolution (~250 nm with a 0.55 NA objective at 800 nm in the case of MoS_2, although finer can be achieved). Moreover, the influence of substrates on the breakdown threshold fluence F_{th} was investigated, both when using single laser pulses and when creating line scans using multiple pulses. It was shown that the femtosecond laser ablation of transferred monolayer MoS_2 is adiabatic, where the heat dissipation through the supporting substrates is negligible, and the variation in F_{th} among substrates can be largely explained by the substrates' etalon effect. Based on our finding, an all-dielectric DBR substrate was realized to reduce F_{th} by 7× compared to that of sapphire to enable laser patterning using low-power femtosecond oscillators. Furthermore, we introduced an intrinsic ablation threshold fluence $F_{th}^{\text{int}r}$ parameter that is the substrate independent and corresponds to the incident fluence required for the material breakdown of suspended film without a substrate and hence is intrinsic to the film. A zero-thickness approximation is also introduced to substantially simplify the calculation of the etalon effect for ODB. Combined with the knowledge of $F_{th}^{\text{int}r}$, this makes the incident F_{th} on any substrate predictable.

3.1.1 Zero-thickness approximation.

Previous studies on the etalon effect of monolayer 2D materials focused on engineering the Raman scattering, photoluminescence, and second-harmonic generation by optimizing the internal field at the excitation wavelength and the outcoupling efficiency at the emission wavelength (67-69). As a result, the theoretical enhancement can only be calculated computationally. For ODB, only the excitation enhancement matters, and the internal field E_{2DM} at the excitation wavelength can be obtained analytically. The substrates used in this study include sapphire (Al_2O_3), borosilicate glass, a 70 nm thick gold (Au) film on a glass (Schott D263M) substrate, 90 nm SiO_2/Si, and two custom designed DBR substrates: one DBR substrate (DBR800(+)) that targets maximal intensity enhancement and the other (DBR800(-)) that targets maximal intensity suppression. The system can be modeled as an asymmetric etalon composed of air, a 2D material, and the substrate, as displayed in the schematic in Figure 3-1(a). If the effective reflection coefficient between the monolayer and the substrate $r_{1s} = r_0 e^{i\phi}$ is known, then the spatial distribution of the electric field inside the monolayer $E_{2DM}(x)$ can be calculated analytically by using the familiar Fabry-Perot style development of accounting for multiple reflections between the interfaces to give;

$$E_{2DM}(x) = E_{incident} t_{01} \left(\frac{e^{i\beta_1 x} + r_{1s} e^{i\beta_1 (2d_1 - x)}}{1 - r_{1s} r_{10} e^{i2\beta_1 d_1}} \right) \tag{3.1}$$

Since monolayer 2D materials are much thinner (<1 nm thick) than the 800-nm wavelength pulses used here, the distance $d_1 \to 0$, and a zero-thickness approximation (ZTA) can be introduced. This simplifies the internal field $E_{2DM}(x)$ to become.

$$E_{2DM}(x) \approx E_{2DM}^{ZTA} = E_{inc} t_{01} \left(\frac{1 + r_{1s}}{1 - r_{1s} r_{10}} \right) \tag{3.2}$$

Where $E_{incident}$ is the incident electric field, t_{ij} and r_{ij} are Fresnel transmission and reflection coefficients for the i_{th} to the j_{th} medium, respectively. For simple substrates such as bulk Al_2O_3, fused SiO_2 glass, or a thick Au film, r_{1s} is simply the Fresnel reflection coefficient between the film and the substrate, and the internal field E_{2DM} within the 2D material simplifies to;

$$E_{2DM}^{ZTA} = E_{inc} \left(\frac{2}{1 + n_s} \right) \tag{3.3}$$

where n_s is the substrate complex refractive index. In the case of more complicated substrates such as SiO_2/Si substrates, or distributed Bragg reflector substrates that are composed of multiple layers or materials with different refractive indices, the contribution of each layer in the stack needs to be accounted for. In that case, the reflection and transmission at each material interface needs to be accounted for to calculate the total field within the 2DM film. This is illustrated in Figure 3-1(b) and it is convenient to use transfer matrix methods (TMM) to calculate E_{2DM} for more complex substrates such as a distributed Bragg reflector (DBR) that is composed of multiple layers of alternative refractive index materials. Open source TMM code implemented in Python for coherent light was used in the practical implementation of calculating E_{2DM} . From the internal field the average intensity in the 2DM can be found according to the equation shown below.

$$\left|E_{2DM}\right|^2 = \frac{1}{d_1}\int_0^{d_1} E_{2DM}^{*}(x)E_{2DM}(x)dx \tag{3.5}$$

From this an enhancement factor can be found.

$$\eta^2 = \frac{\left|E_{2DM}\right|^2}{\left|E_{incident}\right|^2} \tag{3.6}$$

In summary, the multiple reflections on multiple interfaces cause interference within the 2DM and thus a different intensity within the film. This enhancement factor allows for the computation of the internal fluence that the 2DM actually experiences and thus find the intrinsic threshold fluence of the material. This intrinsic threshold fluence would be the same as the threshold of suspended 2D material. This intrinsic fluence can be found by the equation below.

$$F_{th}^{\mathrm{int}r} = \eta^2 F_{th} \tag{3.7}$$

3.1.2 Intrinsic breakdown threshold fluence of MoS$_2$.

To experimentally investigate the effect of the etalon in the ODB of 2DMs the representative material that was chosen was MoS$_2$ since the literature on it is extensive. Due to the simplicity of the formulation of the etalon effect, the results are expected to apply to other 2DMs as well. The MoS$_2$ monolayer thickness was confirmed using Raman spectroscopy, PL and AFM and clean laser ablation was confirmed using OM and AFM (the laser did not damage the underlying substrate) (39). The methodology followed to extract the breakdown threshold was by exposing the material to single laser pulses at different pulse energies. The sample was translated laterally to select a fresh spot of film for each laser shot. For each laser pulse energy 5 separate exposures were made (translating the stage each time) to average out any spatial inhomogeneity in the film. An example is shown in Figure 3-1(a), where single exposures at 5 pulse energies were made for MoS_2 film on a 90-nm SiO_2/Si substrate. The pulse energy increases going from the bottom to the top and are 11.7, 13.2, 14.7, 16.5, 18.6 and 21 nJ with a 1/e^2 derived radius of ~ 3.5 µm. The holes made by each laser exposure were measured via OM as described section 2.3.1. The hole area vs pulse energy data is fitted via the equation $A=(\pi/2)\omega_o^2\ln(E/E_{th})$ that was first proposed by Liu (72), where E is the pulse energy, E_{th} the energy threshold and ω_o the 1/e^2 beam spot radius. Once the spot radius is extracted it is simple to extract the fluence incident on the material via $F=\dfrac{200E}{\pi\omega_o^2}$ in units of mJ/cm^2, where E is in nano-joules and ω_o in µm. Thus, the fluence threshold F_{th} can then be determined by changing the horizontal axis to fluence and fitting to $A=(\pi/2)\omega_o^2\ln(F/F_{th})$ with the same ω_o.

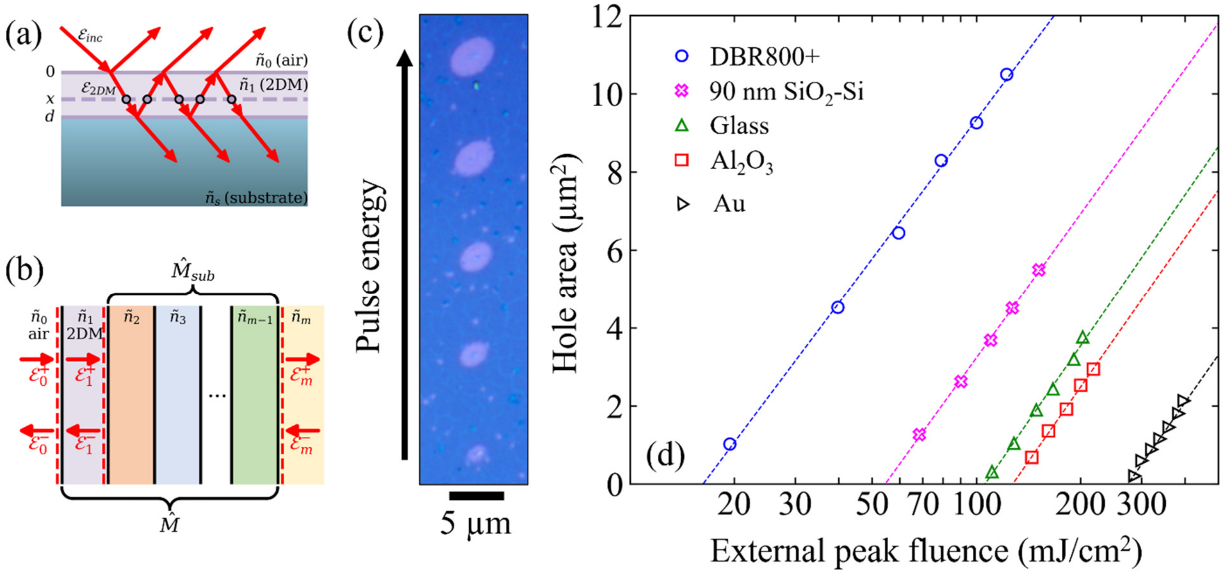

Figure 3-1: (a) Schematic of the etalon effect for a 2DM on a simple substrate such as Al_2O_3. The multiple reflections in the 2DM give rise to the etalon effect. (b) Schematic for a 2DM on a complex substrate such as a distributed Bragg reflector (DBR). Transfer matrix methods (TMM) are more appropriate for such situations. (c) Holes made in MoS_2 monolayer on a 90 nm SiO_2/Si substrate with increasing pulse energies (going bottom to top). (d) ODB thresholds of MoS_2 monolayer on different substrates.

Experimentally, F_{th} for MoS_2 were determined for different substrates and are shown in Figure 3-1(c). The determined thresholds were found to be; Al_2O_3 substrate (130 mJ/cm^2), Au (276 mJ/cm^2) susbtrate, D263M glass (110 mJ/cm^2), 90 nm SiO_2/Si (54 mJ/cm^2), and the DBR800(+) substrate (16 mJ/cm^2) were determined using the method described above. It should be noted that the spot radius for the experiment in Figure 3-1 was smaller around ~ 2.2 µm. The large variability of the threshold for the same material prepared and experimented on under identical conditions clearly indicates that there is a large effect of the substrate on F_{th}. If the observed variation in F_{th} is purely due to the etalon effect, then F_{th}^{intr} should be a constant and F_{th} should be inversely proportional to the η^2 in the MoS_2 monolayer. Put another way, the product of the measured F_{th} and the computed η^2 should give the same number. The computed enhancements factors (using the ZTA for the simple bare substrates and the full TMM calculation for the complex substrates such as the DBR) for each substrate are; $\eta^2_{Al_2O_3}$ = 0.53, η^2_{Au} = 0.16, η^2_{D263M} = 0.63, η^2_{90nm} = 1.14, and $\eta^2_{DBR800+}$ = 3.97. From this the extracted intrinsic thresholds are 68.9 mJ/cm^2 for Al_2O_3, 61.6 mJ/cm^2 for the 90 nm SiO_2/Si, 69.3 mJ/cm^2 for the D263M glass, 63.52 mJ/cm^2 for the DBR800(+), and 44.16 mJ/cm^2 for the film on the Au. Aside from the result for the Au the resulting $F_{th}^{\mathrm{int}r}$ confer good agreement. The average $F_{th}^{\mathrm{int}r}$ ~ 66 mJ/cm^2 and the standard deviation is <6%. The anomalous result was later deduced to originate due to plasmonic enhancement effects via FDTD simulation (39).

The excellent agreement for all these substrates demonstrates that the dominating effect of these substrates in the single-shot ablation of TMDs is the etalon effect, even though their thermal conductivities vary over two orders of magnitudes (73). This result may not be too surprising, given that the total energy input for single-shot ablation is small such that substrate heating is negligible, regardless of their differences in thermal conductivities. Since the end goal here is patterning, which will require exposure to multiple pulses, a process that typically uses high-repetition- rate femtosecond lasers, quasi-CW laser heating of the MoS_2 film is expected such that heat transfer to the substrates may occur during ablation. To investigate this conjecture, lines were cut into the where the MoS_2 film is exposed to an 80 MHz pulse train from an ultrafast oscillator (Spectra physics Tsunami, which is a 80 MHz oscillator, using the same system described in section 2.2), while translating the sample at a constant speed.

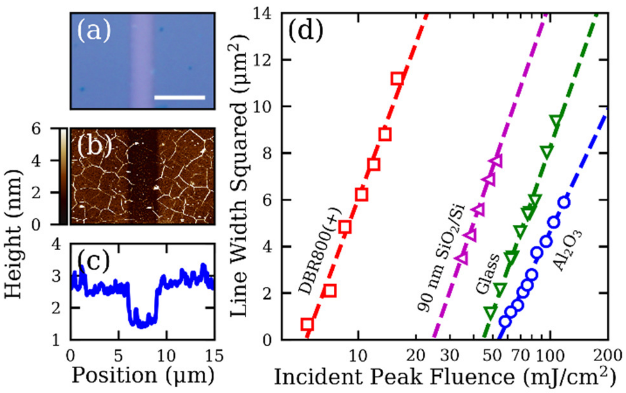

Figure 3-2: (a) OM image of a line cut into MoS_2 on 90 nm SiO_2/Si. (b) AFM image of the line in (a). (c) Corresponding line profile of (b) via a computed via vertical column average. (d) ODB thresholds for multiple pulses via line-scanning experiments for MoS_2 on different substrate.

Figure 3-2 (a)–(c) show respectively an optical microscope (OM) image, AFM height, and AFM cross-sectional profile of a line scan with a fluence of 34 mJ/cm^2 and a scan speed of 100 μm/s on the 90nm SiO_2/Si substrate. Here, clean removal of monolayer MoS_2 is also observed. Like the single-shot trials in Fig. 2c, a line-scan ablation threshold F_{th} for the MoS_2 film can be extracted using a method very similar to that for the single shot holes by fitting to the line width (D) squared in the equation $D^2 = (\pi/2)\omega_o^2 \ln(F/F_{th})$. Figure 3-2(c) shows the data and the fits for various substrates, taken with a fixed scan rate of 100 μm/s and a focused laser spot radius of 2.0 μm. The extracted line-scan F_{th} of MoS_2 are 54, 49, 25, and 5 mJ/cm^2 for Al_2O_3, glass, 90 nm SiO_2/Si, and DBR800(+) substrates, respectively. Analogous to the single-shot thresholds, the intrinsic F_{th} in the case of line scans is found to be $F_{th}^{\text{int}\,r} \approx 26$ mJ/cm^2 for monolayer MoS_2 at a scanning speed of 100 μm/s for each material. The fact that all measured threshold a similar number for each material is good evidence that even for multiple pulse exposure in line scanning experiments ablation is still largely governed by the etalon effect. This indicates that these substrates behave as very poor heat sinks for the ultrafast laser ablation of 2D materials, irrespective of the substrates' thermal properties. The process of ODB appears to be minimally affected by thermal effects and thus appears to be adiabatic. This adiabaticity can be attributed to the very low thermal boundary conductance (TBC) between MoS_2 and the substrates. Literature reports place TBC values between 0.1 and 34 MW/m^2/K for MoS_2 on SiO_2/Si substrates (74, 75) and between 19 and 38 MW/m2 /K for Al_2O_3 substrates (76). Additionally, mechanically exfoliated and as-grown MoS_2 monolayers on a SiO_2/Si substrate. are shown to have similar TBC values (74). Thus, as-grown films should have the same behaviors as transferred films. This finding of adiabaticity is in direct contrast to multiple reports that the substrates serve as a heat sink for the laser processing of 2D materials (58, 64, 66, 77). For example, Yoo et al. reported F_{th} = 98 mJ/cm^2 for graphene on 285 nm SiO_2/Si and F_{th}<43 mJ/cm^2 for suspended graphene in single-shot femtosecond laser ablation (64). They attributed this difference to the adiabatic condition of suspended graphene where heat dissipation through the substrate is forbidden. Alternatively, based on the etalon effect, η_{ZTA}^2 is 0.2 and 1 for 285 nm SiO_2/Si and air substrates, respectively. If the threshold for graphene is F_{th} = 98 mJ/cm^2 on the 285 nm SiO_2/Si substrate, then the threshold for suspended graphene should be F_{th} ~ 20 mJ/cm^2, and this number is consistent with the F_{th} < 43 mJ/cm^2 number reported by the Yoo et al.. Moreover, the knowledge of $F_{th}^{\mathrm{int}\,r}$ and η_{ZTA}^2 (i.e., Fig. 1a) makes F_{th} predictable for any substrate, according to Eq.1.6 . For example, given that F_{th} = 54 mJ/cm^2 and η_{ZTA}^2 = 1.14 for the 90 nm SiO_2/Si substrate, the predicted threshold for the DBR800(+) substrate with η_{ZTA}^2 = 3.97 is F_{th} = 15 mJ/cm^2, which matches very well with the measured threshold of 16 mJ/cm^2 found in the experiment.

3.1.3 Ultrafast laser patterning.

For laser patterning applications, the patterning speed and resolution are important performance metrics. Given that SiO_2/Si substrates are commonly used for field-effect transistors, Figure 3-3 shows the ablated line width in MoS_2 on the 90 nm SiO_2/Si substrate as a function of the scan rate with a constant fluence of about 46 mJ/cm^2 and a 0.26 NA focusing objective 10. As the scan rate increases from 1 µm/s, the line width decreases from 8.7 µm before leveling off at 2.9 µm at 5 mm/s. The leveling off at high scan rates is due to the mechanical instability of the translation stage used here, where the stage vibrates resulting in larger widths and uneven lines.

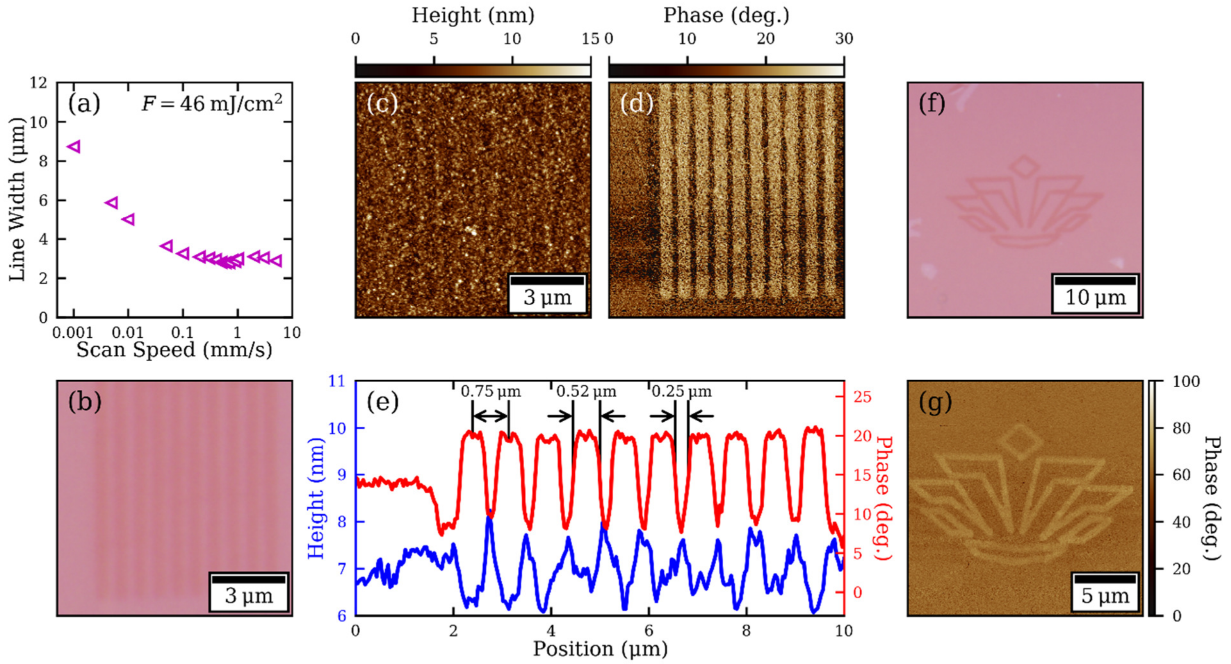

Figure 3-3: Ultrafast laser patterning (a) Line width vs scan speed made with a fluence of 46 mJ/cm^2 on the DBR800+ substrate (b) Corresponding OM image of the lines in (a). AFM height (c) and phase (d) images of line made with a decreasing hatching distance between the lines. (e) Vertically averaged line profiles of (c) and (d). (f) OM image of the university's crown symbol patterned into MoS_2. (g) AFM image corresponding to (f).

Better resolution might be achieved by utilizing galvo-scanner and a telecentric objective lens setup to translate the laser beam itself instead of the translation stage used here. Nevertheless, Figure 3-3 clearly demonstrates high-speed line patterning of TMDs. This translates into increased patterning efficiency of an ultrafast source compared to a CW source: with a scan rate of 5 mm/s, material can be removed at a rate greater than 14,000 μm^2/s by ultrafast lasers, whereas CW laser thinning can only pattern monolayers at a rate of 8 μm^2/min (58). To demonstrate sub-micron patterning resolution, Figure 3-3(b)-(e) shows an array of ablated lines in a MoS_2 film on the DBR800(+) substrate obtained with a laser spot diameter of ~1.3 µm using a 50×, 0.55 NA focusing objective. The AFM height image has poor quality due to the surface roughness of the DBR800(+) substrate (39), while the AFM phase image clearly resolves the grating pattern where an average trench width of 0.52 µm and ribbon width of 0.25 µm are measured. To demonstrate laser micro-patterning, the UNC Charlotte crown logo was patterned into a MoS_2 film on the DBR800(+) substrate as shown in Figure 3-3(f). The total size of the pattern is 20 µm laterally and was engraved using a fluence of 10 mJ/cm^2 and a low feed rate of 3 µm/s to avoid skewing the pattern (39). The thicknesses of the lines in the logo were found to be around 0.7 µm as measured by the AFM phase mapping. For practical applications, cost is also an important consideration. Although Figure 3-1(d) and Figure 3-2(d) have demonstrated femtosecond ablation and patterning of MoS_2 on several substrates, the large field enhancement of the DBR800(+) substrate only requires pulse energies as low as 1 nJ for single-shot ablation and on the order of 100 pJ for line scans, as demonstrated in Figure 3-3. This pulse energy corresponds to an average power of 80 mW which is readily available from compact femtosecond oscillators (39). With a proper design, the substrate could be engineered to enhance both the patterning process and the light-coupling performance of the resulting device.

Alternatively, the patterned film can be transferred to other substrates (78, 79). Since the process of laser patterning exposes the material to trains of ultrafast laser pulses, any laser-induced defects added to the material by an incoming pulse can affect the light-matter interaction of the subsequent pulse, a phenomenon known as incubation. It is important to investigate the behavior of 2DMs under such strong, repeated exposures.

3.2 Multi-shot ablation experiments of 2D TMDs

As discussed before, ultrafast laser patterning is attractive as a tool for the fabrication of 2DM-based devices due to its relative simplicity, cost-effectiveness, and property of being residue-free. Since the process of laser patterning exposes the material to trains of ultrafast pulses, any laser-induced defects added to the material by an incoming pulse can affect the light-matter interaction of the subsequent pulse, a phenomenon known as incubation. For this application, knowledge of multi-shot ablation is essential to select optimal laser parameters to deterministically remove the material. As the onset of ablation and damage are governed by similar physical principles, determining the breakdown threshold fluence $F_{th}(N)$ of 2D materials as a function of the number of pulses N admitting on the same spot can be good probe of laser-induced material degradation. This incubation phenomenon has been explored in the literature for bulk materials and some representative data is shown in Figure 3-4.

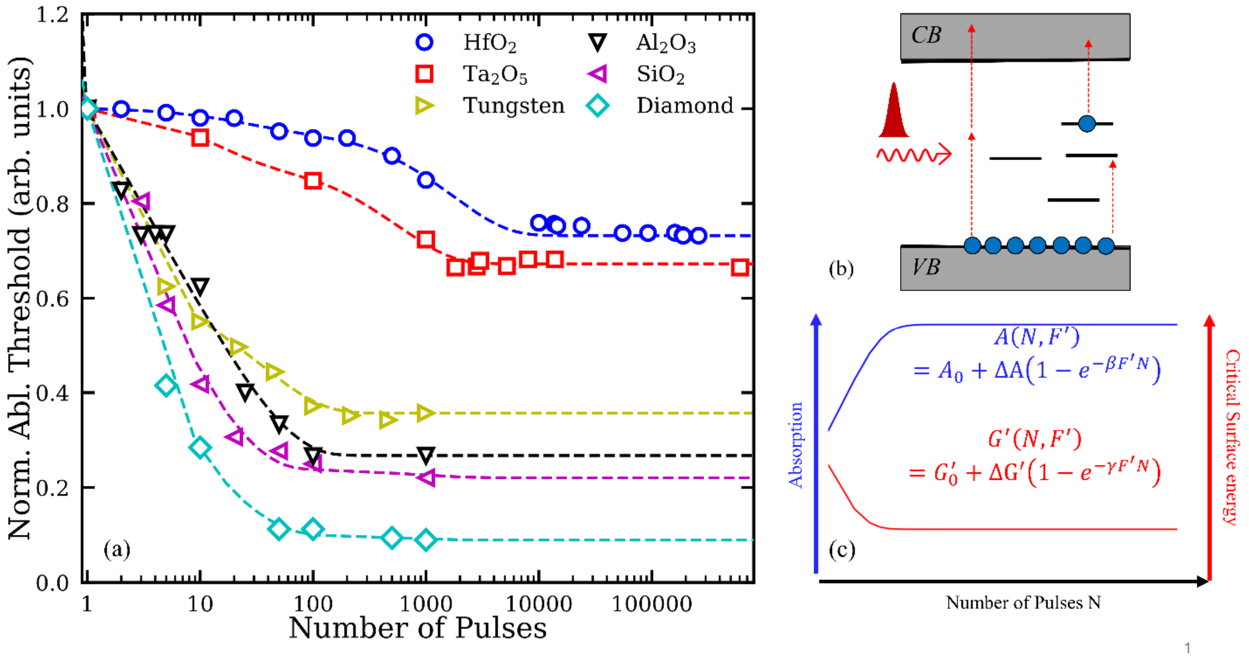

Figure 3-4: (a) Multi-shot ODB threshold data for multiple bulk materials from the literature. (b) Schematic showing laser-induced defects adding mid-gap states that lower the breakdown threshold. (c) Schematic showing the increase in absorption and well as the lowering in critical energy required for material breakdown according to the model described in the text.

Figure 3-4(a) shows data for HfO_2, Ta_2O_5, Al_2O_3 (80), SiO_2, Diamond and Tungsten from literature sources (80-85) and shows similar trends for most materials. Starting from the single-shot ablation threshold $F_{th}(1)$, the threshold fluence decreases monotonically with N until it approximately saturates at N_{sat}. For $N > N_{sat}$, the variation in F_{th} is small and that saturation fluence is defined as $F_{th}(\infty)$. For incident fluences below $F_{th}(\infty)$ no material damage is incurred for any number of pulses, at-least theoretically. The ratio $R \equiv \frac{F_{th}(\infty)}{F_{th}(1)}$ is defined as the measure of the degree of incubation: the larger the value of R, the smaller the effect of laser-induced defects (the lower the incubation) and the more optically robust the material.

It should be noted that such a study on the incubation effect has been carried out by Wetzel et al., in the case of graphene but their study was focused on laser patterning and did not include a discussion or gain much understanding of the phenomenon (63) .On the other hand, femtosecond multi-shot degradation of monolayer MoS_2 was reported by Paradisanos et al. (55) where they observed softening of the Raman A_{1g} and E_{2g}^{1} modes at two fluences [25% and 40% of $F_{th}(1)$], which was attributed to a decrease in the Mo–S bond density. Incubation in terms of $F_{th}(N)$ and their signatures beyond Raman scattering for monolayer TMDs has not been reported. In this section, the multi-shot ablation threshold for monolayer MoS_2 and WS_2 is studied and described based on a phenomenological model that was proposed by Sun et al (85). Transmission electron microscopy (TEM), second harmonic (SH), photoluminescence (PL), and Raman spectroscopies were carried out to reveal the morphological and optical property changes in MoS_2 in the sub-ablation damage regime to provide insight into defect formation.

To model the data, a generalized version of the phenomenological model introduced by Sun et al. (85) was used on the material data, which was formulated in terms of the change in absorption and critical bulk energy density. A schematic of the concept is shown in Figure 3-4 (b) and (c). Material absorption is the fractional pulse energy absorbed from the incoming pulse $A \equiv \Delta E / E$, and can change pulse-to-pulse due to the addition of mid-gap states due to the addition of defects, the formation of self-trapped excitons (STEs) (82), etc. according to the following equation written below.

$$A(N, F') = A_o + \Delta A(1 - e^{-\beta F' N}) \tag{3.8}$$

Where A_o is the initial absorption and $\Delta A = A_{\max} - A_0$ is the maximum change in the absorption, N the admitted number of pulses and β a fitting rate constant. The critical energy density is that amount of energy required to be deposited into the material for breakdown to occur and can be written as shown below.

$$G^{'}(N,F^{'}) = G_0^{'} + \Delta G^{'}(1 - e^{-\gamma F^{'} N}) \tag{3.9}$$

Where $G_0^{'}$ is the initial critical surface energy required for ablation and $\Delta G^{'} = G_{\min}^{'} - G_0^{'}$ is the maximum change in it. On an additional note, $F_{th}^{'} = \eta^2 F_{th,incident}$ is the internal fluence inside the 2D material. Using the internal fluence allows the determination of substrate independent coefficients when using this model in the case of 2DMs. The threshold fluence for N pulses would be reached when the energy deposited in the material by the N^{th} pulse equals the critical surface energy required for ablation that has been modified by the preceding $N-1$ pulses. This can be met by the condition.

$$A(N-1, F_{th}^{'}(N))F_{th}^{'}(N) = G^{'}(N-1, F_{th}^{'}(N)) \tag{3.10}$$

This and the previous two equations can be combined to formulate an equation for the breakdown threshold;

$$F_{th}^{'}(N) = \frac{[F_{th}^{'}(1) - F_{th}^{'}(\infty)(1 + \frac{\Delta A}{A_0})][1 - e^{-\gamma F_{th}^{'}(N)(N-1)}]}{1 + \frac{\Delta A}{A_0}[1 - e^{-\beta F_{th}^{'}(N)(N-1)}]} \tag{3.11}$$

Where $F_{th}^{'}(1) = \frac{G_0^{'}}{A_0}$ is the single shot breakdown threshold. This model is what was used to create the fit lines for the bulk materials in Figure 3-4(a). From Eq. , R can be expressed as a simple analytical function of the maximal fractional change in critical energy $\Delta G^{'} / G_0^{'}$ and absorption $\Delta A / A_0$ according to $R \equiv \frac{F_{th}(\infty)}{F_{th}(1)} = \frac{1+\Delta G^{'} / G_0^{'}}{1+\Delta A / A_0}$.

The described model was applied to fit the bulk data in Figure 3-4 as well as the 2DM data in Figure 3-5 shows the normalized F_{th} value of MoS2 and WS2 for selected N up to 1000 pulses. As a comparison, the incubation for graphene from (63) is also shown. For reference, the values of $F_{th}(1)$ and R for each of these materials are summarized in Table 1.

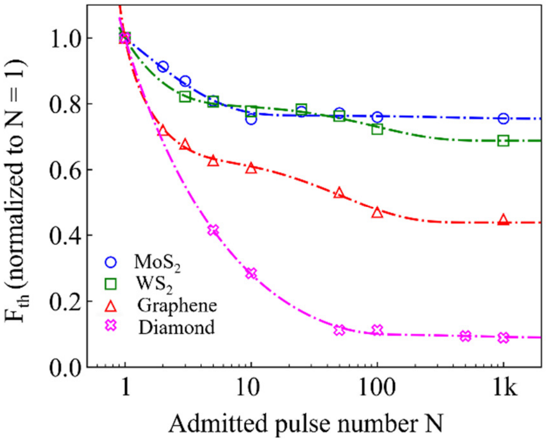

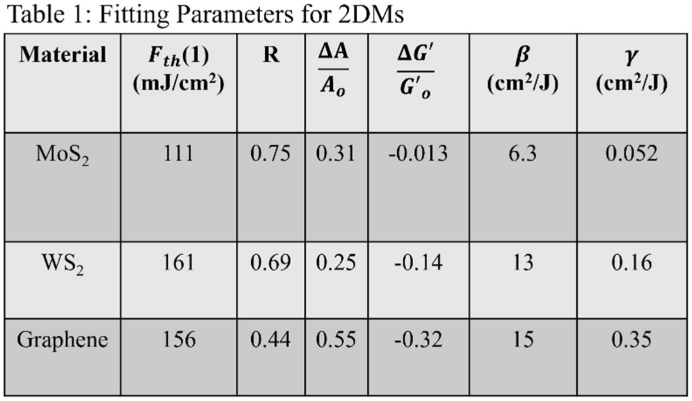
Table 1: Fitting Parameters for 2DMs

Material	$F_{th}(1)$ (mJ/cm^2)	R	$\frac{\Delta A}{A_o}$	$\frac{\Delta G'}{G'_o}$	β (cm^2/J)	γ (cm^2/J)
MoS$_2$	111	0.75	0.31	-0.013	6.3	0.052
WS$_2$	161	0.69	0.25	-0.14	13	0.16
Graphene	156	0.44	0.55	-0.32	15	0.35

Figure 3-5: (left) Experimental multi-shot ODB data for MoS2 on D263M glass and WS2 on Al2O3, overlaid with graphene and diamond data from the literature. (right) Table 1 shows the fitting parameters.

For MoS2, F_{th} decreases monotonically from $N = 1$ to 10 before saturating at $N_{sat} \sim 10$. For WS2 and graphene (63), F_{th} quickly reduces for the first three pulses and then experiences an inflection, before leveling off at 1000 pulses. The enhancement factors η^2_{D263M} = 0.63 and $\eta^2_{Al_2O_3}$ = 0.53 were used to calculate the internal fluence, as described in section 3.1.1. Table 1 shows the fitting parameters and resulting R values for the performed incubation experiments. The R values for MoS_2 and WS_2 were found to be larger than most bulk materials (80-85). Only HfO_2 (R ~ 0.73, N_{sat} ~ 10 000, and 50 fs) and Ta_2O_5 (R ~ 0.67, N_{sat} ~ 1000, and 150 fs) films were found to have comparable R values to MoS_2 and WS_2, respectively.18,19 Among all these materials, MoS_2 appears to have the fastest saturation, appearing to saturate at around 75% of the single shot threshold. Although MoS_2 and WS_2 have similar $\Delta A / A_0$ values, $\Delta G' / G'_0$ is negligible for MoS_2, yielding the largest R value and the smallest N_{sat} value with a single decay trend in its incubation. For WS_2 and graphene, the initial fast decay of F_{th} is due to a strong saturation of ΔA with the number of pulses (i.e., large β), followed by a slow decay due to a weak saturation of ΔG′ (i.e., small γ), leading to a larger N_{sat} value. The transition between these two decays manifests the inflection in Figure 3-5.

To gain information on the structural changes induced by a single laser exposure, an experiment was done where second harmonic generation (SHG) is used to probe the crystallinity of the 2D lattice of the film. The MoS_2 sample is exposed to a single intense pump pulse by firing the shutter, after which the ND filter is adjusted to reduce the laser power and the shutter is opened again to expose the sample to a train of weaker pulses to probe the resultant structural modification using static SHG. The result is shown in Figure 3-6 for various pump fluences below and above $F_{th}(1)$.

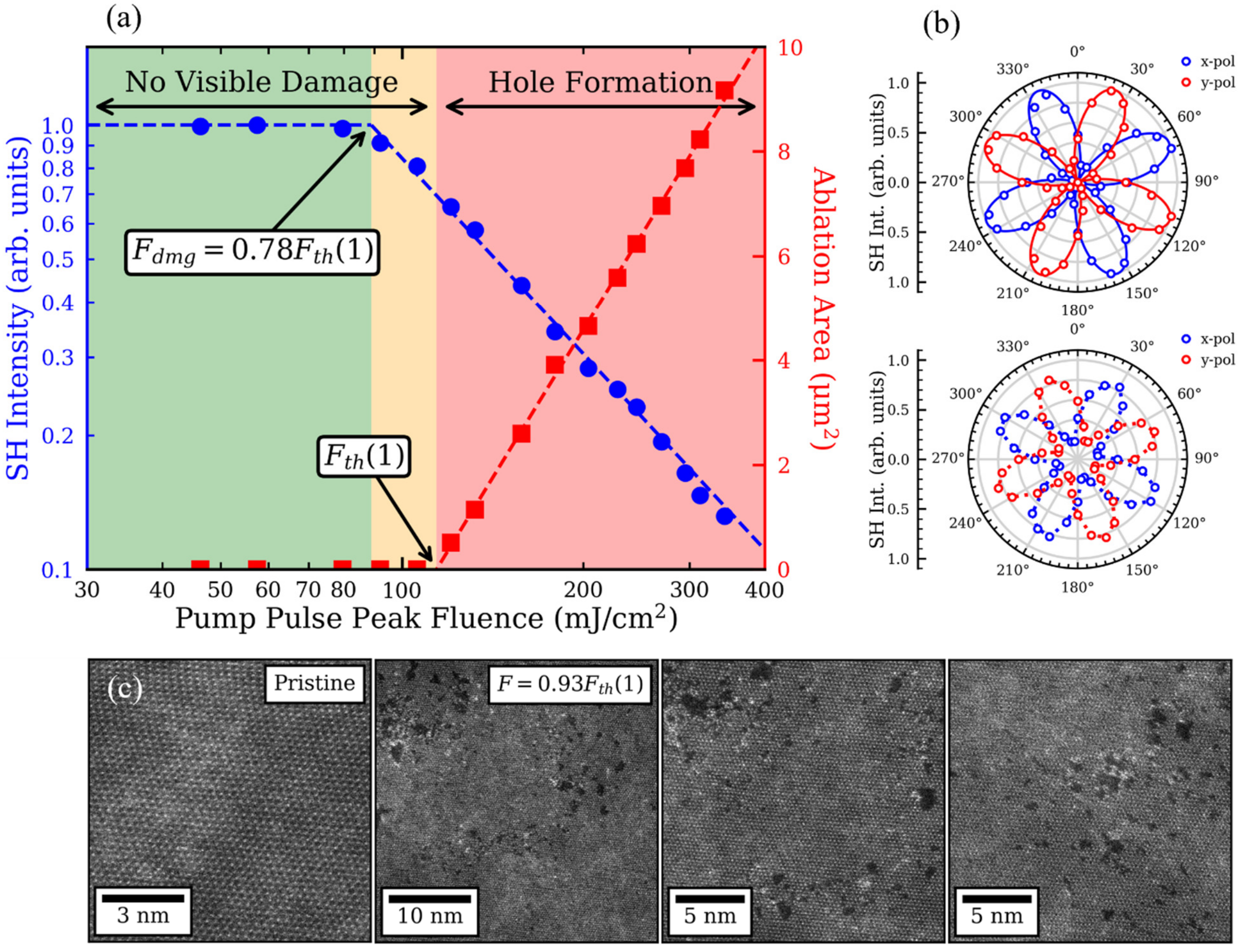

Figure 3-6 (a) Second harmonic generation (SHG) experiment results. (b) Polar plot of SHG with rotating incident polarization. (c) HR-TEM imaging of MoS$_2$ exposed to a single pulse at 0.93 F_{th} .

For fluences above $F_{th}(1)$ where holes are created deterministically, the SH signal decreases with increasing fluence, which is reasonable, given that the overlap of the probe beam with actual film is going to reducing and any signal detected will be due to the edge of the film still within the beam spot area. For pump fluences below ~0.78 $F_{th}(1)$, the SH intensity remained the same as that of pristine MoS$_2$, indicating that the material is intact with no adverse effects to long and short-range order in the crystal. Between these two points in fluence (yellow region in Figure 3-6(a)), even though OM shows no visible hole in the film, the SH signal is still below the pristine value, indicating that the film is permanently modified in some fashion. Accordingly, we define the sub-ablation damage threshold fluence $F_{dmg} = 0.78\,F_{th}(1)$ as the minimal fluence causing permanent damage to the film. At this limit, the damage most likely consists of localized vacancies and lattice disorder. What is crucial to notice is that this experiment agrees very well with the $0.75F_{th}(1)$ value of F_{sat}, showing that the conclusion one reaches by looking at the data from Figure 3-5; that being that no number of pulses with fluence below F_{sat} will modify the film holds a lot of merit. This finding clearly shows that such laser-induced effects represent the beginning stages of incubation for ablation. As long as the pulse fluence is below F_{dmg}, monolayer MoS_2 will not be ablated for any number of pulses $N > N_{sat}$. For fluences that are slightly higher than $F_{th}(N)$, each pulse will generate sub-ablation damage, accumulatively creating a deterministic hole at its zero-area limit by the N^{th} pulse. Another indication of this reduction in crystallinity is shown by Figure 3-6(b), which shows the SH polar profile for pristine MoS_2 by rotating the incident polarization while recording the SH signal at x- and y-polarizations at a constant probe beam power (~$0.3\,F_{th}(1)$ for each pulse). For a pristine film, the SHG should oscillate between its max value and zero as the polarization is rotated, as the phase-matching conditions are different for the different directions. The data follows the theoretical curve (solid line) in Figure 3-6(b, top), indicating excellent crystallinity of the pristine region probed on the film. Next the polar profile at the center of femtosecond -exposed region is shown in Figure 3-6(b, lower). As the damaged region is significantly smaller than the probe pulse spot size, the SH signal is dominated by the surrounding pristine MoS_2 where a four-fold symmetry is still clearly resolved. Compared to Figure 3-6(b,top), however, the depolarization (reduced contrast) is evident where the maximal SH intensity reduces by ~20% and the minimum never drops completely to zero. Clearly, the phase-matching is never completely detuned for any polarization angle, indicating the order in the lattice has reduced.

To directly image sub-F_{th} modifications, a MoS_2 film was transferred to a holey carbon film grid for high resolution transmission electron microscopy (HR-TEM). The left-most image in Figure 3-6(c) shows a HR-TEM image of pristine MoS_2 where the dark spots represent the sulfur atoms, and the bright spots are the molybdenum atoms. All other images in Figure 3-6(c) image MoS_2 exposed to a single pulse at F = 0.93 $F_{th}(1)$ where clusters of atoms ranging up to a few nanometers across are removed without destroying the overall integrity of the film. The figure reveals that such sub-ablation damage is stochastic in nature, where nano-voids appear sporadic with random sizes and shapes within the exposed area. This is in sharp contrast to the deterministic ablated holes seen when ablating above the threshold [Figure 3-1(a)]. The nano-voids in Figure 3-6 show a decrease of roughly 5% in atomic density, as determined using ImageJ analysis, which translates to a 10% reduction. in SH intensity. Figure 3-6(a), however, indicates a 20% reduction in SH intensity, implying the presence of other defects in addition to the nano-voids. This indicates there is lattice disorder in the film that is currently not possible to image with the TEM instrument used here. It is possible that under strong illumination the film melts and then resolidifies, creating small clusters, or ‘grains’ of crystal that have random orientations and the SH dipoles then cause emission in all directions. Alternatively, there exist defects smaller than the resolution of the TEM. To reveal more optical signatures of such defects, further optical spectroscopies were performed on pristine MoS_2, as well as on MoS_2 exposed to a single pulse at 0.83 $F_{th}(1)$.

Figure 3-7shows the PL and Raman spectra recorded at the center of the damaged spot exposed to a pulse with fluence 0.83 $F_{th}(1)$. As a reference, pristine film spectra are also shown in blue, taken in close spatial proximity to the femto-second exposed hole. The line profile of the PL peak intensity and center energy scanned across the damaged spot is presented in Figure 3-7(b), showing an intensity reduction of ~25% and a blue shift of 0.02 eV after exposure.

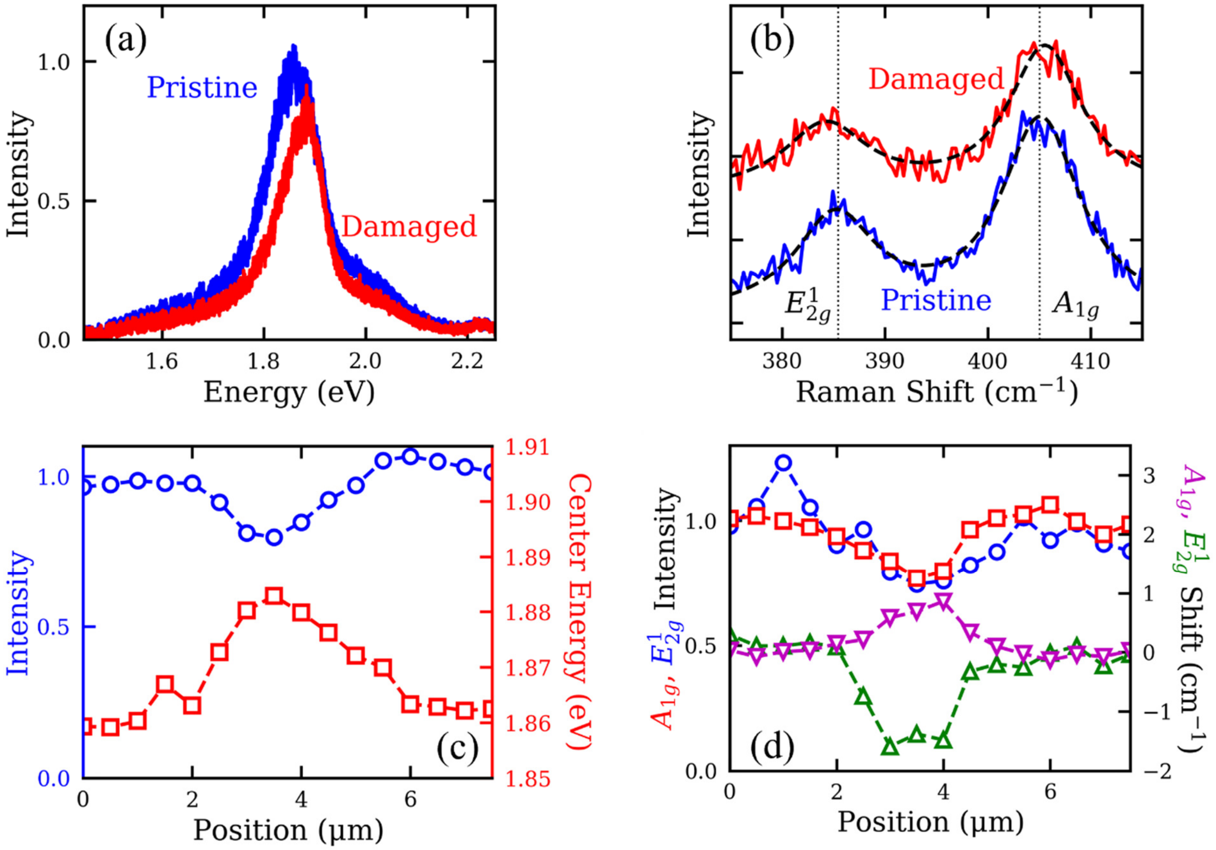

Figure 3-7: PL and Raman scan results across a single-pulse exposed area. (a) PL spectra of MoS_2 on pristine and exposed area. (b) Raman scan of a pristine and exposed area. (c) Extracted amplitude and center energy of PL line scan across exposed area. (d) same as (c) but for line scan with Raman spectra being taken.

Similar results were also recorded for the Raman line scan as shown in Figure 3-7 (c) and (d), where the intensity of both the E^1_{2g} and A_{1g} peaks are reduced by ~25% in the damage region. Additionally, the E_{2g}^{1} mode experiences a maximal red shift of 1.6 cm−1, while the A_{1g} peak shows a maximal blue shift of 0.9 cm^{-1}. For single pulse exposure at 0.83 $F_{th}(1)$, the reduction of the Mo–S bonds is estimated below 5% from Figure 3-6 (c), indicating that other defects play a significant role in the observed 20%–25% drop in SH, PL, and Raman intensities. The presence of vacancies and disorder breaks the lattice translational symmetry, which compromises the constructive and destructive interference among SH dipoles across the sample. This will reduce the maximal SH signal and increase the minimal SH signal in the polar plot, consistent with the observed depolarization effect discussed earlier. In addition, dangling bonds associated with these vacancies are known to introduce mid-gap states. Several types of vacancies associated with S and Mo atoms are shown to generate mid-gap states with energies ranging from 0.02 to 1.72 eV within the bandgap, which can provide non-radiative decay pathways (86-89). These states have been invoked to strongly quench the PL intensity and cause a blue shift similar to that observed here (90-94). The blue shift in the PL peak can also be attributed to the adsorption of oxygen on the MoS_2 monolayer given the ambient conditions of the experiment (93). Moreover, the occupation of these mid-gap states by the preceding pulses could increase the light absorption (ΔA/A0) of successive laser pulses during incubation, leading to a reduction in threshold fluence (88). Additionally, the lateral strain introduced locally by these vacancies and lattice disorder can cause the Raman intensities to decrease (95, 96). The blue shift in the A_{1g} peak and the red shift in the E_{2g}^{1} peak could be explained by a combination of p-doping from the presence of Mo–O bonds (97, 98) and strain introduced by these defects (93, 96). To understand quantitatively the difference of incubation between these two materials, a microscopic model involving multiple kinetic rate equations is needed (99). While such a model better describes the physics of incubation, its implementation is challenging since many properties associated with these defects in 2D materials, such as their energy levels and lifetimes, are not known in the literature or are speculative at best.

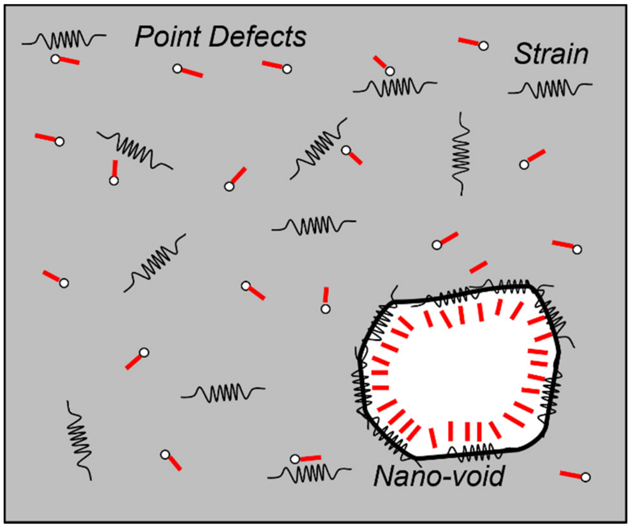

Figure 3-8: Illustration of the different types of defects produced by the ultrafast pulse exposures.

Overall, the different probes utilized reveal information about the different types of defects added to the material under repetitive femtosecond laser pulse exposure. SHG reveals a reduction of crystal symmetry, TEM sheds light on nano-voids themselves forming within the femtosecond exposed area, PL reveals the nature of the defects as being dangling bonds on the edges of the nanovoids in the material and Raman reveals information about the strains applied in the material because of the reduction in lattice order.

3.3 ODB of monolayer hexagonal boron nitride (hBN)

This multiple-pulse ODB work carried out for these 2DMs displays their superior optical robustness under strong-field femtosecond light in comparison to most bulk materials. Even the single pulse ODB work shows somewhat different physics between the metals and semiconductors. Graphene's E_g is 0 eV due to it being a metal and its incubation behavior is markedly worse than that of MoS_2 and WS_2. Additionally, the breakdown threshold of graphene (~50 mJ/cm^2) is higher than that for the TMD semiconductor with the smallest bandgap, which is $MoSe_2$. This could be due to the remarkably high tensile and breaking strength possessed by graphene, where the Young's modulus is ~ 1 TPa, as compared to ~100 GPa for $MoSe_2$ (100) and the breaking strength is . Alternatively, it could be due to different carrier generation physics occurring in different categories of material. The breakdown threshold for different categories of material is shown in Figure 3-9 below. Note that the separation between different categories of material (metal or semiconductor of insulator) is somewhat arbitrary and is simply for the purposes of illustration.

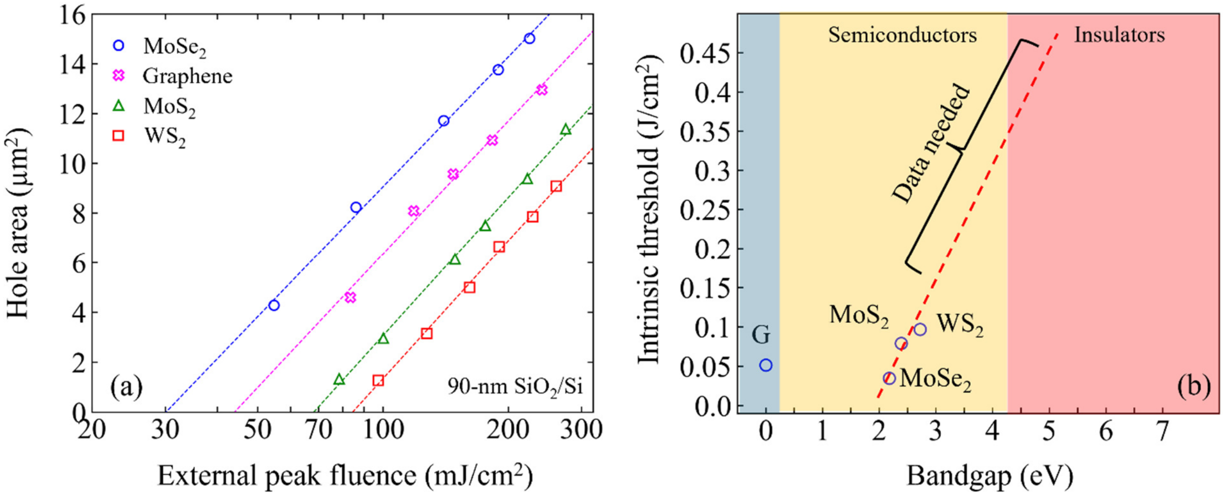

Figure 3-9: (a) ODB thresholds of different 2DMs on 90 nm SiO_2/Si substrates. (b) F_{th} vs E_g for the thresholds found in (a).

The source used this this work produces 800 nm (1.55 eV), 160 fs pulses where the center wavelength is above the material bandgap for graphene, thus it is possible a lot of linear absorption occurs when the light is incident on the material. The semiconductors $MoSe_2$, MoS_2 and WS_2 all possess bandgaps larger than the exciting wavelength and thus might exhibit different physics, possibly nonlinear mechanisms, for carrier generation. Figure 3-9 shows that the semiconductors do exhibit a scaling of F_{th} with the material bandgap that is intriguingly linear and is different from the threshold seen for graphene, although more data points are required to confirm such a hypothesis. Further investigations into materials with higher bandgaps is desirable. This opens another realm of investigation; wide-bandgap 2D insulators are interesting from a practical perspective since they can potentially be used alongside the semiconducting 2DMs in nano-sheet transistors. ODB investigations on such an insulator would hold both engineering applicability as well as more fundamental science interest. For these reasons, hexagonal boron nitride (hBN) was selected to investigate the ODB of a wide bandgap 2D insulator.

Here, we report the first systematic study of optical breakdown of hBN monolayers induced by a single femtosecond laser pulse. We demonstrate that hBN has the highest breakdown threshold among all 2D materials, and femtosecond ablation removes hBN without leaving traces behind or causing lateral damage. The ablation features exhibit excellent fidelity which we attribute to its heterogeneous nature with 3-fold symmetry. This work clearly positions femtosecond laser ablation as a promising tool for resist-free patterning of hBN.

3.3.1 Imaging modalities, Breakdown threshold and Reproducibility

Since hBN exhibits such a large material bandgap (7.7 ± 0.5 eV, based on the literature reported values at the K point ranging between a minimum of 7.2 and maximum of 8.2 eV (40, 101)) it is important to utilize a substrate that is optically robust that is intact when the hBN film itself experiences ODB. Two obvious candidates are Al_2O_3 and fused SiO_2, possessing bandgaps of ~ 9.35 ± 0.55 eV (40, 101) and ~ 9 eV (102) respectively. An Al_2O_3 substrate was considered initially due to its large E_g but was subsequently found to interfere with any Raman measurements (this will be discussed in section 4.2.2) and thus not used. Nevertheless, it was discovered that fused SiO_2 fused SiO_2 substrates maintained their integrity at the breakdown threshold of hBN and were thus utilized for further experiments. In both the case of Al_2O_3 and fused SiO_2 being used as substrates, the optical contrast presented under OM is extremely poor. This considerably complicates the process of experimentation on hBN since any ablated features are invisible. Essentially, one is ‘shooting in the dark.’ Thus, multiple imaging modalities were investigated and are shown in Figure 3-10.

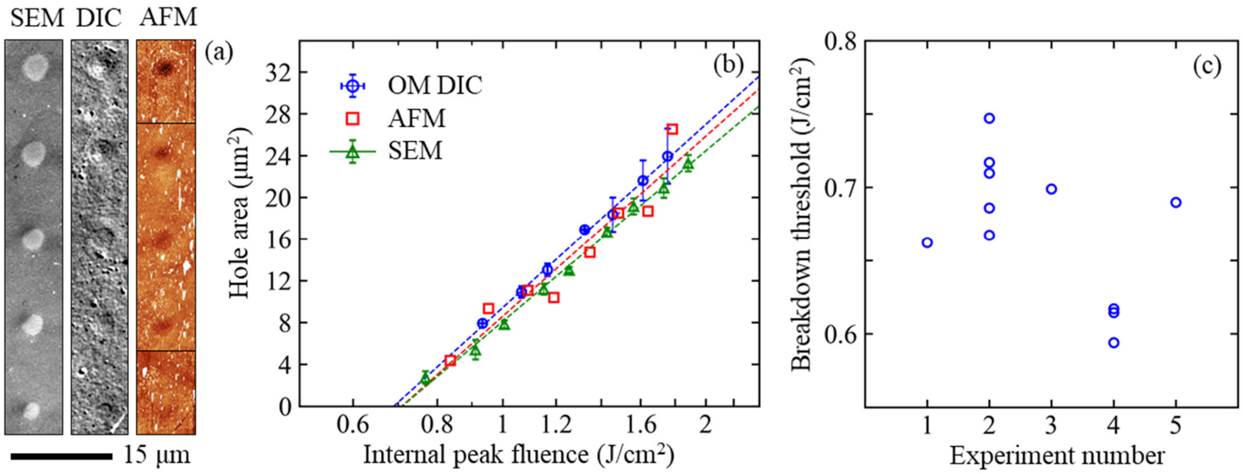

Figure 3-10: (a) SEM, DIC and AFM images of the same ablated features in a hBN monolayer on fused silica, produced with a laser beam radius of ~ 4 µm and with decreasing pulse energy from top to bottom. The scale bars are 15 µm. (b) A linear-log plot of ablated hole area vs. internal peak fluence for three imaging modalities. (c) Reproducibility of breakdown thresholds on the same sample over different days and geographic locations across the sample.

Figure 3-10(a) shows SEM, DIC and AFM images of an array of holes in a hBN monolayer on fused silica ablated with incident pulse energies of 620, 560, 508, 448 and 409 nJ (from top to bottom). The scaling of the hole size with the pulse energy is evident and consistent across different imaging modalities. These pulse energies were converted to the peak internal fluences (in J/cm^2)

following $F = 200 \cdot \eta^2 E / \pi\omega_o^2$, where $\eta = 0.66$ is the field enhancement factor due to the etalon effect (39), E is the incident pulse energy (in nJ), and ω_o is the focused Gaussian beam waist (in μm). Figure 3-10(b) displays the hole area A as a function of the peak internal fluence F for three imaging modalities. The data were fitted to Liu's equation $A = (\pi/2)\omega_o^2 \ln(F/F_{th})$ to extract the breakdown threshold fluences F_{th} (72), which are 0.69, 0.71, 0.71 J/cm^2 for DIC, SEM, AFM modalities, respectively, yielding an average value of 0.70 ± 0.01 J/cm^2. This number is the largest among all 2D materials, which is 8× (10×) higher than that of WS_2 (MoS_2) monolayers (103). Substrate damage was observed for $F \geq 1.5\, F_{th}$ (or 1.1 J/cm^2), evident as a central darker spot in AFM and a brighter spot in DIC images.

To assess the reproducibility of the breakdown thresholds, the above procedure was repeated across the same sample on different days. Figure 3-10(c) shows the statistics of the retrieved F_{th} based on DIC. Experiments #2 and #4 have multiple runs on the same day on remotely separated locations in the sample, which has a spread of 4% and 2%, respectively. Over different days, the spread can be as large as 14% (or ±7%). This number is on par with the 10% reproducibility reported for nanosecond-picosecond laser ablation (104) and is lower than the 15% reproducibility reported in Mero's report for the fluence thresholds for thin amorphous films (47). The reproducibility of F_{th} is influenced by many factors. The small spread of F_{th} in experiments #2 and 4 indicates the sample is quite uniform across the substrate in terms of film quality (e.g., defect density, strain field, etc.), PMMA residue, and substrate imperfection (e.g., roughness, cracks, grooves, pores, etc.). These set the lower limit of reproducibility. The remaining spread is most likely due to the irreproducibility of laboratory conditions such as laser beam quality (e.g., beam size, pulse width, chirp, etc.) and the humidity and temperature of the room.

In the earlier stages of this work a fourth imaging modality was explored that can potentially be used in the imaging of hBN; 2D photoluminescence (PL) imaging. This was performed on the Raman setup described in section 2.3.3 where the sample was scanned laterally in two-dimensions at the laser focus of the objective. Back-emitted PL from the 532-nm excited hBN was coupled into the multimode fiber (with an additional 560-nm LPF) and detected via PMT. Thus, each pixel in a 2D image corresponds to an intensity and the images are shown in Figure 3-11.

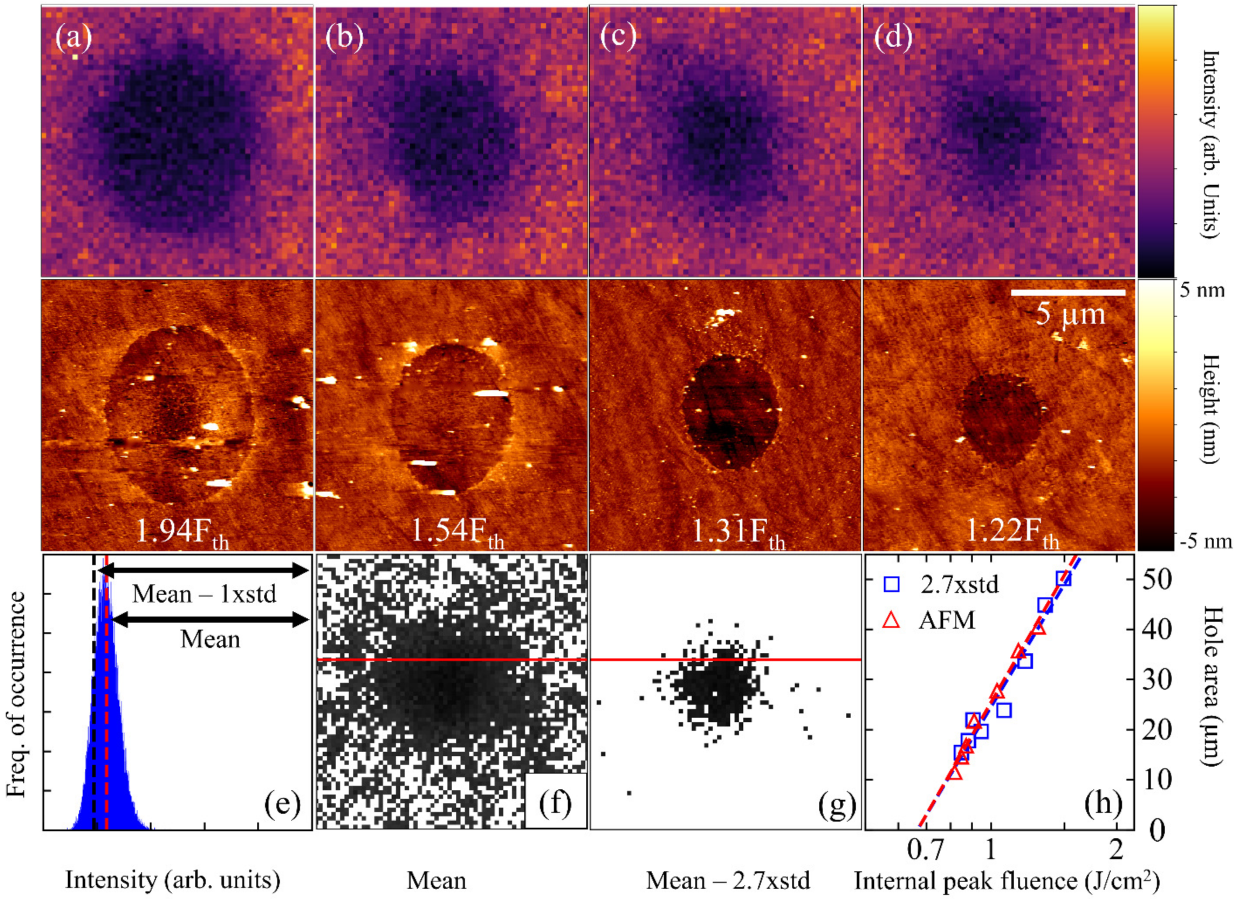

Figure 3-11: (a)-(d) (above) 2D PL scanning images of multiple above- F_{th} holes made in hBN monolayer. (below) corresponding AFM images of the holes shown in (a) to (b). (e) Histogram computed of a 2D PL image of a pristine hBN film (no hole of fs exposure). (f) 2D PL grayscale image of a hole. All pixels at the mean and above (shown in (e)) are painted white. (g) same image as in (f) but with pixels at mean – 2.7xstd painted white. Note: the red line in the image is an

processing artifact and can be ignored. (g) Liu plot of the 2D PL images computed using the method described in (e)-(g) for all holes and compared to a Liu plot from AFM images.

The resulting 2D PL images show the holes to have blurred boundaries in comparison with the AFM images due to the PL images being a convolution of the beam spot size with the actual hole. This makes measuring the hole area difficult. It is possible to obtain a calibration factor (that is somewhat of a deconvolution factor) that can allow measurement of true hole sizes and features via the measurement method outlined in Figure 3-11. An intensity histogram (Figure 3-11(e)) of the pixels from a 2D image of pristine hBN film provides a reference intensity value representing the pristine film. Since the ablation hole corresponds to darker pixel (lower intensity values in the PL images), all pixels with values at the mean minus 2.7× the standard deviation of the histogram are thresholded and ‘painted’ such that an outline of the holes appears for measurement of the hole size. This allows measurement of the hole area. This method of measurement gives the same breakdown threshold as that measured via AFM. While initially interesting, this method ultimately proved unsuitable for practical use, since great care had to be taken while selecting the incident CW laser power such that the optically bright defects did not bleach, get modified via thermal effects and ‘go dark.’ Additionally, the PL signal was not reproducible. When additional hBN on quartz samples were synthesized with the additional step of rapid thermal annealing (RTA) being performed to attempt to clean any PMMA residue that might have been left behind on the sample after transferring to the target substrate, it was found that the PL signal was no longer exhibited. This indicates either that the optical defects in hBN were deactivated or ‘healed,’ or more likely the emission was from PMMA. Thus, this modality was no longer pursued. The reader should note that all work on hBN reported in this dissertation thus relates to the latest hBN on fused silica samples that underwent RTA and presented no PL emissions.

3.3.2 Evidence of clean removal

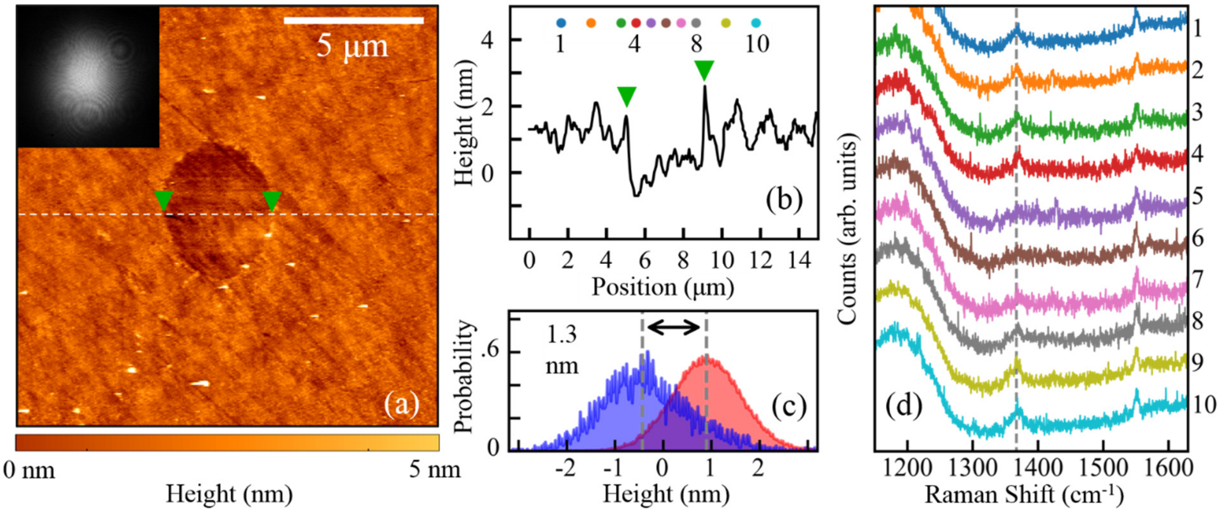

Figure 3-12: (a) Ablated hole in hBN on fused silica with an internal peak fluence of 0.86 J/cm^2. The focused laser beam radii (1/e^2-intensity) is 6.32 μm. The white particles of varying shapes and sizes are PMMA residue from the transfer process. The inset shows the laser beam image captured via CCD. (b) Cross-sectional line profile of a 1.2 nm thick stripe of (a) represented by the dotted line. Green arrows indicate the edge of the hole. (c) Histogram of height data of (a) inside the hole (blue data) and region outside the hole (red data). (d) Raman signals collected across (a). The signals correspond to colored markers in (b).

Figure 3-12(a) shows an ablated hole in hBN obtained with an internal peak fluence of 0.86 J/cm^2 ($F = 1.27\ F_{th}$), whose cross-sectional height profile (averaged over a horizontal strip of 1.2 nm wide) along the dashed line is displayed in Figure 3-12(b) with green arrows indicating the edges of the hole. Figure 3-12(c) shows histograms of AFM height data within the hole (blue trace) and of the pristine film (red trace). The blue trace appears noisier than the red because of fewer pixels available in the hole for statistical averaging. The difference in the peak positions indicates a film height of ~ 1.3 nm, which is consistent with the literature value of 0.3 – 2.8 nm for hBN monolayers (22, 44). The cause of such a large variation in monolayer thickness for the film can be multi-fold. A further discussion on the causes of such variation is provided in the SPM data processing section in Chapter 2.

The width of the histogram for the hole is 1.95 nm, which is slightly larger than 1.76 nm of the pristine film, suggesting that the hBN film acts like a carpet to hide the surface roughness of the underlying bare substrate. The surface roughness inside the hole (Figure 3-12(c)) is the same as that of the bare substrate (Figure 3-13) , indicating the monolayer is removed without damaging the substrate at this fluence.

Figure 3-13 compares histograms of AFM height data within the ablated hole of Figure 3-12(a) on fused silica and that of the bare substrate. The widths of these two histograms are similar, indicating the monolayer is removed without damaging the substrate.

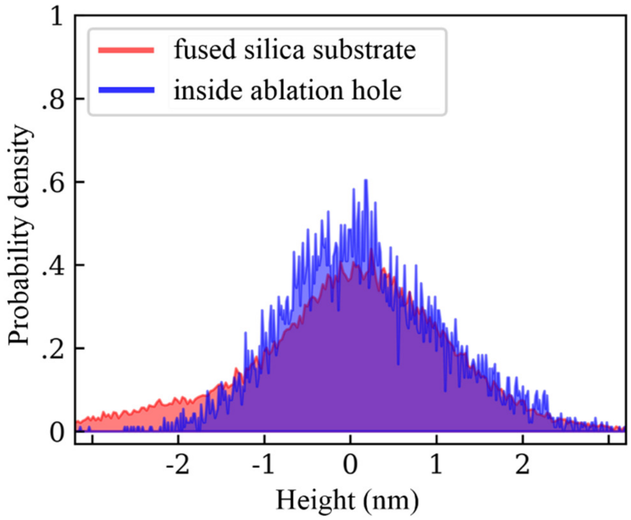

Figure 3-13: Histograms of AFM height data of the ablation hole (blue trace) and of the bare fused silica substrate (red trace). The vertical axis is the probability density function (PDF).

Figure 3-12 (d) displays Raman spectra taken across the hole in Figure 3-12(a), with each spectrum displaced vertically for clarity. The color-coded circles in Figure 3-12(b) mark the positions where the Raman signals were collected. The common features of a broad peak at ~ 1185 cm^{-1} and a smaller one at 1553 cm^{-1} are attributed to the fused silica substrate (see section 4.2.2). The E_{2g}^{1} in-plane optical phonon Raman peak at 1367 cm^{-1} is weak yet clearly resolved and consistent with literature values of 1366 – 1370 cm^{-1} for hBN monolayers (22, 105). Typically the out-of-plane Raman mode for hBN at 52.5 cm^{-1} (106) can be tell-tale sign of the film being multi-layer but the fused SiO_2 spectrum has emission at that shift which precludes that measurement.

The Raman signature of hBN has variation in the literature. One study reports 1370 cm^{-1} yet admits the repeatability of their instrument is limited and that they have measured as low as 1340 cm^{-1} (44). Other reports have values ranging from 1367 cm^{-1} (105), 1369 cm^{-1} (107) and 1372 cm^{-1}, variation that has mostly been attributed to strain. An illuminating report found the Raman peak of single layer hBN to shift by ~30 cm^{-1} (108) based on the isotope used in the hBN synthesis. In the growth of the hBN samples used in this work the isotope concentration was not controlled and could be one possible cause for the shift of the peak that was observed in comparison to that seen in the literature.

This peak vanishes within the hole (traces #5-7), indicating a clean removal of the film by the ablation process. The Raman spectra near the border of the hole (traces # 3,4, 8, 9) show no new peaks or frequency shifts of existing peaks within our detection limit. The absence of new peaks is in sharp contrast to a previous report (44), in which a new Raman peak at 1295 cm^{-1} corresponding to cubic boron nitride (cBN) nano-crystals was observed when the ablation was incurred by 80-MHz nano-joule femtosecond pulses. Frequency shifts, if they exist, would indicate the presence of strains originating from vacancies and lattice disorder introduced by the ablation, which was observed in MoS_2 monolayers (103). The lack of such changes reveals that hBN monolayers remain pristine around the edge of the ablated hole, even at an intensity close to the breakdown threshold.

3.3.3 Patterning fidelity

It is important to examine how well the femtosecond light source can cut the film such that the shape of the ablated hole matches the shape of the laser beam itself in a deterministic fashion. Often thermal or shockwave effects can cause warping of machined features around the edge of the ablated hole, such as was shown for the case of 100 nm metal films irradiated by 500 fs pulses (109). Stochastic features in ablated regions is also something seen in the case of graphene (110), which limits the minimum feature sizes achievable with the film. Here the match between the laser beam shape and the shape of the ablated hole is termed the patterened 'fidelity.' Figure 3-14 shows a schematic for quantitatively determining the fidelity in the specific case of hBN.

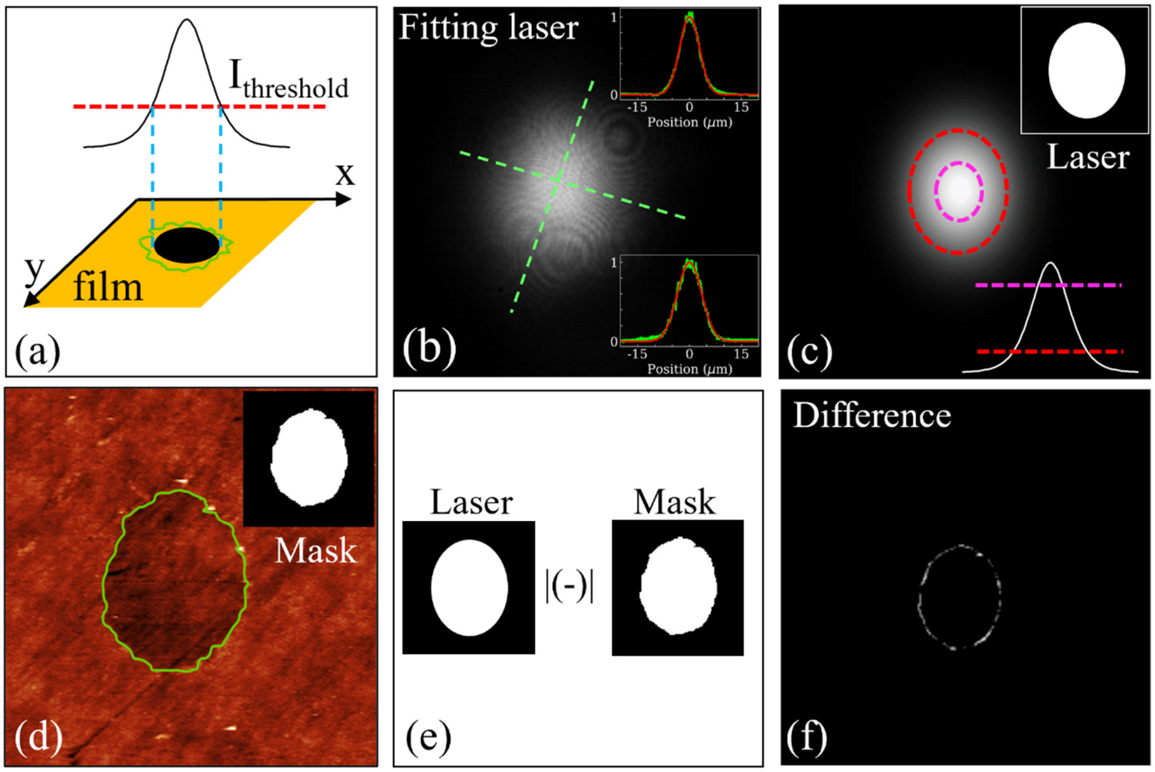

Figure 3-14: Schematic of the patterning fidelity (a) A laser pulse is incident on the material and ablates a hole in the film. Roughness around the edge of the hole is caused by various effects. (b) Laser beam profile measured via CCD and fitted around the major and minor axes. (c) Generated beam profile from the fitting in part (b). The colored dashed lines show different sizes of hole that can be generated by particular intensity levels spatially in the beam (inset) simulated hole shape corresponding to an intensity level. (d) AFM measurement of an actual hole ablated in hBN monolayer. (inset) masked image generated from the highlighted edge of the hole in the AFM image. (e) The simulated hole from the laser image and the mask image are subtracted and the absolute value is computed. (f) The difference image from the subtraction in (e).

Figure 3-14(a) shows a schematic of the laser beam incident on the film. Ideally, the point at which the intensity exceeds the material ablation threshold is where the boundary of the hole should begin. Thermal effects, stresses on the edge of the film boundary, etc. can cause damage beyond the shape of the pure laser beam. Thus, a comparison should be made between a 'simulated' hole made from the ideal shape of the laser beam at a particular intensity and the actual hole cut into the material. To compute this ideal hole shape the laser beam was imaged using the beam microscope described in section 2.1.3. The measured beam was sampled along its semi-major and minor axes and fitted using gaussian functions as shown in Figure 3-14(b), from which an elliptical gaussian shaped laser beam was generated (Figure 3-14 (c)). Any given intensity level corresponds to a particular size of hole, as shown by the colored contours in Figure 3-14(c), and an image was generated of the predicted hole the laser would ideally create. From the OM (in the case of graphene and MoS_2) or AFM (in the case of hBN) images of the actual ablated hole a masked image is created manually using gwyddion (inset in Figure 3-14(d). Both the ideal hole image and the masked image are subtracted from each other (Figure 3-14(e)). The difference image (Figure 3-14(f)) is then normalized to the pixels of the hole in the masked image, giving the percentage area mismatch. This quantity measures the degree to which the shape of the ablation feature differs from the ideal hole shape that would be created by the laser beam. The best fit and intensity level are chosen to minimize the percentage area difference.

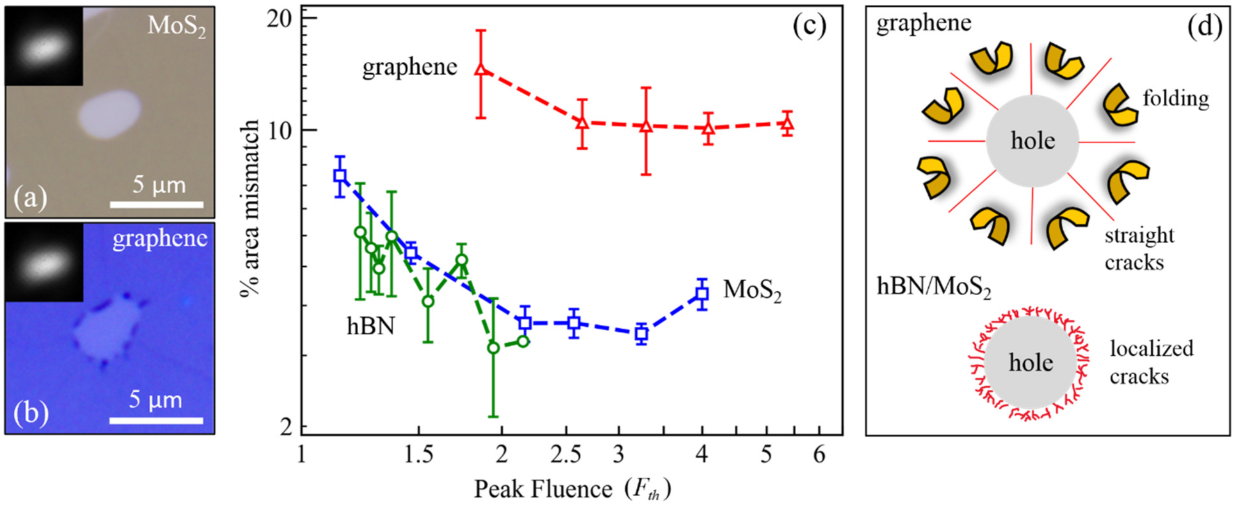

Figure 3-15: (a) An ablated hole in MoS_2 monolayer flakes displaying smooth edges, and (b) an ablated hole in graphene monolayer film displaying folding around the edges. Both results were

performed on 90 nm SiO_2-Si substrates(39) with a laser beam waist of 2.2 μm. The insets show the laser beam images captured via CCD. (c) Calculated percentage area mismatch vs internal peak fluence (in units of F_{th}) data for hBN, MoS_2, and graphene. (d) Illustration (not to scale) of different crack propagation in hBN (MoS_2) and graphene.

The same procedure was followed in the case of MoS_2. An ablation hole and the corresponding laser beam profile is shown in Figure 3-15(a). MoS_2's ablation and fidelity is in stark contrast to that exhibited by graphene, which exhibits petal-like folds outwards away from the ablated hole (see Figure 3-15 ((b) or Ref. (111) for a demonstration with a stronger contrast). Graphene folding was found universally on supporting substrates, possibly due to the rapid substrate expansion during the laser heating (111), which makes high-fidelity patterning of graphene difficult using femtosecond ablation (112). The percentage area mismatch is plotted as a function of the internal peak fluence (in units of F_{th}) for graphene, MoS_2, and hBN (Figure 3-15 (c)). As shown, the percentage area mismatch is comparable for hBN and MoS_2 monolayers but is 4× smaller than that of graphene. We attribute this sharp contrast in fidelity to their different fracture toughness, which is the ability of a material to resist catastrophic fracture (113, 114). Take graphene and hBN as examples. The removal of atoms in the film via laser ablation introduces compressive stress on the edge of the film (115) and cracks initiate from stress concentration sites. For graphene, the cleavage of the bonds results in two identical zigzag edges. Because of this symmetric edge stress, the crack tip propagates along a straight line over a longer distance (*i.e.*, low fracture toughness) (116). Upon the fast substrate expansion induced by the laser heating, the remaining graphene between two adjacent cracks fold (111), leading to the higher area mismatch and lower fidelity (Figure 3-15 (d)). For hBN, the situation is quite different (114). The cleavage of h-BN bonds results in two different types of zigzag edge: a B-terminated edge (B-edge) and an N-terminated edge (N-edge), of which the B-edge has twice the edge stress than that of the N-edge (114). Because of this asymmetric edge stress, the crack tip bifurcates first and then deflects from its original propagation direction, and consequently the B-edge and N-edge swap their positions relative to the crack tip owing to their three-fold symmetry (114). Cracks propagate via repeated deflection and sometimes branch, dissipating substantial energy to form a high density of localized damage close to the edge of the hole (*i.e.*, high fracture toughness). Experiments have shown hBN has a fracture toughness up to 10× higher than graphene (114, 116). The same fracture physics can be applied to other heterogeneous 2D crystals with 3 fold symmetry such as MoS_2 (114), which is supported by our data in Figure 3-15(c). Our result indicates femtosecond laser patterning of hBN and MoS_2 has high fidelity and can generate deterministic features. These observations were next utilized to demonstrate sub-micron patterning in the hBN film.

3.3.4 High-resolution patterning

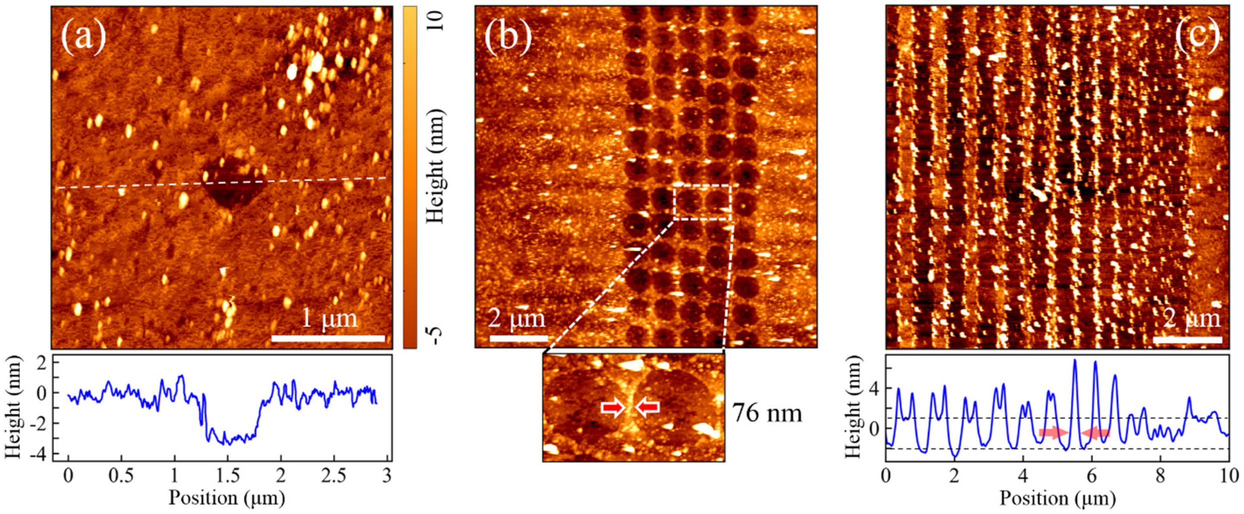

Figure 3-16: AFM images of patterned hBN using femtosecond laser: (a) an isolated hole, (b) an array of holes, and (c) an array of line cuts with decreasing hatching distance. The bottoms of (a) and (c) are a cross-sectional AFM height profile and column-averaged cross-sectional AFM height profile, respectively, and the bottom of (b) is the zoomed-in of the dashed box. See text for details.

By using a 0.9-NA objective and a fluence close to the breakdown threshold ($F = 1.1F_{th}$), Figure 5(a) shows an AFM image of a hole with a diameter of ~ 500 nm in hBN. This sets the resolution of the material removal (*i.e.*, the minimum hole diameter or the line cut width). Figure 3-16(b) shows an array of holes ablated with a fluence of $1.75F_{th}$ and a 0.55-NA objective. The periodicity is 1 μm and the average diameter of the holes is 830 nm. The zoomed-in AFM image (bottom) shows left-over film width of ~ 76 nm between two adjacent holes, an impressive resolution that can be achieved. Figure 3-16(c) shows an AFM image of an array of line cuts obtained with a fluence of ~ $1.5F_{th}$ and a 100 μm/s scanning speed, rendering a line cut width of 330 nm. The bottom plot displays a column-averaged cross-sectional height profile obtained by stacking all columns and then dividing it by the number of columns to remove low-frequency spatial noise. The hatching distance starts at 1 μm and decreases by 50 nm per line, leading to a gradual decrease of the strip width. The PMMA residue is more pronounced in this region of the sample, especially along the edges of the stripes, which suggests these PMMA particles may have aggregated upon laser irradiation. These aggregates lead to the fork-like features in the height profile, which evolve into peaks for very small hatching distances of the laser beam. The stripes display width variation and edge roughness due to the finite positioning stability of the translation stage in the depth and lateral directions, which was hampered by the cross coupling from the moving vertical axis. The horizontal dashed lines delineate the top and bottom of the film, from which the narrower stripe width is determined to be ~ 240 nm. When the hatching distance is too small, hBN stripes become partially removed due to the positioning instability. Holes and line cuts demonstrated in Figure 3-16 form the basic building blocks for more sophisticated structures and have plenty of room for improvement: Ablation resolution can be improved by using a shorter wavelength, narrower strip width can be obtained by a more stable translational stage or employing beam shaping techniques (38), and higher throughout can be obtained using a galvo scanner (117). Moreover, a more effective recipe for cleaning PMMA residue (37) or a residue-free transferring agent such as PDMS (118) can be adopted to improve surface cleanness.

4 THE ROLE OF AVALANCHE IONIZATION IN hBN ABLATION

As seen in the previous chapter, hBN exhibits good conformity to the laser beam profile and a high degree of reproducibility under femtosecond ablation. In this next chapter the ablation threshold of hBN is examined in relation to the ablation threshold of other 2D and bulk materials. The role of different photoionization processes such as multiphoton and avalanche ionization is examined and it is concluded that AI is the dominant mechanism involved in carrier generation, as well as the generation being more efficient in hBN.

4.1 Avalanche Ionization

Several reports have investigated the nature of ultrafast ablation and the nature of the threshold energy required for material damage can reveal information about the specific process that contributed to generating the carriers required for the ablation. Golin et al. measured the transmission of a linearly polarized 1900-nm (0.65 eV, GaAs has E_g = 1.43 eV), 75 fs source while rotating a GaAs crystal at the laser focus and found significant variations. According to Keldysh photoionization theory the effective mass of a material determines the multi-photoionization (MPI) rate. Small changes in the effective mass in different directions can lead to large changes in the MPI rate, so as the crystal orientation changes, the changing absorption due to changing MPI rate would lead to a changing transmission, which is what was observed (119). A similar experiment was performed by Li et al. with 800 nm, 35 fs light incident on GaAs (E_g = 1.43 eV), ZnSe (E_g = 2.8 eV), MgO (E_g = 5.37 eV) and LiF (E_g = 13.6 eV) crystals (120). The F_{th} was found to have a maximum variation of ~1-2.4 F_{th} (in the case of GaAs) as the polarization was rotated using a HWP, indicating that MPI is the dominant mechanism in the ablation process for these materials. A similar conclusion was reached by Mero et al., where dielectric breakdown for TiO_2, Ta_2O_5, HfO_2, Al_2O_3, and SiO_2 with 800-nm pulses between 25 fs to 1.3 ps materials was examined (47). When fitting using a phenomenological model that takes MPI and AI into account via a single rate equation, a conclusion favoring MPI as the carrier mechanism is drawn. However, this does not apply to all bulk materials and there are caveats to Mero's experiments; their materials are thin films that are amorphous and ideally, data for crystalline bulk materials should be examined to get intrinsic properties and mechanisms of the materials. Studies like Mero's have been done by others; Scahffer et al. report a similar linear relationship for SF11, Corning 0211 glass, fused silica, and CaF_2 with both 800- and 400-nm femtosecond pulses but unfortunately have no discussion on the relevant mechanism (121). Joglekar et al. performed similar experiments on Si, fused SiO_2, quartz and Al_2O_3 with 1053-nm, 800-fs pulses, with the addition of threshold energy being compared for different light polarizations (40). Since the quiver energy in AI needs to match the bandgap for new carriers to be promoted to the CB via impact, the threshold fluence required for ablation will increase linearly with E_g, they argue that AI is the dominant mechanism. The data from different sources in the literature is presented in Figure 4-1.

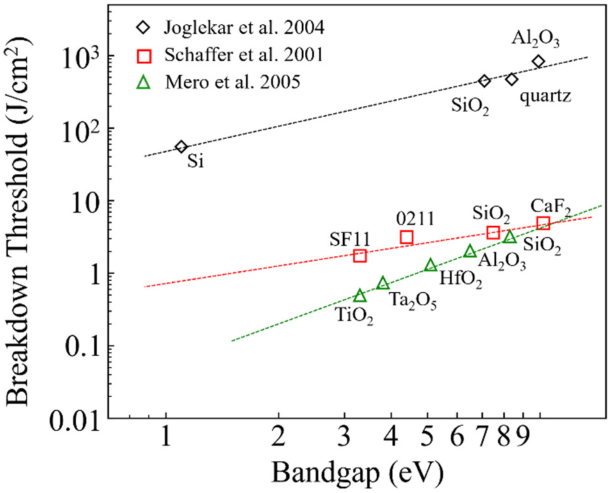

Figure 4-1: F_{th} vs E_g data showing a linear scaling for data measured from multiple literature sources.

Joglekar et al. were also able to conclude in favor of AI simply by the sharp features of ablation; relating the smooth boundaries of their ablation features with a 4 nm variation to the avalanche volume required for a single electron to initiate AI.

The investigations on hBN ablation in this work would be incomplete without an examination of its place within the current ablation research landscape. It is interesting to compare the fluence threshold of hBN to other large band-gap materials and see what mechanisms occur within the material under ultrafast strong-field illumination.

4.2 The role of defects in optical breakdown

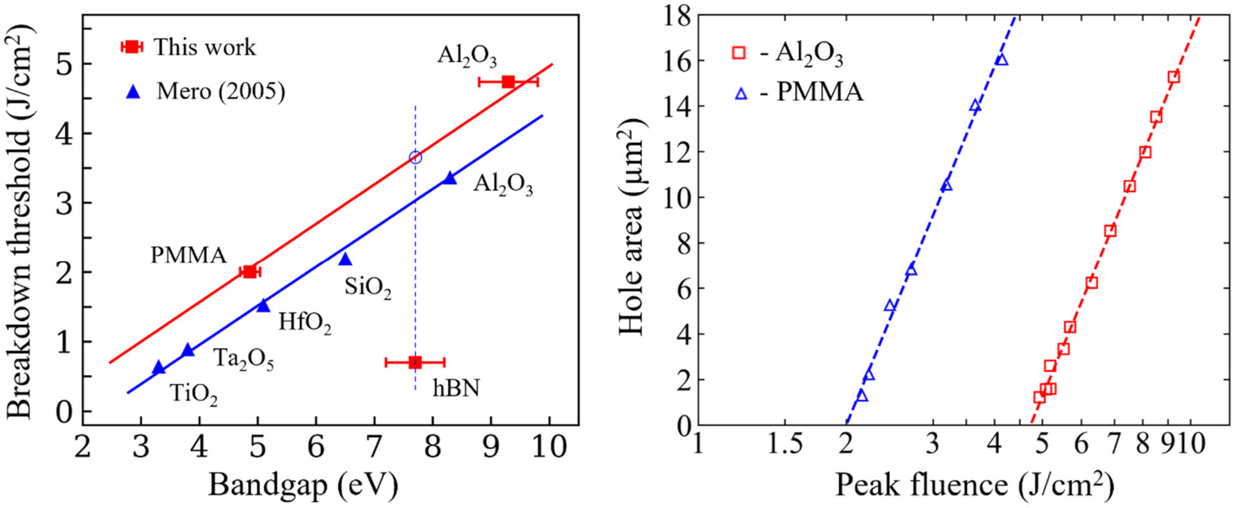

Figure 4-2: (a) Breakdown threshold vs. bandgap for hBN monolayer, Al_2O_3, and PMMA, obtained in this work. Also included are data (red triangles) from Mero et al. for comparison. (b) Hole area vs peak fluence for PMMA and Al_2O_3.

Figure 4-2(a) compares the surface breakdown threshold of bulk PMMA (2.0 J/cm^2) and Al_2O_3 (4.7 J/cm^2) (see Figure 4-2(b)) and the breakdown threshold of hBN (0.7 J/cm^2). For discussion, it also displays the breakdown threshold of various amorphous thin films from Mero et al., measured with a pulse-width like that in this work. Mero's work, along with Joglekar's as well as Schaffer's, shows a linear scaling of F_{th} with E_g. If this linear scaling is applied to the PMMA and Al_2O_3 data points¸ the red empty circle is the interpolated F_{th} ~ 3.8 J/cm^2 for a fictitious bulk dielectric with a bandgap energy of 7.7 eV, which is 5.4 times larger than experimentally measured F_{th} of the monolayer hBN. Physical imperfection on the surface, such as sub-wavelength cracks, grooves, and voids, were reported to lower breakdown threshold of bulk dielectrics by a factor of 2 to 5 via electric field enhancement (122). This is likely not the case here, as all our ablated holes are at the geometric center of the laser beam and their shapes resemble the beam, even though very fine surface scratches are present within the hole (see the upper right corner of the hole in Figure 3-12(a)). The region on the boundary immediately outside the hole also does not present significant tears or small holes despite the presence of scratches there.

Atomic defects are also known to lower the breakdown threshold of bulk dielectrics and could potentially have a contribution here. Defects could lower F_{th} mechanically by weakening bonds enough to destabilize the lattice and by building up tensile pressure, and was the proposed cause for a 4x reduction in XUV ablation threshold of LiF by molecular dynamic simulation (123). Defects could also do so electronically by seeding electrons to the conduction band. It is generally accepted that optical breakdown is initiated by seed carriers followed by AI (122). In the absence of defects, such seed electrons are generated from photoionization of valence electrons. In the presence of defects, however, they can be background carriers from shallow donors or derived from photoionization of occupied intragap defect states. The latter possibility was examined by Hellwarth et al., who showed a deep-lying impurity density of $10^{18}\ cm^{-3}$ is required to lower breakdown threshold of polar crystals (122). Joglekar et al. estimated the same $10^{18}\ cm^{-3}$ figure as being the carrier density required to initiate AI in various materials with varying bandgaps. With this in mind, we characterized the presence of defects in our samples and their corresponding effects on material properties using a combination of various optical spectroscopies and further experimentation.

4.2.1 Photoluminescence (PL) spectroscopy

Photoluminescence (PL) spectra of hBN on fused silica and bare fused silica substrate were taken using 532 nm excitation in the Raman system described in section 2.3.3. In the case of fused silica the LO, TO and ‘cage’ Raman peaks are clearly visible at ~567.8 nm (1185 cm^{-1}), ~563.61 nm (1054 cm^{-1}) and ~555.7 nm (801 cm^{-1}) respectively (124). The same peaks are visible in the hBN spectrum. Beyond 571 nm the film exhibits no features that can be convincingly claimed to be above the noise floor, attributable to vis-NIR defects, and that also do not appear in the bare substrate spectrum.

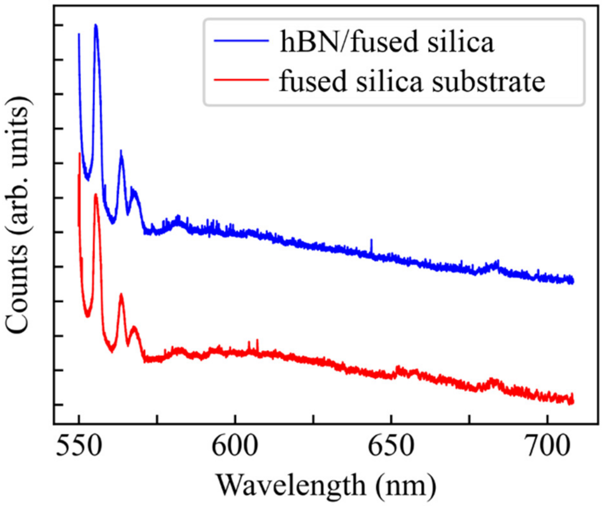

Figure 4-3: PL spectrum of hBN on fused silica (blue trace), and bare fused silica substrate. The spectra are offset vertically for clarity.

The literature has some discussion on the nature of radiative defects in hBN and are elucidated here. N_BV_N defects are those where a Nitrogen atom occupies a Boron site and has a neighboring N vacancy (125). There is typically a broad emission attributed to the zero-phonon line (ZPL) of the N_BV_N defect at 623 nm (44, 125). Cubic Boron-Nitride (cBN) color centers have a narrow emission peak at 640 nm (44). Point defects such as $C_BC_NC_BC_N$ carbon complexes in hBN have been shown to have emission at 575 nm (126).The characteristic peaks and emission lines from these types of radiative defects are all absent from our spectra, leading us to conclude that the vis-NIR defect density in our samples is quite low. This is confirmed for all three samples that were experimented on for this work.

4.2.2 UV-vis-NIR absorbance and Raman spectroscopy

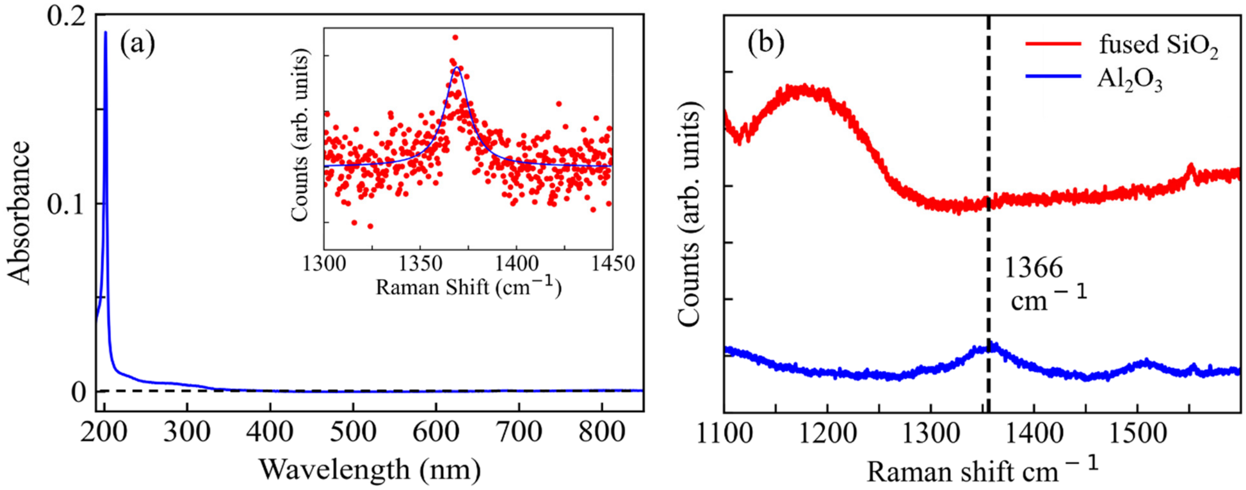

Figure 4-4: UV-vis-NIR absorbance spectra for hBN/fused SiO_2. (inset) Raman spectrum of hBN with the background subtracted. (b) Raman spectra of bare fused SiO_2 and Al_2O_3 substrates.

The defects present in our hBN samples might not present PL emission but still might be optically absorptive, thus an absorbance spectrum can prove useful. The UV-vis-NIR absorbance spectrum (Figure 4-4(a)) shows a narrow exciton absorption band around 201 nm and an absorption tail in the range of 215-400 nm (3.1 - 5.7 eV). Similar absorption spectra from CVD-grown hBN were reported earlier that were attributed to optical transitions associated with common defects in hBN, including substitutional carbon impurity on nitrogen sublattice (C_N), the boron vacancy (V_B), the nitrogen vacancy (V_N), and the boron-nitrogen vacancy (V_{BN}) (127, 128). Thus, defects are established to be present in our samples, even if they don't fluoresce. The next question that arises is whether the presence of such defects affects material properties, and this can be probed using Raman spectroscopy. The Raman signature of materials is typically determined by various mechanical parameters such as material strain (107) and the presence of dangling bonds in the case of nano-voids and vacancies in samples as was examined in the case of MoS_2 earlier in section 3.2.

It was noted earlier that all experiments were performed for hBN film on fused SiO_2 substrates and not Al_2O_3, even though Al_2O_3 is a good candidate for such high intensity experiments due to its large bandgap. One of the reasons for this is that with Al_2O_3 substrates the Raman measurement of hBN is not possible. Al_2O_3 exhibits its own Raman peak at 1366 cm^{-1} that interferes with and suppresses hBN's Raman signature (Figure 4-4 (b)). Our Raman spectrum displays a peak wavelength of 1367 cm^{-1} and a FWHM linewidth of 20 cm^{-1} (see the inset in Figure 4-4(a)). The peak position is red-shifted with respect to that of exfoliated monolayer supported on substrates (~ 1369 cm^{-1}), which we attribute to tensile strains originating from these atomic defects (105, 107). The Raman linewidth is larger than that of exfoliated monolayer on substrates (~ 10-13 cm^{-1}), which we attribute to in-homogeneously distributed strain fields within the micrometer-sized laser spot, as the monolayer follows the substrate's roughness (107). As for the defect density, transport studies have reported a trap density anywhere between $10^{12} - 10^{17}\ cm^{-3}$ for exfoliated hBN (129, 130). Given that the defect density can be 2-3 orders higher for CVD hBN (130), this amounts to a maximum bulk defect density of $10^{19} - 10^{20}\ cm^{-3}$, corresponding to a surface density of $10^{12} - 10^{13}\ cm^{-2}$ for monolayer hBN and a mean separation of 3-10 nm between defects. It is evident that there are an abundant number of defects interacting with the laser pulse. If the presence of these defects lowers F_{th}, either mechanically or electronically, then artificially adding more defects should reduce it further. To verify this hypothesis, the sample was exposed to repeated laser pulses to test the addition of laser-induced defects and probe their subsequent effect on the multi-pulse breakdown threshold $F_{th}(N)$, where N is the admitted number of pulses incident on the hBN monolayer.

4.2.3 Multi-pulse breakdown and material degradation

First the addition of laser-induced defects to the sample by multiple laser pulses below F_{th} was tested. The experiment was performed by creating a matrix of femtosecond exposed areas where a column of exposures corresponded fluences of 0.7 F_{th}, 0.8 F_{th} and 0.9 F_{th} (or slightly below these fluences). Each row then corresponded to a specific number of laser shots. Since these exposures were all sub-threshold (which are confirmed to be below threshold since no hole is visible via DIC), accurate positioning when collecting Raman signals from the center of each area exposed to sub-F_{th} pulses is critical. To ensure this, two 'marker' holes were made with a higher fluence (~1.5 F_{th}) on a either side of the sub-F_{th} exposed area. This protocol is shown in the DIC image in Figure 4-5(a), where 3 columns of marker holes are visible via DIC and the sub-F_{th} exposed areas indicate visible material ablation. This experiment's parameters introduce the issue of the substrate material (fused SiO_2) exhibiting its own incubation effects that modify the Raman signature of the substrate. As an example, a blank SiO_2 sample with no film served as a control and was exposed to femtosecond pulses under the same conditions as the one with hBN and Raman signatures were collected from the blank sample as well. The Raman signature of the fused SiO_2, substrate being modified by the laser is exhibited in the scan shown in Figure 4-5(b) where a clear fluorescence signature appears for wavelengths smaller than ~650 nm.

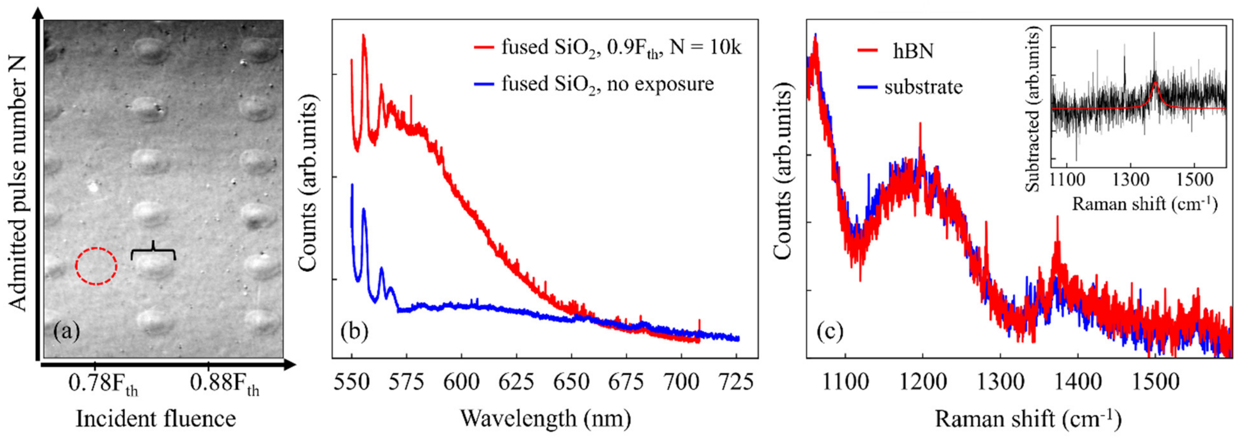

Figure 4-5: (a) DIC image of an area with sub-F_{th} exposures (an example exposure is marked by the red circle). Marker holes are visible on either side of a sub-F_{th} exposed area (an example marker hole is marked by the black curled bracket). (b) PL spectra of bare fused SiO_2 with no exposure (blue trace) and fused SiO_2 with exposure to 10k pulses (red trace). (c) Substrate scan (blue trace) that was scaled multiplicatively and shifted vertically to remove the fused SiO_2 signature. (inset) subtracted spectrum (black trace) then fitted with a Lorentzian function (red trace).

To look at just the effect on the hBN film Raman signals around 1366 cm^{-1} were collected from both the femtosecond exposed hBN/fused SiO_2 (see Figure 4-5(c), red trace, for the case of an exposure where N = 10k and F ~ 0.88 F_{th}) as well as the fused SiO_2 substrate (Figure 4-5(c), blue trace). The substrate scans were then shifted vertically and scaled multiplicatively to match the SiO_2 peaks in the Raman spectra collected from the hBN/ fused SiO_2 and subtracted (Figure 4-5(c) inset, black trace). A Lorentzian function is then used to fit the subtracted signal (Figure 4-5(c) inset, red trace). The extracted amplitude, center shift, FWHM and area under the curve (AUC) from the fitted Lorentzian functions are displayed in Figure 4-6.

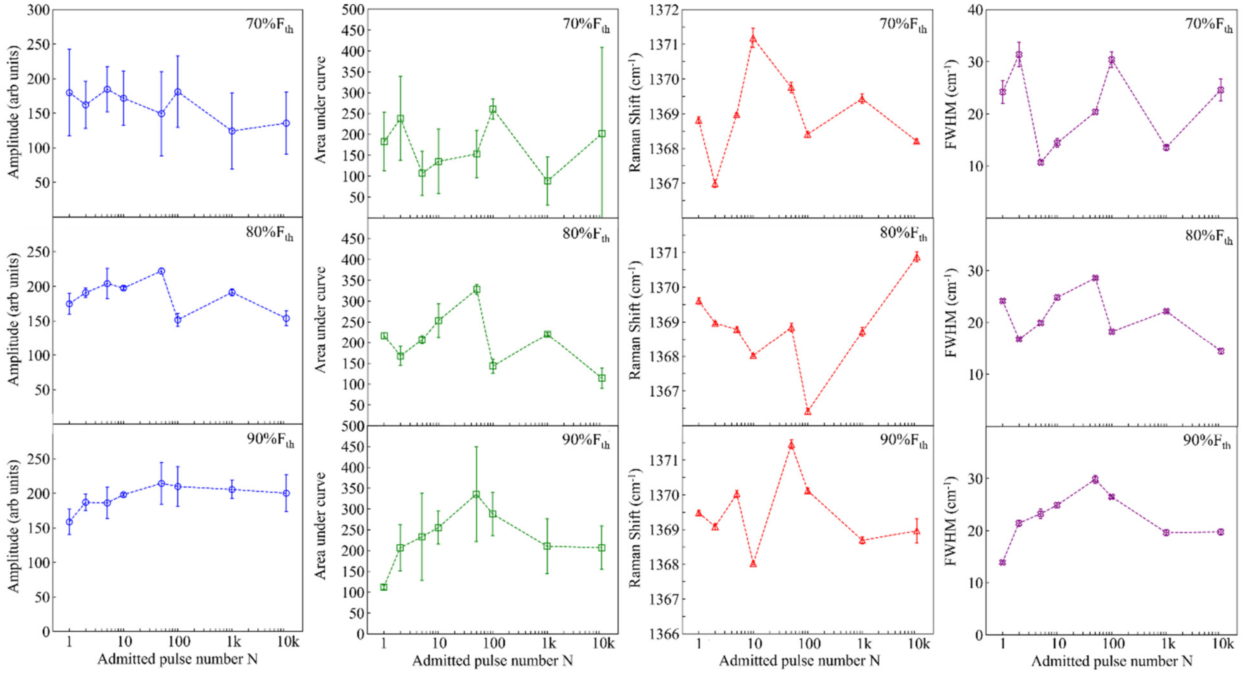

Figure 4-6: Sub- F_{th} data collected from the fitted Lorentzian functions for different incident fluences collected following the scheme in Figure 4-5. The 1st column (blue traces) is the fitted amplitude, 2nd column (green traces) is the area under the curve, 3rd column (red trace) is the center Raman shift and 4th column (purple traces) is the FWHM.

The returned data shows no discernible trend in the data, even at very high fluences up to ~90% of the breakdown threshold for hBN on fused SiO_2. This result can either indicate that repeated femtosecond exposure does not add defects to the hBN film or that the added defects do not affect the Raman spectrum, even at fluences as high as 0.88 F_{th}. This result necessitates looking fluences even higher, above the material breakdown threshold. These experiments were performed, and the data are shown in Figure 4-7.

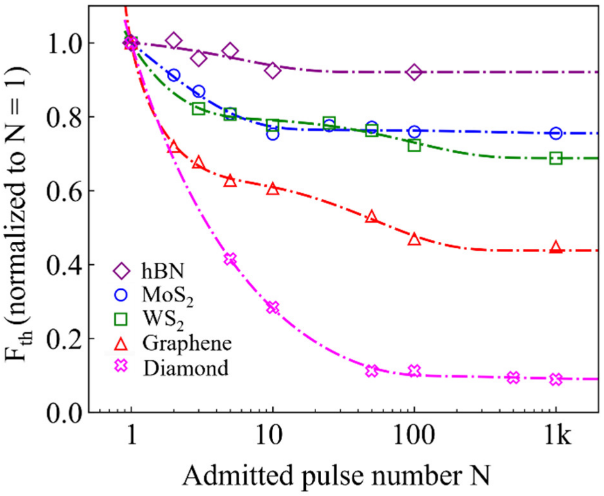

Figure 4-7: Experimentally determined multi-shot breakdown threshold $F_{th}(N)$ data for hBN, MoS_2 and WS_2. Data for graphene and diamond from literature sources is also shown for comparison.

The data is displayed in (c) along with the data presented earlier for MoS_2, WS_2, graphene and diamond. The data indicates a very weak dependence of F_{th} on the admitted pulse number: $F_{th}(N)$ drops only by less than 10% for 10 pulses compared to the single pulse. According to the theory of incubation (85), as $F_{th}(N)$ is only slightly smaller than $F_{th}(1)$, the first *N-1* pulses in the *N* pulse train will surely add defects and yet the N^{th} pulse needs a fluence comparable to $F_{th}(1)$ to induce breakdown. This means all the defects created by the leading *N-1* pulses do very little to lower the breakdown threshold.

4.2.4 Spot size dependence of F_{th}

Further evidence toward this conclusion is provided by an investigation of the spot size dependence of hBN. Other reports in the literature have investigated the relationship between the material breakdown threshold and the laser spot size with most seeing an increase in F_{th} with an increase in spot radius (131). This effect has typically been linked to the increase in the probability of the laser beam encountering defects with an increase in spot radius. The obtained data is shown in Figure 4-8.

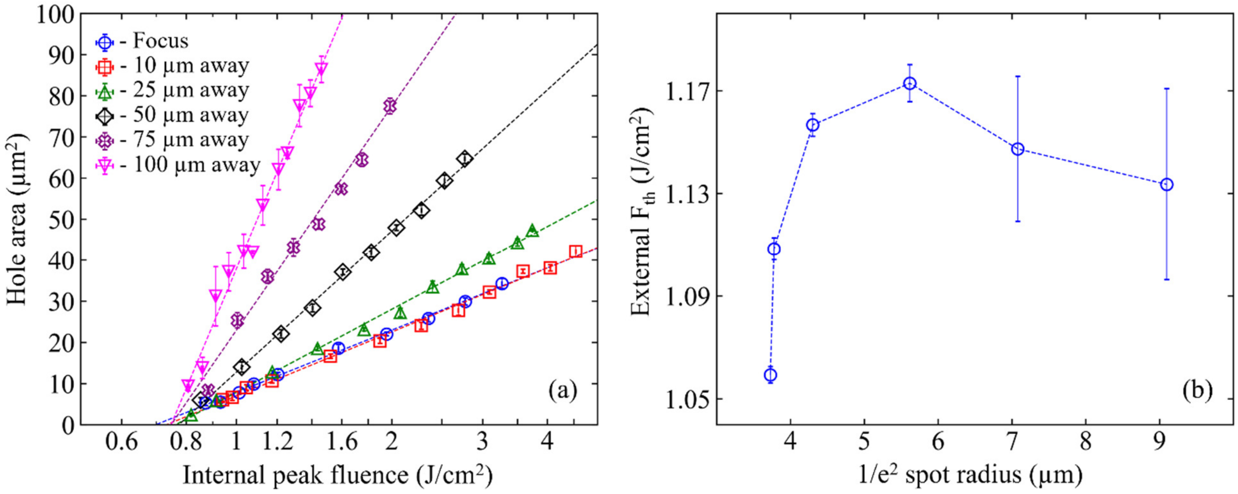

Figure 4-8: Spot size dependance data for hBN on fused SiO_2/Si. (a) Individual Liu plots for each distance away from the laser focus. (b) Extracted F_{th} vs spot radius extracted from the Liu plots in (a).

The returned data shows an initial increase in the breakdown, a small dip and after that a saturation of F_{th} occurs, instead of the typical reduction in F_{th} with spot radius seen in bulk glass (131). This provides further evidence that the presence of defects in the film does not affect the material breakdown threshold significantly.

4.2.5 Numerical modelling on the effects of defects

To round out the theme of the effects of defects and further support the notion that the defects present in the sample do not affect ODB, numerical modeling is offered. A simple model of a bulk dielectric with pre-existing background carrier density n_{e0} and one intragap defect state with an initial density n_{d0} (see the inset of Figure 4-9) is considered.

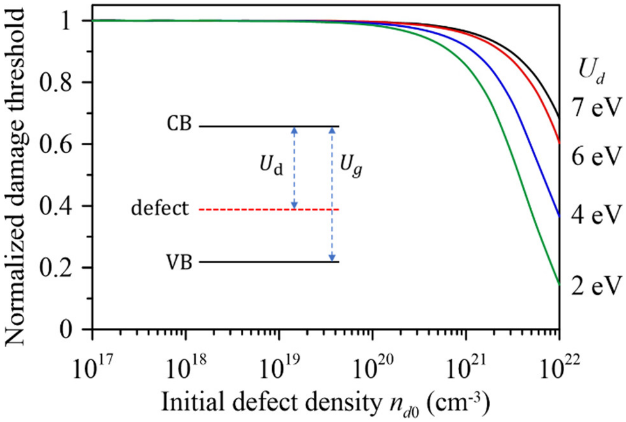

Figure 4-9: Simulation results of the F_{th} vs the initial defect density.

Denoting the carrier density in the conduction band as n_e, the initial valance band electron density as n_{v0}, the intragap defect density as n_d , and the atomic density as n_a, the transient population evolution for n_e and n_d including saturation can be described by the following simple rate equation (132):

$$\begin{aligned}
\frac{dn_e}{dt} &= \left[\alpha W_{PI}\left(U_g\right)+\gamma W_{AI}\left(U_g\right)n_e\right]\left(1-\frac{n_e}{n_{v0}}\right)+\left[W_{PI}\left(U_d\right)+W_{AI}\left(U_d\right)n_e\right]\left(\frac{n_d}{n_a}\right)-\frac{n_e}{\tau_c} \\
\frac{dn_d}{dt} &= \frac{n_e}{\tau_{cd}}-\left[W_{PI}\left(U_d\right)+W_{AI}\left(U_d\right)n_e\right]\left(\frac{n_d}{n_a}\right)
\end{aligned} \tag{4.1}$$

where U_g is the gap energy between the valance band (VB) and the conduction band (CB), U_d is the energy between the intragap defect and the CB, τ_c is the carrier lifetime, and τ_{cd} is the carrier relaxation time from the conduction band to the defect state. In Eq.4.1, $W_{PI}(U_g)$ is the photoionization rate per unit volume, which is calculated by using Keldysh's photoionization theory (Eqs. (4)-(6) of ref.(104)) and can be described by;

$$
\begin{aligned}
W_{PI} &= 2\frac{2\omega}{9\pi}\left(\frac{m_r\omega}{\hbar\sqrt{\gamma_1}}\right)^{3/2} Q(\gamma,\nu)\times\exp\left(-\pi\frac{K(\gamma_1)-E(\gamma_1)}{E(\gamma_2)}N\right) \\
Q(\gamma,\nu) &= \sqrt{\frac{\pi}{2K(\gamma_2)}}\sum_{l=0}^{\infty}\exp\left(-l\pi\frac{K(\gamma_1)-E(\gamma_1)}{E(\gamma_2)}\right)\times\Phi\left(\sqrt{\frac{\pi^2\left(N-\nu+l\right)}{2K(\gamma_2)E(\gamma_2)}}\right)
\end{aligned}
\tag{4.2}
$$

where $m_r = m_e m_h/(m_e + m_h)$ is electron-hole reduced mass, ω is the angular frequency of the light, $\gamma = \omega\sqrt{m_r U}/(e\bar{E})$ is the Keldysh parameter that can be computed from the laser electric field $\bar{E}$ and the bandgap, K and E are complete elliptic integrals of the 1st and 2nd kind respectively, with arguments $\gamma_1 = \gamma^2/(1+\gamma^2)$ and $\gamma_2 = 1/(1+\gamma^2)$, $\Phi(\mathrm{z}) = \int_0^z (y^2 - z^2)dy$ is the Dawson integral, and $N = \langle \nu + 1 \rangle$, where $\nu = 2E(\gamma_2)/(\pi\gamma_1) \times U/(\hbar\omega)$ corresponds to the effective ionization potential normalized to photon energy. Note that the factor of 2 on the left-most side of W_{PI} results from the inclusion of electron spin degeneracy.

The second important term in the rate equation is the avalanche ionization rate per conduction electron $W_{AI}(U)$, for a transition across a bandgap energy U and is taken from a model based on the ratio of the laser plasma heating rate to the effective bandgap required for impact ionization (133):

$$
\begin{aligned}
W_{\mathrm{AI}} &= \frac{\sigma_c \bar{E}^2/2}{\tilde{U}} \\
\sigma_c &= \frac{e^2\tau_s}{m_e\left(1+\omega^2\tau_s^2\right)}
\end{aligned}
\tag{4.3}
$$

where σ_c is the AC conductivity of an electron, m_e is the electron effective mass, and τ_s is the electron collision time. The effective bandgap is defined by $\tilde{U} = (2 - m_r/m_e)(U + e^2\bar{E}^2/4m_r\omega^2)$, which considers the conservation of energy and momentum during the collision between free and bound charges and the quiver/pondermotive energy of carriers in the CB. In the case of there being no defects the carrier density due to defects n_{d0} can be set to zero and Eq.4.1 can be expressed as

$$\frac{dn_e}{dt} = \left[\alpha W_{PI}\left(U_g\right) + \gamma W_{AI}\left(U_g\right) n_e\right]\left(1 - \frac{n_e}{n_{v0}}\right) - \frac{n_e}{\tau_c}. \tag{4.4}$$

The parameters in the rate equations above are known to overestimate AI and the choice of these models for $W_{PI}(U)$ and $W_{AI}(U)$ are not unique. For a given incident fluence, one can find $W_{PI}(U)$ and $W_{AI}(U)$ by calculating the requisite Keldysh parameter etc. but these calculated rates might yield carrier densities from the rate equations that are too high. Thus, Eqs.4.1 and 4.4 include two multiplicative fitting parameters, α and γ, that adjust the strength of $W_{PI}(U)$ and $W_{AI}(U)$, respectively when fitting to a given fluence.

With Eqs. 4.2 - 4.3, the peak total n_e can be solved from the rate equations Eq.4.1 or Eq.4.4 under the initial conditions of the initial carrier concentration in conduction band n_{e0} and the initial defect density n_{d0}. Table gives other requisite parameters for the calculations.

Table 4.1: Required material parameters for solving rate equations in Eq.4.4. Laser beam parameters are λ = 800 nm and τ = 160 fs. The τ_{cd}lifetime is assumed to be equal to τ_c.

U_g (eV)	m_e	m_h	n_{v0} (cm^{-3})	n_a (cm^{-3})	τ_c (ps)	τ_s (fs)
7.7	$0.83m_{e0}$ (17)	$0.63m_{e0}$ (17)	2.55×10^{23}	6.38×10^{22}	430 (134)	1 (135)

First, the AI strength of the fictitious bulk (3D) material was estimated assuming the presence of no defects. The interpolated breakdown threshold fluence F_{th} of 3.8 $\mathrm{J/cm^2}$ gives the electric field strength E required to calculate the Keldysh parameter, $W_{PI}(U)$, $W_{AI}(U)$, etc. Eq. 4.4 is numerically integrated while setting $\alpha = 1$ and treating γ as a fitting parameter (denoted as γ_{3D}) while looking at the total CB carrier density n_e. Breakdown is defined to occur when n_e at the center of the pulse (denoted as $n_{e,\mathrm{cri}}$) equals 5% of the VB density n_{v0} (136). The obtained γ_{3D} equals 0.085.

The pre-existing background carrier concentration n_{e0} in the sample can be estimated as outlined next. Chen et al. used a growth technique similar to one used here and reported a resistivity of 529 $\Omega\ cm$ for monolayer hBN flakes (137). Assuming an electron mobility of 35 $cm^2/V \cdot s$ (138), this translates to a background carrier density of $n_{e0} \sim 10^8\ cm^{-3}$. Numerically, this initial condition was found to have no influence on the total n_e. Stuart et al. has shown that, assuming a temporally flat pulse, Eq. 4.4 can be simplified to define an effective photoionized carrier density as $W_{PI}(U_g)/W_{AI}\ (U_g)$ (139). This number is estimated to be ~ $3.3 \times 10^{21}\ cm^{-3}$ at the breakdown threshold of this fictitious bulk material with $F_{th} = 3.8\ \mathrm{J/cm^2}$, $U_g = 7.7$ eV, $\alpha = 1$, and $\gamma = \gamma_{3D} = 0.085$. This photoionized carrier density is 13 orders of magnitude larger than n_{e0} leading to the conclusion that background carriers from shallow donors have no effect on F_{th}.

Next, the effect of the initial defect density (n_{d0}) on the reduction of F_{th} of the fictitious bulk material was evaluated, as seen in Figure 4-2(a), from the new F_{th}. The breakdown criterion is again set to when $n_{e,\mathrm{cri}} = 0.05 n_{v0}$. Parameters such as $U_g = 7.7$ eV, $\alpha = 1, \gamma = \gamma_{3D} = 0.085$ were set and the bandgap U_d of the intragap defect states in hBN was obtained from literature that estimated using density functional theory. Wirtz et al. showed that C_N, V_B, and V_{BN} defect states have energy levels close to the VB with $U_d \leq 7\ eV$, while V_N has an occupied mid-gap state with $U_d \approx 4.1$ eV from the conduction band edge. Thus, a variety of defect bandgaps could be appropriate. Eq. 4.1 was numerically integrated and the resulting new F_{th}, normalized to the intrinsic threshold of 3.8 J/cm^2, is displayed in Figure 4-9 as a function of initial defect density n_{d0} for selected defect bandgap energies U_d. The results indicate that even for an extremely high defect density of $n_{d0} = 10^{20}\ cm^{-3}$, the breakdown threshold stays nearly the same for $4\ \leq U_d\ \leq\ 7\ eV$. It appears that intragap defect states have a negligible effect on F_{th}.

It should be noted that, even though the choices of $W_{PI}(U)$ and a 5% critical carrier density (136) for breakdown are somewhat arbitrary, the conclusion drawn from this analysis can be checked for robustness against variation in the parameters used. The normalized F_{th} vs. n_{d0} is examined under three extreme scenarios, including (a) $(\alpha = 0.1, n_{e,\mathrm{cri}} = 0.05 n_{v0})$ (weak PI), (b) $(\alpha = 3, n_{e,\mathrm{cri}} = 0.05 n_{v0})$ (strong PI), and (c) $(\alpha = 1, n_{e,\mathrm{cri}} = 0.2 n_{v0})$ (high breakdown criterion). The bandgap of the defect state U_d is fixed at 4 eV. The result is demonstrated in Figure 4-10. Again, even for very high defect density of $n_{d0} = 10^{20}$ cm^{-3}, the reduction of normalized F_{th} is below 3%.

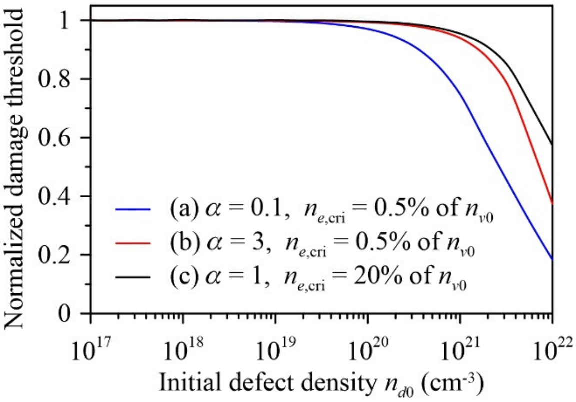

Figure 4-10: Normalized F_{th} vs. n_{d0} under three different scenarios defined in the part IV of this section.

These findings all lead to the conclusion that defects do not cause the observed reduction in F_{th} that is seen for hBN compared to the other large bandgap materials. Avalanche Ionization becomes a more convincing proposition as the cause. To estimate the AI strength of the monolayer (2D) material, Eq. 4.1 is solved with $\alpha = 1$ and γ is again treated as a fitting parameter (denoted as γ_{2D}) to fit the measured breakdown threshold fluence F_{th} of $0.7\ \mathrm{J/cm^2}$. The breakdown criterion is also set $n_{e,\mathrm{cri}} = 5\%$ of n_{v0}. The obtained γ_{2D} equals 2.013. In comparison to that for the interpolated bulk $\gamma_{3D} = 0.085$, the obtained AI coefficient for 2D hBN appears to be vastly enhanced (~24×).

4.2.6 Mechanical strength of bulk materials vs hBN

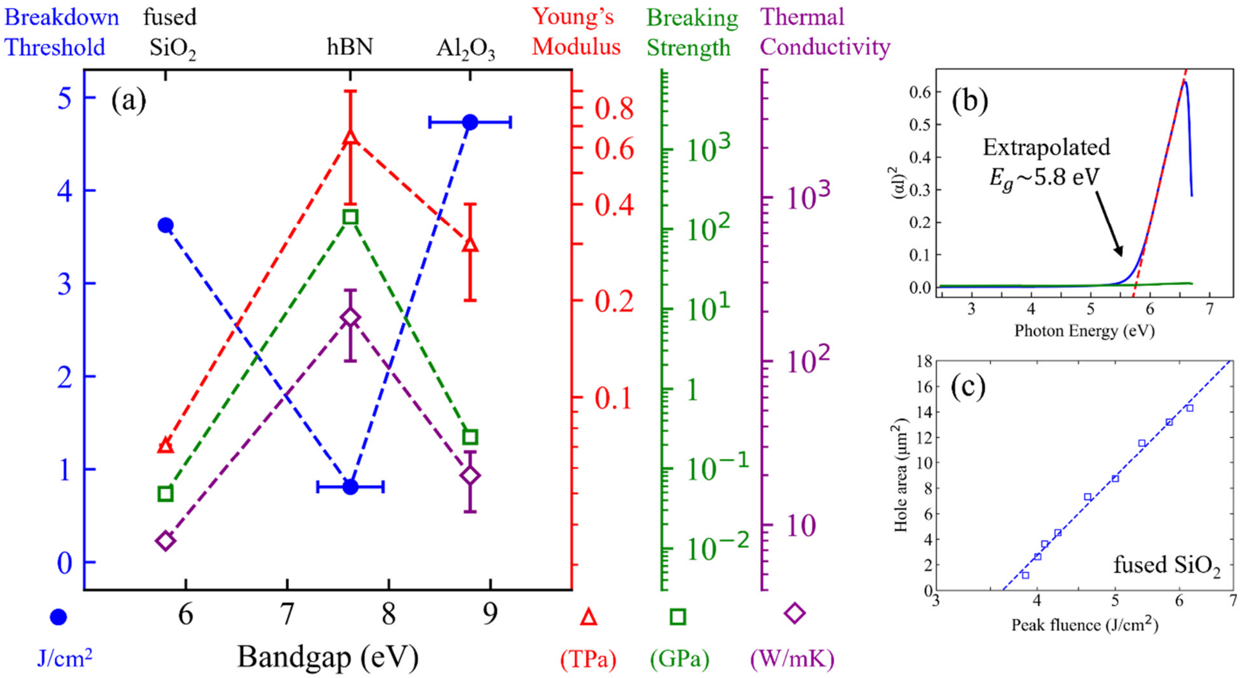

Figure 4-11: (a) Comparison of the ablation threshold, Young's modulus, breaking strength, and thermal conductivity of fused SiO$_2$, hBN monolayers, and Al$_2$O$_3$. (b) Estimation of the bandgap of fused SiO$_2$ from a UV-vis absorbance measurement (l is the sample thickness). (c) Liu plot to determine breakdown threshold of fused SiO$_2$ (~ 3.6 J/cm^2).

An additional argument for a nonlinear process such as MPI or AI to be enhanced as the explanation for the reduced F_{th} of hBN monolayers compared to the bulk equivalent material can be found by looking at the mechanical properties of the bulk and 2D materials. Figure 4-11(a) displays the surface breakdown threshold F_{th} for fused SiO_2 (~3.6 J/cm^2) and Al_2O_3 (~4.7 J/cm^2), and the intrinsic breakdown threshold F_{th}^{intr} of hBN (0.7 J/cm^2). The drastically lower F_{th} for hBN is intriguing. Even though hBN monolayers have a bandgap energy between fused SiO_2 and Al_2O_3 ($E_g \sim 9.35 \pm 0.55$ eV), its F_{th}^{intr} is 5.1× smaller than that of quartz and 6× smaller than that of Al_2O_3. This is even more surprising if we consider that hBN monolayers have a Young's modulus comparable to Al_2O_3 and is ~10× larger than SiO_2, a breaking strength 550× larger than Al_2O_3 and 3000× larger than SiO_2, and a thermal conductivity ~10× larger than Al_2O_3 and 10-30× larger than PMMA (see right vertical axes of Figure 4-11 (a);). The mechanical properties for the materials are given in table 4.2. This observation indicates that carrier generation in hBN has to be strong enough to overcome the higher mechanical robustness of hBN such that the ablation threshold is so much lower.

It should be noted that early in this work, UV-vis absorbance was performed to determine the bandgap of fused SiO_2 (see Figure 4-11(b)). There is a prominent peak above 5.8 eV that was used to extrapolate the bandgap. For comparison, UV-vis absorbance of Al_2O_3 is also shown, which shows a much smaller absorbance. On the SiO_2 spectrum, the downturn in the spectrum above ~6.5 eV merited a closer look at the bandgap of SiO_2. Further analysis of theoretical reports placed E_g much higher than the experimental measurements in this work (~ 9 eV instead of 5.8 eV). There exist two prominent defect peaks at ~5.8 eV and at ~7.6 eV (102, 140) in the structure of fused SiO_2 that complicate the interpretation of UV-vis absorbance spectra and the extraction of E_g using the Tauc method, which extrapolates the slope of the absorption edge of a UV-vis absorption spectrum to estimate the direct optical bandgap (141). It should be noted that the term 'optical bandgap' is a somewhat loose term used in the literature to refer to the onset of absorption (due to defects in the case of SiO_2) that is not due to the true electronic bandgap of materials. In the case of 2DMs this is referred to as the excitonic bandgap due to the absorption occurring due to the presence of the exciton resonance. It is possible the defects in SiO_2 aid carrier generation such that the F_{th} is lower than Al_2O_3 but do not enhance it as much as hBN. Regardless, the argument holds since excitonic bandgap for hBN is ~ 6 eV, which is slightly higher than SiO_2's 5.8 eV, yet the material presents a lower threshold.

Table 4.2: Mechanical properties of 2D (graphene and hBN) and bulk (Al_2O_3 and SiO_2) materials from literature sources.

	Young's Modulus (TPa)	Breaking Strength (GPa)	Thermal Conductivity (W/mk)	Refs
graphene	1	130	600	(22, 142)
$MoSe_2$	0.1	13	44	(100, 143)
hBN	0.4-0.9	120-165	100-270	(22)
Al_2O_3	0.2-0.4	0.25	12-28	(144)
fused SiO_2	0.071	0.048	8	(145)

Given that hBN is more robust mechanically, dissipates energy faster, and yet is easier to ablate, the data strongly suggests that the carrier generation in hBN is much more efficient than in quartz and Al_2O_3. Since at breakdown, the Keldysh parameters (146) for quartz, hBN, and Al_2O_3 are estimated to be ~0.83, ~1.57, and ~0.80, respectively (see table 4.3), which are again in the intermediate regime between the multiphoton and tunneling. This provides another piece of evidence toward AI as the reason for the threshold reduction of 2D hBN compared to bulk but it will be good to examine more evidence toward this from the literature.

4.3 Enhanced carrier generation in hBN monolayers

4.3.1 Bandgap scaling of the ablation threshold for 2D materials

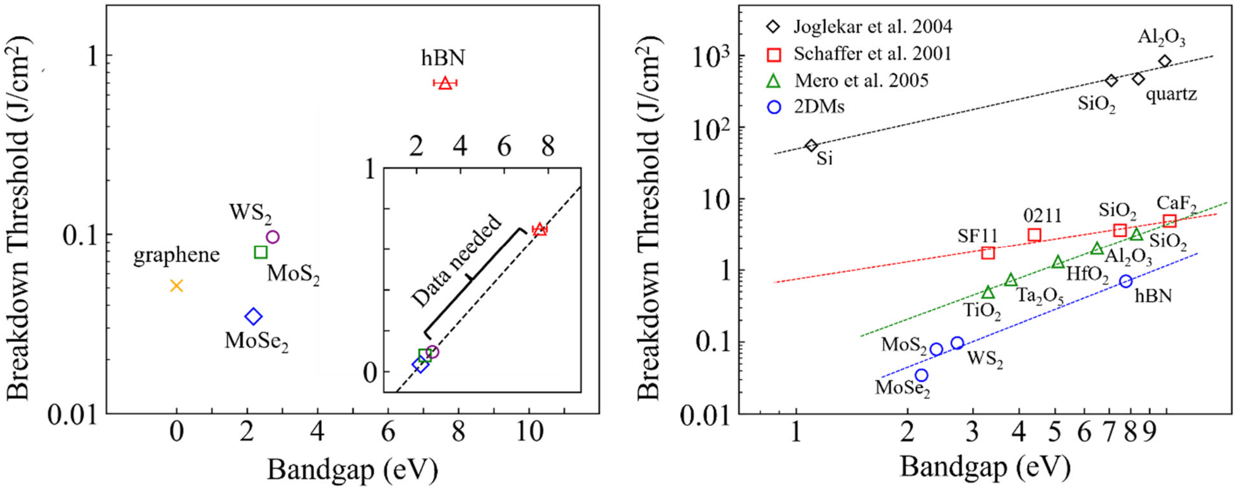

Figure 4-12: A log-linear plot of F_{th}^{intr} vs. electronic bandgap of monolayer 2D materials. The inset shows the same plot in linear-linear scale excluding graphene. F_{th}^{intr} are 51 mJ/cm^2 (graphene, blue), 35 mJ/cm^2 (MoSe$_2$, yellow), 79 mJ/cm^2 (MoS$_2$, green), 97 mJ/cm^2 (WS$_2$, purple), 800 mJ/cm^2 (hBN, red). (b) F_{th} vs E_g for 2DMs measured in this work as well as from literature.

Figure 4-12(a) shows the dependence of the F_{th}^{intr} on the quasi-particle bandgap energy for graphene, MoSe$_2$, MoS$_2$, WS$_2$, and hBN monolayers. Although MoSe$_2$ has a bandgap energy (E_g ~ 2.18 eV) larger than the photon energy of 1.55 eV, it has a strong excitonic resonance at 1.57 eV (10). Both graphene and MoSe$_2$ therefore exhibit strong saturable linear absorption at 800 nm, which is why F_{th}^{intr} for them are among the lowest. Despite its zero bandgap, graphene has a higher F_{th}^{intr} than MoSe$_2$, which we attribute to its exceptional mechanical strength, including a 10× larger Young's modulus and breaking strength. On the other hand, carrier generation in MoS$_2$ (E_g ~ 2.40 eV), WS$_2$ (~ 2.73 eV)(10) and hBN (7.7 ± 0.3 eV) monolayers, which have bandgap energy higher than the photon energy, is expected to be initiated by some form of nonlinear ionization which is then followed by AI.

Table 4.3: Material parameters required for the calculation of the Keldysh parameters for 2D and bulk materials. Laser beam parameters used for the calculation are λ = 800 nm, $\Delta\tau$ = 160 fs.

	Bandgap (eV)	m_e	m_h	F_{th} (J/cm^2)	Keldysh Parameters	Refs
MoS_2	2.40	0.43	0.43	0.079	2.16	(10, 147)
WS_2	2.73	0.44	0.45	0.097	2.11	(10, 147)
fused SiO_2	5.8	0.39	7.5	3.6	0.83	(148)
Al_2O_3	9.3	0.39	6.2	4.7	0.80	(101, 149, 150)

The Keldysh parameters for these materials at their respective breakdown thresholds are estimated to be 2.16 (for MoS_2), 2.11(for WS_2), and 1.57 (for hBN), according to the parameters listed in Table 4. These values are somewhat inconclusive since they indicate that the nonlinear ionization is in the intermediate regime between the multiphoton and tunneling(146) are not strongly biased toward either regime. The linear relationship between F_{th}^{intr} on the bandgap energy clues toward AI being the important mechanism since the quiver energy of the electron would increase with an increase in F_{th}. As noted earlier, similar trends have been reported for bulk materials in the works of Joglekar (40), Mero (47) and Schaffer (121), , although there is a lack of consensus about the exact mechanism. Joglekar argues for AI, Mero for PI and Schaffer is inconclusive. The linear dependency suggested in the inset of Figure 4-12(a), if substantiated by more data points from other 2D materials with a bandgap energy between 3 and 7 eV, would clearly validate a universal scaling law that is independent of materials' dimensionality.

In the literature, it was reported that MoS_2 monolayers have 2- and 3-photon absorption coefficients $10^3\times$ larger than typical bulk materials (151, 152). The authors attributed this enhancement to the excitonic effect, even though the detuning is substantial between the exciton resonance and the photon energy used in those experiments. Such a process can be expected for hBN as well, especially since it has an exciton resonance at 5.6 - 6.3 eV (corresponding to 4-photon absorption of 800 nm) (17). Ji et. al. have reported enhanced 2-photon absorption to exciton states at wavelength $\lambda = 400$ nm and enhanced 3-photon absorption to the defect states at $\lambda = 600\text{-}800$ nm in a 5-layered hBN sample (128). 2DMs are postulated to possess an enhanced electronic density of states near the band edge, which could lead to the nonlinear absorption process being enhanced (153), albeit these can be challenging to detect directly. Otherwise, Auger recombination rates have been reported to be $10\times$ - $10^6\times$ larger in TMD monolayers than in bulk materials, which was attributed to enhanced Coulomb interaction as a result of quantum confinement, reduced dielectric screening, and the large effective masses of electrons and holes in TMDs (154, 155). Since Auger recombination is the reverse process of AI it is possible AI-based carrier generation is similarly enhanced in 2DMs, though this has not been experimentally demonstrated. Future experiments need to be designed and carried out to verify these conjectures.

These postulations have strong implications for future work involving strong-field interaction with 2D materials. As substrates are practically necessary to support 2D materials, it is intuitive to use a substrate with a large bandgap to avoid optical damage. The data in Figure 4-2 eliminates this constraint and enables the use of lower-bandgap materials with additional desired merits. For example, diamond has a lower bandgap (~ 5.5 eV) and 10× better thermal conductivity than hBN. In the quest for high harmonic generation in hBN, it may thus be advantageous to use diamond substrates to dissipate heat efficiently and avoid thermal damage under repetitive high intensity excitation. As another example, Stemme et al. have demonstrated high-speed (50 mm/s) and high-spatial-resolution (100 nm) patterning of $PtSe_2$, MoS_2, and graphene using a commercial femtosecond two-photon 3D printer (117). Low-cost borosilicate glass wafers with a bandgap energy of 3-4 eV can serve as the supporting substrates for large-scale laser pattering of hBN instead of the more expensive pure Al_2O_3.

The optical spectroscopy characterizations, various experiments, and numerical modeling indicate that defects alone cannot explain the 4-5× reduction in F_{th} of hBN monolayers compared to the bulk equivalent. Mechanical arguments and purview of the literature on nonlinear mechanisms imply that AI is the cause. In reality, both photoionization and AI in hBN could be enhanced and further experiments that probe AI more directly need to be undertaken.

4.3.2 Investigation of AI via polarization dependence of F_{th}

The explorations of the previous sections have hinted toward the dominance of AI as the primary carrier generation mechanism in hBN under strong ultrafast light. Experimentally probing the generation process and differentiating between MPI and AI can be done via relatively simple experiments. Since MPI's efficiency depends on the material effective mass, a quantity that can vary in different directions of k-space, rotating the polarization of the incident light at constant incident peak fluence and observing the area of the ablated features can be an effective experiment, like the work of Golin et al. (119) and Li et al. (120). One issue in probing MPI this way is the inability to determine the polarization angle with respect to the crystal lattice orientation for continuous films, such as the hBN films used in this work. In the case of 2DM flakes, such as those grown for MoS_2 or WS_2, the triangular shape of the flakes allows determination of the angle of the armchair or zig-zag directions of the lattice, due to the way the films are grown via CVD. Second harmonic generation (SHG) can be used to determine the lattice orientation but SHG in monolayer hBN is quite weak (42) and difficult to detect, requiring the use of techniques that are impractical such as plasmonic tweezers (156). Since the goal is to detect the presence of MPI, knowing the exact film orientation is not strictly necessary. Like graphene, hBN's lattice has 3-fold symmetry so the effective masses are expected to differ only within a 120° angle. Rotating the incident polarization by 120° should be enough to detect any significant changes in F_{th}, regardless of the original film orientation. Thus, holes were made at a single shot constant fluence ($F_{incident} = 2076$ mJ/cm^2 ~ $1.52\,F_{th}^{intr}$ cutting holes with average area ~ 20.3 μm^2) and then the polarization was rotated by over 120°. Three ablation holes were made for each wave-plate position/polarization angle and the data is displayed in Figure 4-13.

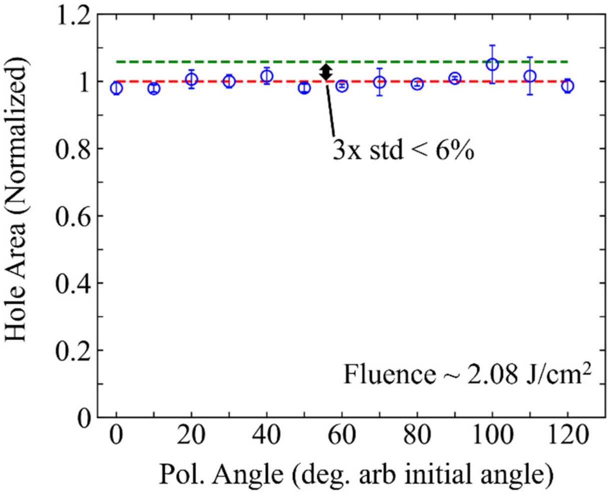

Figure 4-13: Hole area vs polarization angle at a constant incident fluence.

The hole area shows a minimal variation (3x the standard deviation ~5.7%) as the incident polarization is rotated, indicating that MPI plays a minimal role as the generating process for carriers. Alternatively, one can compare F_{th} when using linear polarization (LP) as opposed to circular polarization (CP). For CP light, dephasing between the driving electric field and the driven electrons due to different effective masses would lead to a lower efficiency of carrier generation. This data is shown in Figure 4-14. The results of Liu-plots when changing the polarization of the incoming light reveal small differences between the Liu-plots.

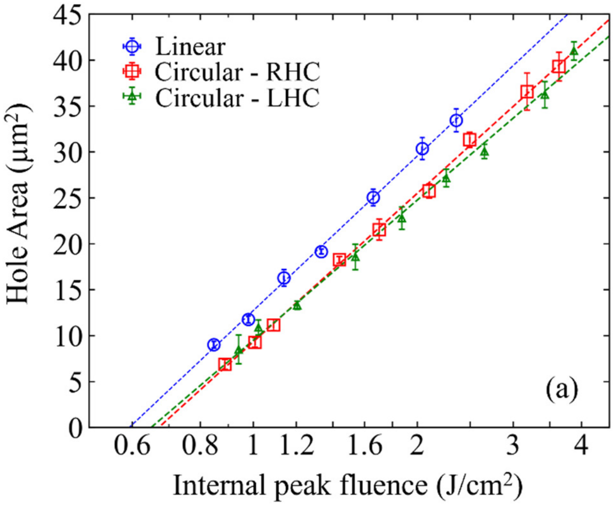

Figure 4-14: Polarization dependence of F_{th} for monolayer hBN with different polarizations of light.

The internal peak fluence threshold and slope-derived spot radius for the linear polarization is ~ 0.59 J/cm^2 and 3.9 µm respectively. For the right-hand circular polarization (RHC) and left-hand polarization (LHC) is 0.67 J/cm^2 and 3.85 µm and 0.65 mJ/cm^2 and 3.74 µm respectively. All three spot radii derived from the Liu plots fall below that measured by the beam profiling microscope, indicating the sample was placed adequately at the laser focus, within the Rayleigh range. The threshold of the LP light is ~10% lower than that of CP light. This could indicate a role for MPA, but the result is small enough to remain unconvincing.

These findings for 2DMs; the minimal change in ablation area w.r.t. rotating incident linear polarization, the similarity of the threshold between linear and circular polarizations, as well as the linearity of the scaling between the bandgap and F_{th}, strongly indicate AI as the dominant mechanism for carrier generation in 2DMs.

4.4 Adding new materials to investigate F_{th} vs E_g

To investigate the relationship between the breakdown threshold (F_{th}) and the material electronic bandgap (E_g) new materials with bandgaps between those of WS_2 (2.7 eV) and hBN (~7.7 eV) are needed.

4.4.1 Finding materials with appropriate bandgaps

The identification of the bandgaps of various materials done for this thesis is presented here. Most works on the bandgaps of novel materials are done via utilizing density functional theory (DFT). It is important to realize that DFT has many different flavors that can affect the overall accuracy of the results. Typically, DFT with some form of local density approximation (LDA) or generalized gradient approximation is used to find the dispersion of the energy bands in a material. One should when examining such works since LDA and GGA, while they might return accurate effective masses and overall correct band curvatures, they are known to severely underestimate the bandgap (157). More accurate methods utilize hybrid functionals, such as HSE06, that can get closer to estimating the correct band-gap (157). So far it appears that methods utilizing the many-body GW approximation predict bandgaps most accurately (158). When examining theoretical works in determining the bandgaps, reports using GW methods were utilized. For this work over 100 materials were examined. Unfortunately obtaining monolayer 2D films, either commercially or via synthesis, with the correct E_g is quite challenging. Thus, bulk materials were obtained that were then thinned via mechanical exfoliation. The materials selected for such exfoliation methods were $Mg(OH)_2$, and $CrCl_3$.

Literature reports examining the band-structure of $Mg(OH)_2$ report a bandgap around 7.7 ± 0.5 eV (159-161), as determined by a combination of theoretical and experimental methods.

Experimental reports report lower bandgaps, with Tongay et al. reporting ~ 4.8 eV, as measured via nano-electron energy loss spectroscopy (nano-EELS) (162), which raises some doubts about the results obtained here. Further analysis of the literature reports is necessary. The nature of the bandgap remains direct going from bulk all the way down to monolayer and the size of the bandgap also remains relatively constant according to Xia et al. (163). In the case of $CrCl_3$, was found from literature to be ~ 4.65 eV (164, 165). Once the material was prepared an ODB experiment was performed, and the results are shown in Figure 4-15.

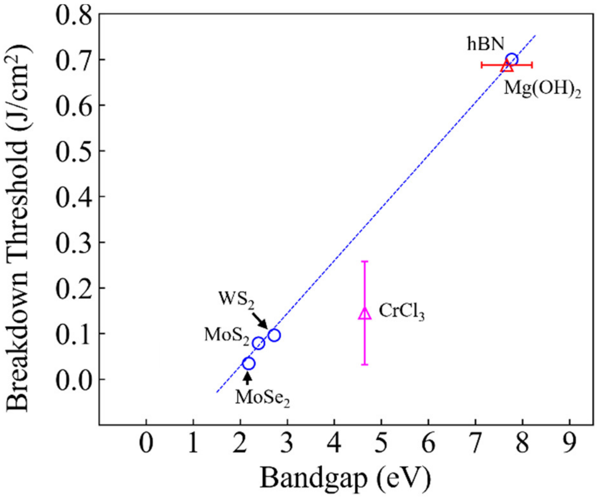

Figure 4-15: F_{th} vs E_g with new 2DMs.

The data point for $Mg(OH)_2$ is somewhat encouraging in that it corresponds pretty well to the hBN data point. Figure 4-15 also displays the results for $CrCl_3$. Each material's F_{th} was corrected using the field enhancement factor squared via the full transfer matrix method using the material and substrate refractive indices. Clearly the observed threshold for $CrCl_3$ deviate from the linear F_{th} vs E_g scaling examined earlier. It should be noted that the large error-bars for the CrCl3 threshold are due to large variations seen when Liu plots were conducted on different flakes, even on the same sample. The large discrepancies in the measured thresholds could be due to several factors. The thickness of $CrCl_3$ and $Mg(OH)_2$ is far from the ideal monolayer and the bandgap structure might be different. The exact bandgap and nature of the bandgap also needs to be examined more rigorously. It is possible that optical anisotropy has an effect as well. Further work needs to be performed to appropriately further test AI for 2DMs.

5 CONCLUSIONS

In this work, femtosecond LDW was established to be a good tool for the patterning of 2D materials. The etalon interference effect on the breakdown threshold of 2D materials was found to be the dominant contributor to the wide variation seen across different substrates. Preliminary patterning was demonstrated for MoS_2 monolayer. Since patterning involves the repeated exposure of the material to multiple high intensity pulses, the multi-pulse breakdown behavior was studied next. It was found that 2D TMDs are extremely optically robust, with incubation R values of around 75%, which is higher than most bulk materials. The nature of the laser-induced defects added by the femtosecond pulses was investigated using various optical spectroscopies. While semiconducting MoS_2 and WS_2 are great candidates for transistors, there is a place for a wide bandgap insulator like hBN in such applications as well. The ODB of hBN was demonstrated and characterized for the first time. It was found that hBN's ablation is quite precise and that the ablation features correspond quite well to the laser beam profile; an attribute that was explained via its ultra-high fracture toughness. The lessons learned from characterization of hBN ablation were then used to demonstrate high-resolution patterning, with impressive features of ~76 nm achieved.

It was found that the breakdown threshold of hBN was far lower than would be expected from a material with a bandgap that high. A thorough investigation of the presence and effect of optical defects showed that defects alone could not explain such a reduction in threshold and that carrier generation in hBN must necessarily be more efficient than in a corresponding bulk material. This was postulated to occur due to avalanche ionization, a claim that was then further investigated by polarization experiments as well as finding a linear scaling between the threshold and the bandgap. Efforts were undertaken to confirm such a scaling by attempting to add more datapoints to the threshold vs bandgap data.

6 BIBLIOGRAPHY

1. Cao W, Bu H, Vinet M, Cao M, Takagi S, Hwang S, et al. The future transistors. Nature. 2023;620(7974):501-15.

2. Auth C, Shankar A. Evolution of Transistors: Humble Beginnings to the Ubiquitous Present. IEEE Solid-State Circuits Magazine. 2023;15(3):20-8.

3. Schwierz F. Flat transistors get off the ground. Nature Nanotechnology. 2011;6(3):135-6.

4. Agarwal T, Szabo A, Bardon MG, Soree B, Radu I, Raghavan P, et al., editors. Benchmarking of monolithic 3D integrated MX2 FETs with Si FinFETs. 2017 IEEE International Electron Devices Meeting (IEDM); 2017 2-6 Dec. 2017.

5. Mas-Ballesté R, Gómez-Navarro C, Gómez-Herrero J, Zamora F. 2D materials: to graphene and beyond. Nanoscale. 2011;3(1):20-30.

6. Novoselov KS, Geim AK, Morozov SV, Jiang D, Zhang Y, Dubonos SV, et al. Electric Field Effect in Atomically Thin Carbon Films. Science. 2004;306(5696):666-9.

7. Bao Q, Loh KP. Graphene Photonics, Plasmonics, and Broadband Optoelectronic Devices. ACS Nano. 2012;6(5):3677-94.

8. Sprinkle M, Siegel D, Hu Y, Hicks J, Tejeda A, Taleb-Ibrahimi A, et al. First Direct Observation of a Nearly Ideal Graphene Band Structure. Physical Review Letters. 2009;103(22):226803.

9. Morozov SV, Novoselov KS, Katsnelson MI, Schedin F, Elias DC, Jaszczak JA, et al. Giant Intrinsic Carrier Mobilities in Graphene and Its Bilayer. Physical Review Letters. 2008;100(1):016602.

10. Gusakova J, Wang X, Shiau LL, Krivosheeva A, Shaposhnikov V, Borisenko V, et al. Electronic Properties of Bulk and Monolayer TMDs: Theoretical Study Within DFT Framework (GVJ-2e Method). physica status solidi (a). 2017;214(12):1700218.

11. Huo N, Konstantatos G. Recent Progress and Future Prospects of 2D-Based Photodetectors. Advanced Materials. 2018;30(51):1801164.

12. Zhang Y, Zhu J, Li P, Wang X, Yu H, Xiao K, et al. All-fiber Yb-doped fiber laser passively mode-locking by monolayer MoS2 saturable absorber. Optics Communications. 2018;413:236-41.

13. Salehzadeh O, Djavid M, Tran NH, Shih I, Mi Z. Optically Pumped Two-Dimensional MoS2 Lasers Operating at Room-Temperature. Nano Letters. 2015;15(8):5302-6.

14. Zhao L, Shang Q, Gao Y, Shi J, Liu Z, Chen J, et al. High-Temperature Continuous-Wave Pumped Lasing from Large-Area Monolayer Semiconductors Grown by Chemical Vapor Deposition. ACS Nano. 2018;12(9):9390-6.

15. Pal A, Zhang S, Chavan T, Agashiwala K, Yeh C-H, Cao W, et al. Quantum-Engineered Devices Based on 2D Materials for Next-Generation Information Processing and Storage. Advanced Materials. 2023;35(27):2109894.

16. Yi Y, Chen Z, Yu X-F, Zhou Z-K, Li J. Recent Advances in Quantum Effects of 2D Materials. Advanced Quantum Technologies. 2019;2(5-6):1800111.

17. Ferreira F, Chaves AJ, Peres NMR, Ribeiro RM. Excitons in hexagonal boron nitride single-layer: a new platform for polaritonics in the ultraviolet. J Opt Soc Am B. 2019;36(3):674-83.

18. Hunt RJ, Monserrat B, Zólyomi V, Drummond ND. Diffusion quantum Monte Carlo and GW study of the electronic properties of monolayer and bulk hexagonal boron nitride. Physical Review B. 2020;101(20):205115.

19. Tancogne-Dejean N, Rubio A. Atomic-like high-harmonic generation from two-dimensional materials. Science Advances. 2018;4(2):eaao5207.

20. Le Breton G, Rubio A, Tancogne-Dejean N. High-harmonic generation from few-layer hexagonal boron nitride: Evolution from monolayer to bulk response. Physical Review B. 2018;98(16):165308.

21. Ares P, Cea T, Holwill M, Wang YB, Roldán R, Guinea F, et al. Piezoelectricity in Monolayer Hexagonal Boron Nitride. Advanced Materials. 2020;32(1):1905504.

22. Li LH, Chen Y. Atomically Thin Boron Nitride: Unique Properties and Applications. Advanced Functional Materials. 2016;26(16):2594-608.

23. Caldwell JD, Aharonovich I, Cassabois G, Edgar JH, Gil B, Basov DN. Photonics with hexagonal boron nitride. Nature Reviews Materials. 2019;4(8):552-67.

24. Cao Y, Mishchenko A, Yu GL, Khestanova E, Rooney AP, Prestat E, et al. Quality Heterostructures from Two-Dimensional Crystals Unstable in Air by Their Assembly in Inert Atmosphere. Nano Letters. 2015;15(8):4914-21.

25. Wang J, Yao Q, Huang C-W, Zou X, Liao L, Chen S, et al. High Mobility MoS2 Transistor with Low Schottky Barrier Contact by Using Atomic Thick h-BN as a Tunneling Layer. Advanced Materials. 2016;28(37):8302-8.

26. Ziegler J, Klaiss R, Blaikie A, Miller D, Horowitz VR, Alemán BJ. Deterministic Quantum Emitter Formation in Hexagonal Boron Nitride via Controlled Edge Creation. Nano Letters. 2019;19(3):2121-7.

27. López JJ, Ambrosio A, Dai S, Huynh C, Bell DC, Lin X, et al. Large Photothermal Effect in Sub-40 nm h-BN Nanostructures Patterned Via High-Resolution Ion Beam. Small. 2018;14(22):1800072.

28. Kim S, Fröch JE, Christian J, Straw M, Bishop J, Totonjian D, et al. Photonic crystal cavities from hexagonal boron nitride. Nature Communications. 2018;9(1):2623.

29. Fröch JE, Hwang Y, Kim S, Aharonovich I, Toth M. Photonic Nanostructures from Hexagonal Boron Nitride. Advanced Optical Materials. 2019;7(4):1801344.

30. Martin AA, McCredie G, Toth M. Electron beam induced etching of carbon. Applied Physics Letters. 2015;107(4):041603.

31. Elbadawi C, Tran TT, Kolíbal M, Šikola T, Scott J, Cai Q, et al. Electron beam directed etching of hexagonal boron nitride. Nanoscale. 2016;8(36):16182-6.

32. Kim M, Pallecchi E, Ge R, Wu X, Ducournau G, Lee JC, et al. Analogue switches made from boron nitride monolayers for application in 5G and terahertz communication systems. Nature Electronics. 2020;3(8):479-85.

33. Mahvash F, Paradis E, Drouin D, Szkopek T, Siaj M. Space-Charge Limited Transport in Large-Area Monolayer Hexagonal Boron Nitride. Nano Letters. 2015;15(4):2263-8.

34. Zhang Z, Yang J, Chen D, Jiang X. Ultra-confined low-loss surface phonon polaritonic resonances in periodically patterned monolayer hexagonal boron nitride. Physica E: Low-dimensional Systems and Nanostructures. 2021;134:114897.

35. Li P, Dolado I, Alfaro-Mozaz FJ, Casanova F, Hueso LE, Liu S, et al. Infrared hyperbolic metasurface based on nanostructured van der Waals materials. Science. 2018;359(6378):892-6.

36. Lassaline N, Thureja D, Chervy T, Petter D, Murthy PA, Knoll AW, et al. Freeform Electronic and Photonic Landscapes in Hexagonal Boron Nitride. Nano Letters. 2021;21(19):8175-81.

37. Garcia AGF, Neumann M, Amet F, Williams JR, Watanabe K, Taniguchi T, et al. Effective Cleaning of Hexagonal Boron Nitride for Graphene Devices. Nano Letters. 2012;12(9):4449-54.

38. Stöhr RJ, Kolesov R, Xia K, Wrachtrup J. All-Optical High-Resolution Nanopatterning and 3D Suspending of Graphene. ACS Nano. 2011;5(6):5141-50.

39. Solomon JM, Ahmad SI, Dave A, Lu L-S, HadavandMirzaee F, Lin S-C, et al. Ultrafast laser ablation, intrinsic threshold, and nanopatterning of monolayer molybdenum disulfide. Scientific Reports. 2022;12(1):6910.

40. Joglekar AP, Liu H-h, Meyhöfer E, Mourou G, Hunt AJ. Optics at critical intensity: Applications to nanomorphing. Proceedings of the National Academy of Sciences. 2004;101(16):5856-61.

41. Henriques JCG, Ventura GB, Fernandes CDM, Peres NMR. Optical absorption of single-layer hexagonal boron nitride in the ultraviolet. Journal of Physics: Condensed Matter. 2020;32(2):025304.

42. Li Y, Rao Y, Mak KF, You Y, Wang S, Dean CR, et al. Probing Symmetry Properties of Few-Layer MoS2 and h-BN by Optical Second-Harmonic Generation. Nano Letters. 2013;13(7):3329-33.

43. Popkova AA, Antropov IM, Fröch JE, Kim S, Aharonovich I, Bessonov VO, et al. Optical Third-Harmonic Generation in Hexagonal Boron Nitride Thin Films. ACS Photonics. 2021;8(3):824-31.

44. Hou S, Birowosuto MD, Umar S, Anicet MA, Tay RY, Coquet P, et al. Localized emission from laser-irradiated defects in 2D hexagonal boron nitride. 2D Materials. 2018;5(1):015010.

45. Gao X, Pandey S, Kianinia M, Ahn J, Ju P, Aharonovich I, et al. Femtosecond Laser Writing of Spin Defects in Hexagonal Boron Nitride. ACS Photonics. 2021;8(4):994-1000.

46. Balling P, Schou J. Femtosecond-laser ablation dynamics of dielectrics: basics and applications for thin films. Reports on Progress in Physics. 2013;76(3):036502.

47. Mero M, Liu J, Rudolph W, Ristau D, Starke K. Scaling laws of femtosecond laser pulse induced breakdown in oxide films. Physical Review B. 2005;71(11):115109.

48. Jiang L, Wang A-D, Li B, Cui T-H, Lu Y-F. Electrons dynamics control by shaping femtosecond laser pulses in micro/nanofabrication: modeling, method, measurement and application. Light: Science & Applications. 2018;7(2):17134-.

49. Wang X, Zhao M, Nolte DD. Optical contrast and clarity of graphene on an arbitrary substrate. Applied Physics Letters. 2009;95(8).

50. Shearer CJ, Slattery AD, Stapleton AJ, Shapter JG, Gibson CT. Accurate thickness measurement of graphene. Nanotechnology. 2016;27(12):125704.

51. Nemes-Incze P, Osváth Z, Kamarás K, Biró LP. Anomalies in thickness measurements of graphene and few layer graphite crystals by tapping mode atomic force microscopy. Carbon. 2008;46(11):1435-42.

52. Hsu W-F, Lu L-S, Kuo P-C, Chen J-H, Chueh W-C, Yeh H, et al. Monolayer MoS2 Enabled Single-Crystalline Growth of AlN on Si(100) Using Low-Temperature Helicon Sputtering. ACS Applied Nano Materials. 2019;2(4):1964-9.

53. Chen T-A, Chuu C-P, Tseng C-C, Wen C-K, Wong HSP, Pan S, et al. Wafer-scale single-crystal hexagonal boron nitride monolayers on Cu (111). Nature. 2020;579(7798):219-23.

54. Huang Y, Sutter E, Shi NN, Zheng J, Yang T, Englund D, et al. Reliable Exfoliation of Large-Area High-Quality Flakes of Graphene and Other Two-Dimensional Materials. ACS Nano. 2015;9(11):10612-20.

55. Paradisanos I, Kymakis E, Fotakis C, Kioseoglou G, Stratakis E. Intense femtosecond photoexcitation of bulk and monolayer MoS2. Applied Physics Letters. 2014;105(4).

56. Pan Y, Yang M, Li Y, Wang Z, Zhang C, Zhao Y, et al. Threshold Dependence of Deep- and Near-subwavelength Ripples Formation on Natural MoS2 Induced by Femtosecond Laser. Scientific Reports. 2016;6(1):19571.

57. Pan C, Jiang L, Sun J, Wang Q, Wang F, Wang K, et al. Ultrafast optical response and ablation mechanisms of molybdenum disulfide under intense femtosecond laser irradiation. Light: Science & Applications. 2020;9(1):80.

58. Castellanos-Gomez A, Barkelid M, Goossens AM, Calado VE, van der Zant HSJ, Steele GA. Laser-Thinning of MoS2: On Demand Generation of a Single-Layer Semiconductor. Nano Letters. 2012;12(6):3187-92.

59. Zhang W, Li L, Wang ZB, Pena AA, Whitehead DJ, Zhong ML, et al. Ti:sapphire femtosecond laser direct micro-cutting and profiling of graphene. Applied Physics A. 2012;109(2):291-7.

60. Currie M, Caldwell JD, Bezares FJ, Robinson J, Anderson T, Chun H, et al. Quantifying pulsed laser induced damage to graphene. Applied Physics Letters. 2011;99(21).

61. Gil-Villalba A, Xie C, Salut R, Furfaro L, Giust R, Jacquot M, et al. Deviation from threshold model in ultrafast laser ablation of graphene at sub-micron scale. Applied Physics Letters. 2015;107(6).

62. Roberts A, Cormode D, Reynolds C, Newhouse-Illige T, LeRoy BJ, Sandhu AS. Response of graphene to femtosecond high-intensity laser irradiation. Applied Physics Letters. 2011;99(5).

63. Wetzel B, Xie C, Lacourt P-A, Dudley JM, Courvoisier F. Femtosecond laser fabrication of micro and nano-disks in single layer graphene using vortex Bessel beams. Applied Physics Letters. 2013;103(24).

64. Yoo J-H, Bin In J, Bok Park J, Jeon H, Grigoropoulos CP. Graphene folds by femtosecond laser ablation. Applied Physics Letters. 2012;100(23).

65. Han GH, Chae SJ, Kim ES, Güneş F, Lee IH, Lee SW, et al. Laser Thinning for Monolayer Graphene Formation: Heat Sink and Interference Effect. ACS Nano. 2011;5(1):263-8.

66. Tran-Khac B-C, White RM, DelRio FW, Chung K-H. Layer-by-layer thinning of MoS2 via laser irradiation. Nanotechnology. 2019;30(27):275302.

67. Yoon D, Moon H, Son Y-W, Choi JS, Park BH, Cha YH, et al. Interference effect on Raman spectrum of graphene on ${\text{SiO}}_{2}/\text{Si}$. Physical Review B. 2009;80(12):125422.

68. Lien D-H, Kang JS, Amani M, Chen K, Tosun M, Wang H-P, et al. Engineering Light Outcoupling in 2D Materials. Nano Letters. 2015;15(2):1356-61.

69. Chen Y-C, Yeh H, Lee C-J, Chang W-H. Distributed Bragg Reflectors as Broadband and Large-Area Platforms for Light-Coupling Enhancement in 2D Transition-Metal Dichalcogenides. ACS Applied Materials & Interfaces. 2018;10(19):16874-80.

70. Donnelly GE, Velický M, Hendren WR, Bowman RM, Huang F. Achieving extremely high optical contrast of atomically-thin MoS2. Nanotechnology. 2020;31(14):145706.

71. Velický M, Hendren WR, Donnelly GE, Katzen JM, Bowman RM, Huang F. Optimising the visibility of graphene and graphene oxide on gold with multilayer heterostructures. Nanotechnology. 2018;29(27):275205.

72. Liu JM. Simple technique for measurements of pulsed Gaussian-beam spot sizes. Opt Lett. 1982;7(5):196-8.

73. Rumble JR, Bruno TJ, Doa MJ. CRC handbook of chemistry and physics : a ready-reference book of chemical and physical data. 102nd edition ed. Boca Raton: CRC Press/Taylor & Francis Group; 2021.

74. Yalon E, McClellan CJ, Smithe KKH, Muñoz Rojo M, Xu RL, Suryavanshi SV, et al. Energy Dissipation in Monolayer MoS2 Electronics. Nano Letters. 2017;17(6):3429-33.

75. Zhang X, Sun D, Li Y, Lee G-H, Cui X, Chenet D, et al. Measurement of Lateral and Interfacial Thermal Conductivity of Single- and Bilayer MoS2 and MoSe2 Using Refined Optothermal Raman Technique. ACS Applied Materials & Interfaces. 2015;7(46):25923-9.

76. Yasaei P, Foss CJ, Karis K, Behranginia A, El-Ghandour AI, Fathizadeh A, et al. Interfacial Thermal Transport in Monolayer MoS2- and Graphene-Based Devices. Advanced Materials Interfaces. 2017;4(17):1700334.

77. Tran Khac BC, Jeon K-J, Choi ST, Kim YS, DelRio FW, Chung K-H. Laser-Induced Particle Adsorption on Atomically Thin MoS2. ACS Applied Materials & Interfaces. 2016;8(5):2974-84.

78. Lin L, Li J, Li W, Yogeesh MN, Shi J, Peng X, et al. Optothermoplasmonic Nanolithography for On-Demand Patterning of 2D Materials. Advanced Functional Materials. 2018;28(41):1803990.

79. Park JB, Yoo J-H, Grigoropoulos CP. Multi-scale graphene patterns on arbitrary substrates via laser-assisted transfer-printing process. Applied Physics Letters. 2012;101(4).

80. Ashkenasi D, Stoian R, Rosenfeld A. Single and multiple ultrashort laser pulse ablation threshold of Al2O3 (corundum) at different etch phases. Applied Surface Science. 2000;154-155:40-6.

81. Börner P. Ultra-short pulsed laser ablation of diamond: ETH Zurich; 2019.

82. Mero M, Clapp B, Jasapara J, Rudolph W, Ristau D, Starke K, et al. On the damage behavior of dielectric films when illuminated with multiple femtosecond laser pulses. Optical Engineering. 2005;44(5):051107.

83. Nguyen D, Emmert L, Mero M, Rudolph W, Patel D, Krous E, et al. The effect of annealing on the subpicosecond breakdown behavior of hafnia films: SPIE; 2008.

84. Rosenfeld A, Lorenz M, Stoian R, Ashkenasi D. Ultrashort-laser-pulse damage threshold of transparent materials and the role of incubation. Applied Physics A. 1999;69(1):S373-S6.

85. Sun Z, Lenzner M, Rudolph W. Generic incubation law for laser damage and ablation thresholds. Journal of Applied Physics. 2015;117(7).

86. Bahmani M, Faghihnasiri M, Lorke M, Kuc A-B, Frauenheim T. Electronic Properties of Defective MoS2 Monolayers Subject to Mechanical Deformations: A First-Principles Approach. physica status solidi (b). 2020;257(5):1900541.

87. Hong J, Hu Z, Probert M, Li K, Lv D, Yang X, et al. Exploring atomic defects in molybdenum disulphide monolayers. Nature Communications. 2015;6(1):6293.

88. Khan MA, Erementchouk M, Hendrickson J, Leuenberger MN. Electronic and optical properties of vacancy defects in single-layer transition metal dichalcogenides. Physical Review B. 2017;95(24):245435.

89. Liu Y, Stradins P, Wei S-H. Air Passivation of Chalcogen Vacancies in Two-Dimensional Semiconductors. Angewandte Chemie International Edition. 2016;55(3):965-8.

90. Förster A, Gemming S, Seifert G, Tománek D. Chemical and Electronic Repair Mechanism of Defects in MoS2 Monolayers. ACS Nano. 2017;11(10):9989-96.

91. Lu J, Carvalho A, Chan XK, Liu H, Liu B, Tok ES, et al. Atomic Healing of Defects in Transition Metal Dichalcogenides. Nano Letters. 2015;15(5):3524-32.

92. Ma Q, Odenthal PM, Mann J, Le D, Wang CS, Zhu Y, et al. Controlled argon beam-induced desulfurization of monolayer molybdenum disulfide. Journal of Physics: Condensed Matter. 2013;25(25):252201.

93. Oh HM, Han GH, Kim H, Bae JJ, Jeong MS, Lee YH. Photochemical Reaction in Monolayer MoS2 via Correlated Photoluminescence, Raman Spectroscopy, and Atomic Force Microscopy. ACS Nano. 2016;10(5):5230-6.

94. Sivaram SV, Hanbicki AT, Rosenberger MR, Jernigan GG, Chuang H-J, McCreary KM, et al. Spatially Selective Enhancement of Photoluminescence in MoS2 by Exciton-Mediated Adsorption and Defect Passivation. ACS Applied Materials & Interfaces. 2019;11(17):16147-55.

95. Kukucska G, Koltai J. Theoretical Investigation of Strain and Doping on the Raman Spectra of Monolayer MoS2. physica status solidi (b). 2017;254(11):1700184.

96. Wang Y, Cong C, Qiu C, Yu T. Raman Spectroscopy Study of Lattice Vibration and Crystallographic Orientation of Monolayer MoS2 under Uniaxial Strain. Small. 2013;9(17):2857-61.

97. Mawlong LPL, Paul KK, Giri PK. Direct Chemical Vapor Deposition Growth of Monolayer MoS2 on TiO2 Nanorods and Evidence for Doping-Induced Strong Photoluminescence Enhancement. The Journal of Physical Chemistry C. 2018;122(26):15017-25.

98. Wu J, Li H, Yin Z, Li H, Liu J, Cao X, et al. Layer Thinning and Etching of Mechanically Exfoliated MoS2 Nanosheets by Thermal Annealing in Air. Small. 2013;9(19):3314-9.

99. Emmert LA, Mero M, Rudolph W. Modeling the effect of native and laser-induced states on the dielectric breakdown of wide band gap optical materials by multiple subpicosecond laser pulses. Journal of Applied Physics. 2010;108(4).

100. Wang X, Hong Y, Wang M, Xin G, Yue Y, Zhang J. Mechanical properties of molybdenum diselenide revealed by molecular dynamics simulation and support vector machine. Physical Chemistry Chemical Physics. 2019;21(18):9159-67.

101. Santos RCR, Longhinotti E, Freire VN, Reimberg RB, Caetano EWS. Elucidating the high-k insulator α-Al2O3 direct/indirect energy band gap type through density functional theory computations. Chemical Physics Letters. 2015;637:172-6.

102. Guizard S, Martin P, Petite G, Oliveira PD, Meynadier P. Time-resolved study of laser-induced colour centres in. Journal of Physics: Condensed Matter. 1996;8(9):1281.

103. Solomon JM, Ahmad SI, Dave A, Lu L-S, Wu Y-C, Chang W-H, et al. Ultrafast multi-shot ablation and defect generation in monolayer transition metal dichalcogenides. AIP Advances. 2022;12(1):015217.

104. Bloembergen N. Laser-induced electric breakdown in solids. IEEE Journal of Quantum Electronics. 1974;10(3):375-86.

105. Cai Q, Scullion D, Falin A, Watanabe K, Taniguchi T, Chen Y, et al. Raman signature and phonon dispersion of atomically thin boron nitride. Nanoscale. 2017;9(9):3059-67.

106. Stenger I, Schué L, Boukhicha M, Berini B, Plaçais B, Loiseau A, et al. Low frequency Raman spectroscopy of few-atomic-layer thick hBN crystals. 2D Materials. 2017;4(3):031003.

107. Gorbachev RV, Riaz I, Nair RR, Jalil R, Britnell L, Belle BD, et al. Hunting for Monolayer Boron Nitride: Optical and Raman Signatures. Small. 2011;7(4):465-8.

108. Cai Q, Scullion D, Gan W, Falin A, Cizek P, Liu S, et al. Outstanding Thermal Conductivity of Single Atomic Layer Isotope-Modified Boron Nitride. Physical Review Letters. 2020;125(8):085902.

109. Gallais L, Bergeret E, Wang B, Guerin M, Bènevent E. Ultrafast laser ablation of metal films on flexible substrates. Applied Physics A. 2014;115(1):177-88.

110. Sahin R, Simsek E, Akturk S. Nanoscale patterning of graphene through femtosecond laser ablation. Applied Physics Letters. 2014;104(5).

111. Yoo J-H, In JB, Park JB, Jeon H, Grigoropoulos CP. Graphene folds by femtosecond laser ablation. Applied Physics Letters. 2012;100(23):233124.

112. Sahin R, Simsek E, Akturk S. Nanoscale patterning of graphene through femtosecond laser ablation. Applied Physics Letters. 2014;104(5):053118.

113. Stephens RI. Metal Fatigue in Engineering: John Wiley & Sons; 2000.

114. Yang Y, Song Z, Lu G, Zhang Q, Zhang B, Ni B, et al. Intrinsic toughening and stable crack propagation in hexagonal boron nitride. Nature. 2021;594(7861):57-61.

115. Deng J, Fampiou I, Liu JZ, Ramasubramaniam A, Medhekar NV. Edge stresses of non-stoichiometric edges in two-dimensional crystals. Applied Physics Letters. 2012;100(25).

116. Zhang P, Ma L, Fan F, Zeng Z, Peng C, Loya PE, et al. Fracture toughness of graphene. Nature Communications. 2014;5(1):3782.

117. Enrico A, Hartwig O, Dominik N, Quellmalz A, Gylfason KB, Duesberg GS, et al. Ultrafast and Resist-Free Nanopatterning of 2D Materials by Femtosecond Laser Irradiation. ACS Nano. 2023;17(9):8041-52.

118. Jain A, Bharadwaj P, Heeg S, Parzefall M, Taniguchi T, Watanabe K, et al. Minimizing residues and strain in 2D materials transferred from PDMS. Nanotechnology. 2018;29(26):265203.

119. Golin SM, Kirkwood SE, Klug DD, Villeneuve DM, Rayner DM, Herrero CAT, et al. Strong field processes inside gallium arsenide. Journal of Physics B: Atomic, Molecular and Optical Physics. 2014;47(20):204025.

120. Li X, Rong W, Jiang L, Zhang K, Li C, Cao Q, et al. Generation and elimination of polarization-dependent ablation of cubic crystals by femtosecond laser radiation. Opt Express. 2014;22(24):30170-6.

121. Chris BS, André B, Eric M. Laser-induced breakdown and damage in bulk transparent materials induced by tightly focused femtosecond laser pulses. Measurement Science and Technology. 2001;12(11):1784.

122. Bloember N. Laser-induced electric breakdown in solids. IEEE Journal of Quantum Electronics. 1974;10(3):375-86.

123. Cherednikov Y, Inogamov NA, Urbassek HM. Influence of defects on extreme ultraviolet laser ablation of LiF. Physical Review B. 2013;88(13):134109.

124. Mishchik K. Ultrafast laser-induced modification of optical glasses : a spectroscopy insight into the microscopic mechanisms 2012.

125. Tran TT, Bray K, Ford MJ, Toth M, Aharonovich I. Quantum emission from hexagonal boron nitride monolayers. Nature Nanotechnology. 2016;11(1):37-41.

126. Kumar A, Cholsuk C, Zand A, Mishuk MN, Matthes T, Eilenberger F, et al. Localized creation of yellow single photon emitting carbon complexes in hexagonal boron nitride. APL Materials. 2023;11(7).

127. Attaccalite C, Bockstedte M, Marini A, Rubio A, Wirtz L. Coupling of excitons and defect states in boron-nitride nanostructures. Physical Review B. 2011;83(14):144115.

128. Ouyang Q, Zhang K, Chen W, Zhou F, Ji W. Nonlinear absorption and nonlinear refraction in a chemical vapor deposition-grown, ultrathin hexagonal boron nitride film. Opt Lett. 2016;41(7):1368-71.

129. Pierret A, Mele D, Graef H, Palomo J, Taniguchi T, Watanabe K, et al. Dielectric permittivity, conductivity and breakdown field of hexagonal boron nitride. Materials Research Express. 2022;9(6):065901.

130. Ranjan A, O'Shea SJ, Padovani A, Su T, La Torraca P, Ang YS, et al. Molecular Bridges Link Monolayers of Hexagonal Boron Nitride during Dielectric Breakdown. ACS Applied Electronic Materials. 2023;5(2):1262-76.

131. Martin S, Hertwig A, Lenzner M, Krüger J, Kautek W. Spot-size dependence of the ablation threshold in dielectrics for femtosecond laser pulses. Applied Physics A. 2003;77(7):883-4.

132. Chimier B, Utéza O, Sanner N, Sentis M, Itina T, Lassonde P, et al. Damage and ablation thresholds of fused-silica in femtosecond regime. Physical Review B. 2011;84(9):094104.

133. Sudrie L, Couairon A, Franco M, Lamouroux B, Prade B, Tzortzakis S, et al. Femtosecond Laser-Induced Damage and Filamentary Propagation in Fused Silica. Physical Review Letters. 2002;89(18):186601.

134. Chatzakis I, Davidson RB, II, Dunkelberger AD, Liu S, Freitas J, Culbertson J, et al. Rapid Bimolecular and Defect-Assisted Carrier Recombination in Hexagonal Boron Nitride. The Journal of Physical Chemistry C. 2019;123(23):14689-95.

135. Wu AQ, Chowdhury IH, Xu X. Femtosecond laser absorption in fused silica: Numerical and experimental investigation. Physical Review B. 2005;72(8):085128.

136. Sokolowski-Tinten K, Bialkowski J, von der Linde D. Ultrafast laser-induced order-disorder transitions in semiconductors. Physical Review B. 1995;51(20):14186-98.

137. Deng S, Gu Y, Wan X, Gao M, Xu S, Chen K, et al. Probing Electronic Properties of CVD Monolayer Hexagonal Boron Nitride by an Atomic Force Microscope. Frontiers in Materials. 2021;8.

138. Maity A, Grenadier SJ, Li J, Lin JY, Jiang HX. Hexagonal boron nitride: Epitaxial growth and device applications. Progress in Quantum Electronics. 2021;76:100302.

139. Stuart BC, Feit MD, Herman S, Rubenchik AM, Shore BW, Perry MD. Nanosecond-to-femtosecond laser-induced breakdown in dielectrics. Physical Review B. 1996;53(4):1749-61.

140. Jia B, Guan Z, Peng Z, Zhang J, Guan X, Guan P, et al. Structural disorder in fused silica with ODC(I) defect. Applied Physics A. 2018;124(10):696.

141. Dolgonos A, Mason TO, Poeppelmeier KR. Direct optical band gap measurement in polycrystalline semiconductors: A critical look at the Tauc method. Journal of Solid State Chemistry. 2016;240:43-8.

142. Mu X, Wu X, Zhang T, Go DB, Luo T. Thermal Transport in Graphene Oxide – From Ballistic Extreme to Amorphous Limit. Scientific Reports. 2014;4(1):3909.

143. Hong Y, Zhang J, Zeng XC. Thermal Conductivity of Monolayer MoSe2 and MoS2. The Journal of Physical Chemistry C. 2016;120(45):26067-75.

144. Ashby NWaMF. CRC- Elsevier materials selector: CRC PRess; 1991.

145. Lide DR. CRC Handbook of physics and chemistry. 76 ed: CRC Press; 1996.

146. Keldysh LV. Ionization in the Field of a Strong Electromagnetic Wave. Soviet Physics JETP. 1965;20:1307-14.

147. Ramasubramaniam A. Large excitonic effects in monolayers of molybdenum and tungsten dichalcogenides. Physical Review B. 2012;86(11):115409.

148. Gritsenko VA, Ivanov RM, Morokov Y. Electronic structure of amorphous SiO2: Experiment and numerical simulation. Journal of Experimental and Theoretical Physics. 1995;81:1208-16.

149. Perevalov TV, Shaposhnikov AV, Gritsenko VA, Wong H, Han JH, Kim CW. Electronic structure of α-Al2O3: Ab initio simulations and comparison with experiment. JETP Letters. 2007;85(3):165-8.

150. Perevalov TV, Gritsenko VA, Kaichev V. Electronic structure of aluminum oxide: Ab initio simulations of α and γ phases and comparison with experiment for amorphous films. European Physical Journal-applied Physics - EUR PHYS J-APPL PHYS. 2010;52.

151. Li Y, Dong N, Zhang S, Zhang X, Feng Y, Wang K, et al. Giant two-photon absorption in monolayer MoS2. Laser & Photonics Reviews. 2015;9(4):427-34.

152. Zhou F, Ji W. Giant Three-Photon Absorption in Monolayer MoS2 and Its Application in Near-Infrared Photodetection. Laser & Photonics Reviews. 2017;11(4):1700021.

153. Tsang HK, Grant RS, Penty RV, White IH, Soole JBD, Colas E, et al. GaAs/GaAlAs multiquantum well waveguides for all-optical switching at 1.55 μm. Electronics Letters [Internet]. 1991; 27(22):[1993-5 pp.]. Available from: https://digital-library.theiet.org/content/journals/10.1049/el_19911235.

154. Salehzadeh O, Tran NH, Liu X, Shih I, Mi Z. Exciton Kinetics, Quantum Efficiency, and Efficiency Droop of Monolayer MoS2 Light-Emitting Devices. Nano Letters. 2014;14(7):4125-30.

155. Cunningham PD, McCreary KM, Jonker BT. Auger Recombination in Chemical Vapor Deposition-Grown Monolayer WS2. The Journal of Physical Chemistry Letters. 2016;7(24):5242-6.

156. Hajisalem G, Shariatdoust MS, Ali RF, Gates BD, Barclay PE, Gordon R. Single Nanoflake Hexagonal Boron Nitride Harmonic Generation with Ultralow Pump Power. ACS Photonics. 2021;8(7):1922-6.

157. Pela RR, Marques M, Teles LK. Comparing LDA-1/2, HSE03, HSE06 and G0W0 approaches for band gap calculations of alloys. Journal of Physics: Condensed Matter. 2015;27(50):505502.

158. Lebègue S, Klintenberg M, Eriksson O, Katsnelson MI. Accurate electronic band gap of pure and functionalized graphane from GW calculations. Physical Review B. 2009;79(24):245117.

159. Kumar V, Mishra RK, Kumar P, Gwag JS. A comprehensive study on the electronic structure, dielectric and optical properties of alkali-earth metals and transition metal hydroxides M(OH)2. Luminescence. 2023;38(7):1307-18.

160. Murakami T, Honjo T, Kuji T. DOS Calculation Analysis of New Transparent Conductor Mg(OH)2-C. MATERIALS TRANSACTIONS. 2011;52(8):1689-92.

161. Pishtshev A, Karazhanov SZ, Klopov M. Excitons in Mg(OH)2 and Ca(OH)2 from ab initio calculations. Solid State Communications. 2014;193:11-5.

162. Suslu A, Wu K, Sahin H, Chen B, Yang S, Cai H, et al. Unusual dimensionality effects and surface charge density in 2D Mg(OH)2. Scientific Reports. 2016;6(1):20525.

163. Xia C, Xiong W, Du J, Wang T, Wei Z, Li J. Robust electronic and mechanical properties to layer number in 2D wide-gap X(OH)2 (X = Mg, Ca). Journal of Physics D: Applied Physics. 2018;51(1):015107.

164. Acharya S, Pashov D, Cunningham B, Rudenko AN, Rösner M, Grüning M, et al. Electronic structure of chromium trihalides beyond density functional theory. Physical Review B. 2021;104(15):155109.

165. Zhu L, Yang L. Quasiparticle energies and excitonic effects of chromium trichloride: From two dimensions to bulk. Physical Review B. 2020;101(24):245401.